Carnegie Mellon University

Carnegie Institute of Technology

Thesis Submitted in Partial Fulfillment of the Requirements for the Degree of

DOCTOR OF PHILOSOPHY

Title: BOUNDARY LAYER RECEPTIVITY AND RESONANCE CAUSED BY TUNED DISTURBANCES WITHIN CASCADE FLOWS

Presented by: **Luis Ramón Rojas-Solórzano**

Accepted by the Department of Mechanical Engineering

Cristina Amon — 6-6-97

Cristina H. Amon, Major Professor — Date

Adnan Akay — 6-9-97

Adnan Akay, Department Head — Date

Approved by the College Council

Daniel D. Stancil — 6-10-97

John L. Anderson, Dean — Date

Carnegie Mellon

CARNEGIE MELLON UNIVERSITY
DEPARTMENT OF MECHANICAL ENGINEERING

FINAL PUBLIC ORAL EXAMINATION
For the Degree of
DOCTOR OF PHILOSOPHY

Candidate: Luis Ramon Rojas-Solorzano

Title of Dissertation: "Boundary Layer Receptivity and Resonance Caused by Tuned Disturbances within Cascade Flows "

Department: Mechanical Engineering

Date and Time: May 7, 1997
10:30 a.m.

Place: Scaife Hall 301

Examiners:
Professor Cristina Amon, Chair
Professor Mingking Chyu
Professor Omar Ghattas (Civil Engineering)
Professor Wilfred Rouleau
Professor Robert Simoneau

Carnegie Mellon University

BOUNDARY LAYER RECEPTIVITY AND RESONANCE CAUSED BY TUNED DISTURBANCES WITHIN CASCADE FLOWS

A DISSERTATION
SUBMITTED TO THE CARNEGIE INSTITUTE OF TECHNOLOGY
IN PARTIAL FULFILLMENT OF THE REQUIREMENTS

for the degree

DOCTOR OF PHILOSOPHY
IN
MECHANICAL ENGINEERING

by

Luis Ramón Rojas-Solórzano

Pittsburgh, Pennsylvania

May 1997

ACKNOWLEDGMENTS

First, I have to recognize all what I have learned and the experience I have obtained from my Ph.D. research at Carnegie Mellon University and the opportunity to work with the leading edge in existing research resources.

During these five years I have learned to do independent fundamental research, learned to implement some of the latest techniques on CFD, met many international friends, had the experience of taking really enjoyable graduate courses as Turbulent Flow and CFD with my advisor Professor Cristina Amon and had the opportunity of being a TA for an undergraduate course and being rewarded as the Best TA of the Department by my students.

I could not have been able to succeed in this program without the help of all the people who accompanied me for these five years. I would like to specially mention those who come to my mind at this moment.

Special gratitude to my wife, Mirian, for all these years of patience and support. To my mother for all her thoughts, support and love. To my daughter, Claudia, and my son, Luis, for being the light of my life. To my patron Virgen del Valle who has never left me alone. To my brothers, sisters and rest of the family in Venezuela for their continuous support in my life; I love you guys. To my father, who taught me to be honest. To my second father, Professor Stefan Zarea, who taught me to be a hard worker and what I am able to achieve in my professional life.

Very special thanks to my advisor Professor Cristina Amon for the opportunity she gave me of being part of her research group, for all the insightful comments that helped me understand and analyze much better the problem I was investigating, and for being an extraordinary example of what a hard worker and a successful researcher is.

Thanks to the FUNDAYACUCHO/LASPAU José María Vargas program and to my home-institution Universidad Simón Bolívar for funding my studies.

Thanks to all my friends: Ignacio, Mary, German, Fernando, Fatima, Amador, Jauber, Napoleon, Lissette, the Parisi-Amon Family, Luis Alberto, Cucha, Richard, Lin, Kevin and all the ones I did not mention but who have given me the gift of their friendship.

My gratitude also to the members of my thesis committee: Professors Cristina Amon, Mingking Chyu, Omar Ghattas, Wilfred Rouleau and Robert Simoneau for all the ideas and comments they provided that enriched the content of this work.

The airfoil geometry investigated in this research is based on a high pressure turbine first vane profile suggested to us by Dr. Robert Simoneau, Chief of the Heat Transfer Branch at NASA Lewis at the time this research started.

ABSTRACT

The receptivity and stability of steady non-separated and unsteady separated boundary layers in a two-dimensional airfoil cascade flow is investigated by Direct Numerical Simulation of the time-dependent Navier-Stokes and continuity equations. The study includes the effects caused by the introduction of free-stream time-harmonic disturbances. The calculation of the transport, generation and dissipation of Fluctuating Kinetic Energy (FKE) is introduced as a non-classical technique in the analysis.

Unperturbed flows are first investigated to describe the evolution of the naturally-generated boundary layer instabilities. Above a critical $Re_c \cong 400$, spatially- and temporally-evolving instabilities are observed within the suction-side boundary layer, and separation occurs downstream of the minimum pressure point. Between the minimum pressure point and the separation point, the instabilities undergo a long to short wavelength modulation turning into Tollmien-Schlichting (T-S) transitional waves. The driving role of the production of FKE in the wavelength modulation process is demonstrated. The production largely hastens the wavelength modulation around the inflection point of the mean velocity profile across the boundary layer. Above the inflection point, the fluctuating pressure field favors the energy transport and provides the energy necessary to convect the instabilities out of the boundary layer. The evolution of the T-S waves is marked by a symmetric distribution of the production term in the transverse direction, i.e., in the lower half of the boundary layer, and the mean flow provides energy to the instabilities while the opposite occurs in the upper half.

Perturbed flows are investigated by superposing monotonic time-harmonic disturbances onto the cascade inlet velocity. The disturbance frequencies and amplitudes range between 0.3-37.1 of the basic flow natural frequency and 0.5-2% of the basic flow inlet velocity, respectively. The free-stream disturbances turn into Stokes waves at the interaction with the stationary walls. The boundary layer shows particular sensitivity to disturbances with frequencies close to the natural frequency by exciting T-S waves in subcritical flows and by exhibiting local resonant effects on existent T-S waves in supercritical flows. In subcritical flows, the FKE budget shows that the artificial excitation of T-S waves occurs within the upper half of the boundary layer and is supported by the mean flow convection against an adverse unsteady pressure field. The resonant effect on existent supercritical T-S waves responds to a preferential interaction with the Stokes waves within the lower half of the boundary layer where the production of FKE is enhanced. The stability of the basic flow is found to be unaltered by disturbances with frequencies far from the natural frequency.

TABLE OF CONTENTS

LIST OF FIGURES

LIST OF TABLES

NOMENCLATURE

APG = adverse pressure gradient
c = chord length of airfoil [ft]
c_x = axial chord length of airfoil [ft]
C_p = pressure coefficient $C_p=(p-p_2)/(p_{o1}-p_2)$
d_n = distance from airfoil wall in the normal direction [ft]
D = fluid domain
DNS = direct numerical simulations
FKE = fluctuating kinetic energy
FPG = favorable pressure gradient
h = pitch [ft]
MPP = minimum pressure point
p^* = pressure [lbm/ft-s^2]
p = non-dimensional pressure ($p^*/\rho.U_\infty^2$)
p^*_{o1} = dynamic pressure at blade leading edge [lbm/ft-s^2]
p_{o1} = non-dimensional p^*_{o1} ($p^*_{01}/\rho.U_\infty^2$)
p^*_2 = pressure at blade trailing edge [lbm/ft-s^2]
p_2 = non-dimensional p^*_2 ($p^*_2/\rho.U_\infty^2$)
$q^{*\prime}$ = fluctuating kinetic energy per unit mass [ft^2/s^2]
q' = non-dimensional $q^{*\prime}$ ($q^{*\prime}/ U_\infty^2$)
Re = Reynolds number ($U_\infty.c/\nu$)
Re_c = critical Re
Re_s = Reynolds number based on the suction-side arclength ($U_\infty.s/\nu$)
s = arclength [ft]
s_r = solidity ratio (h/c)
Sp^* = magnitude of the velocity vector (speed) [ft/s]
$Sp^{*\prime}$ = oscillatory component of the speed [ft/s]
Sp' = non-dimensional $Sp^{*\prime}$ ($Sp^{*\prime}/U_\infty$)
SP = separation point
t^* = time [s]
t = non-dimensional time ($t^*.U_\infty/c$)
T1 = non-dimensional term I from FKE equation (eqn. 14b)
T2 = non-dimensional term II from FKE equation (eqn. 14b)
T3 = non-dimensional term III from FKE equation (eqn. 14a)
T4 = non-dimensional term IV from FKE equation (eqn. 14a)
T5 = non-dimensional term V from FKE equation (eqn. 14a)
T6 = non-dimensional term VI from FKE equation (eqn. 14a)
T-S = Tollmien-Schlichting
u^*,v^* = velocity components in x and y-direction, respectively [ft/s]
$u^{*\prime},v^{*\prime}$ = oscillatory components of u and v, respectively [ft/s]
u, v = non-dimensional u^*,v^* (u^*/U_∞ , v^*/U_∞, respectively)
u', v' = non-dimensional $u^{*\prime},v^{*\prime}$ ($u^{*\prime}/U_\infty$, $v^{*\prime}/U_\infty$, respectively)

U_∞ = velocity at the inlet boundary [ft/s]
$\vec{u}^*$ = velocity vector [ft/s]
$\vec{u}$ = non-dimensional $\vec{u}^*$ ($\vec{u}^*/U_\infty$)
u_t^*, u_n^* = velocity components in tangential and normal direction to the wall, respectively [ft/s]
u_t, v_n = non-dimensional u_t^*, v_n^* (u_t^*/U_∞ , v_n^*/U_∞, respectively)
x^* = x-axis distance [ft]
y^* = y-axis distance [ft]
x = non-dimensional x^* (x^*/c)
y = non-dimensional y^* (y^*/c)
α = angle of attack [°]
β = angle of stagger [°]
Δ = variation of the accompanying parameter
ε^* = amplitude of the superposed disturbance (% of U_∞)
ε = non-dimensional ε^* (ε^*/U_∞)
ν = kinematic viscosity [ft^2/s]
ρ = density [lbm/ft^3]
τ_{xy}^* = shear stress on x-y plane [$lbm/(ft.s^2)$]
τ_{xy} = non-dimensional τ_{xy}^* ($\tau_{xy}^*.c/(\mu.U_\infty)$)
τ_w^* = shear stress on plane tangential to the wall [$lbm/(ft.s^2)$]
τ_w = non-dimensional τ_w^* ($\tau_w^*.c/(\mu.U_\infty)$)
ω^* = natural angular frequency for basic flow [rad/s]
ω = non-dimensional ω^* ($\omega^*.c/U_\infty$)
ω_d^* = angular frequency of the superposed disturbance [rad/s]
ω_d = non-dimensional ω_d^* ($\omega_d^*.c/U_\infty$)
ω_{LS}^* = angular frequency of the least stable mode of the basic flow obtained by linear stability analysis of the Orr-Sommerfeld equation [rad/s]
ω_{LS} = non-dimensional ω_{LS}^* ($\omega_{LS}^*.c/U_\infty$)
ω^*_z = z-component of the vorticity vector [s^{-1}]
ω_z = non-dimensional ω^*_z ($\omega^*_z.c/U_\infty$)

Subscripts

$_{2D\_400}$ = two-dimensional basic flow at Re=400
$_{2D\_600}$ = two-dimensional basic flow at Re=600
$_{2D\_1000}$ = two-dimensional basic flow at Re=1000
$_{3D\_400}$ = three-dimensional basic flow at Re=400

CHAPTER 1

INTRODUCTION

Most flows of real fluids in engineering applications exhibit an irregular time-dependent behavior, termed turbulence (Hinze, 1987), in which velocity, pressure and other quantities show a random variation with time and space. The origin of turbulence and the associated transition from laminar to turbulent flow is considered of fundamental importance in fluid mechanics.

The phenomenon of laminar to turbulent transition in internal flows and in boundary layers occurs at a critical Reynolds number (Re_c) when the flow is perturbed by finite or infinitesimal disturbances. Below Re_c the flow remains laminar even in the presence of very strong disturbances (Schlichting, 1979). The disturbances may be the result from surface irregularities, variations in fluid physical properties (e.g., viscosity and density), environmental noise, upstream wakes and many other sources of physical perturbation.

The transition from laminar to turbulent flow within boundary layers may occur as an evolutive process or as a snap-through event depending on the prevailing conditions in the originally laminar flow. The first type of transition, also denominated natural transition, corresponds to the evolution of primary (linear two-dimensional) and secondary (non-linear three-dimensional) instabilities encountered within boundary layers on solid bodies. The second type is known as by-pass transition and often occurs at very high free-stream perturbation levels. In this type of transition, the evolution of the primary and secondary instabilities is by-passed. Therefore, turbulent spots are produced within the boundary layer before a developed turbulent regime sets in. It is believed that under high levels of flow disturbances by-pass transition is the dominant form of laminar to turbulent transition within boundary layer flows.

The origin of natural transition in boundary layer flows is strongly related to the study of another phenomenon named receptivity. Receptivity is the physical

mechanism by which energy is transferred from the typically long wavelength free-stream disturbances to the short wavelength boundary layer transitional instabilities (Morkovin, 1969). The study of the receptivity is one aspect of fluid dynamics that currently attracts significant attention from researchers (Sherman, 1990). The boundary layer receptivity determines how natural transition initiates and the subsequent initial evolution of the primary instabilities, known as Tollmien-Schlichting (T-S) waves. Further evolution of T-S waves within the boundary layer depends on the Reynolds number (Re). Above a critical Re (Re_c) the T-S wave amplitude might saturate becoming the flow unstable to three-dimensional disturbances and triggering convective three-dimensional instabilities, i.e., secondary instabilities. The secondary instabilities convect further downstream and might equilibrate at a finite amplitude or have an unbounded fast growth and precede the complete turbulence (Herbert, 1988).

The T-S waves are characterized by a relatively short wavelength compared to free-stream disturbances (Loehrke et al., 1975; Kerschen et al., 1990; Goldstein & Hultgren, 1987, 1989), by a convective speed between zero and the flow speed outside the boundary layer (Sherman, 1990), and by an exponential evolution.

The study of the stability of fluid flows is an important area of research in fluid mechanics. The stability analysis of a fluid flow is oriented to determine how the originally laminar flow is affected by naturally-generated or artificially-superimposed disturbances. In the first case, the source of the disturbances might be the increase in the Re, whereas in the second case, the disturbances are superposed artificially onto the basic flow. The fundamental question is whether the amplitude of the disturbances increases or dies out. If the amplitude decays, the mean flow is said to be stable; if the amplitude increases, the flow is considered unstable. In this case, there exists the possibility of transition to a turbulent regime (Schlichting, 1979).

Understanding and predicting transition within boundary layer flows is also relevant to calculating the force exerted on the wall and the heat transfer characteristics since these are strongly dependent on whether the boundary layer

flow is laminar, transitional or turbulent. It is acknowledged that the boundary layer transition is mostly affected by the pressure distribution in the external flow, the wall surface and the free-stream disturbances (Schlichting, 1979). In fact, the pressure gradient and the friction near the wall may cause boundary layer separation from the solid surface. Separation might occur in regions with a steep adverse pressure gradient and is always associated with the formation of vortices and with large energy losses.

Furthermore, between 1984 and 1994 the aerospace industry, leaded by NASA, dedicated major efforts to the study of the by-pass transition in boundary layers within blades and vanes in high-pressure turbines. A summary of the progress of the such named Bypass Transition Program was presented by Simon & Ashpis (1996). Present needs of the industry (Simon & Ashpis, 1996) point to the search of improvements in the models that predict natural transition within separated boundary layers typically encountered in Low-Pressure Turbines (LPT). Major research work is currently ongoing in the experimental, computational, analytical and modeling areas. The improved understanding and modeling of the flow field characteristics will contribute to improve predictions of temperature and losses, as well as impact favorably in better designs.

This investigation contributes to the fundamental study of the receptivity and stability of the boundary layer undergoing natural separated and induced non-separated flow transition within an experimental airfoil cascade geometry.

CHAPTER 2

BIBLIOGRAPHICAL REVIEW

This section introduces briefly the current knowledge of receptivity and transition within boundary layer flows including the flow within turbine blade passages.

Previous research on boundary layer receptivity and stability has mainly focused on flat plate with variations in the leading edge geometry and on isolated airfoils. Up to this date, only preliminary numerical studies of the boundary layer receptivity and stability to free-stream disturbances within airfoil cascades have been made (Rojas & Amon, 1995, 1997). Most of the previous transitional studies on this geometry have been experimental and mainly oriented to determine the initiation and coverage of the laminar-turbulent transition within separated boundary layers.

The following three subsections summarize the work done experimentally, theoretically and numerically related to the study of laminar to turbulent transition in boundary layer flows. The next subsection summarizes the most relevant research done on Reynolds stresses transport related to our investigation of the interpretation of the receptivity phenomenon and the flow stability.

2.1. Experimental Investigation

2.1.1. Isolated Airfoil and Flat Plate. Experimental investigations based on isolated airfoils and flat plates, reviewed by Kachanov et al. (1982) and Nishioka & Morkovin (1986), showed that receptivity can occur in the vicinity of the leading edge and at localized downstream points. Dovgal et al. (1986) performed experiments on the hydrodynamic stability of separated boundary layers over isolated airfoils and encountered the separation to be an efficient mechanism in the generation and amplification of transitional instabilities. They found the

maximum intensity of the oscillations within the separated boundary layer around the inflection point of the mean velocity profile.

The experiments on the isolated airfoil with flow subject to low and high free-stream turbulence levels (e.g., Grek et al., 1990; Dovgal et al., 1986) also showed that increased free-stream disturbance levels enhance the amplitude of the instability waves in the boundary layer, hastening transition. It was not clear though, how selected modes of the introduced perturbation may have induced the generation of the boundary layer transitional instabilities.

Despite the insight they have provided to the study of transitional flows, experiments on the receptivity to unsteady pressure fields, including acoustic waves, have been inconclusive (e.g., review by Nishioka & Morkovin, 1986), because either (a) poor characterization of forcing field along outer edge of the boundary layer, (b) inadequate local information on the flow fluctuation within the boundary layer in the region where the T-S-like instabilities start growing, (c) lack of documentation of effects around the leading edge, (d) excessive forcing disturbance levels, (e) uncontrolled ambient pressure fields around the test facility, and (f) uncontrolled secondary effects caused by wakes from any support systems including probes.

2.1.2. Airfoil Cascades. Experiments have been made to develop correlations that predict transition in separated boundary layers within turbine blades under controlled free-stream turbulence levels (e.g., Apostolopoulo, 1965; Dunham, 1972). Some researchers (e.g. Wang & Simon, 1987) up to recently considered that existing correlations to determine the location of the transition initial point and coverage are based on limited experimental results which isolate different effects that influence transition. Wang & Simon (1987) suggested that additional heat transfer and hydrodynamic data are necessary to improve the transitional correlations and to further the understanding of laminar to turbulent flow transition in boundary layers.

The flow transition in airfoil cascades has been recognized to be either by-pass or natural type (Mayle, 1991). Natural transition occurs in gas turbines

mainly in compressors and low-pressures turbine blades with separated boundary layers (Mayle, 1991).

In airfoil cascades, separated-flow transition may start in an overspeed region such as near the airfoil leading edge or near the point of minimum pressure on the suction side of the blade (Mayle, 1991; Schlichting, 1979). T-S waves have been identified close to the wall in boundary layers subject to low free-stream turbulence levels undergoing separation (e.g., Gaster, 1969) and in non-separated boundary layers within airfoil cascades (e.g., Dring et al., 1982). In the separated-flow transition it is apparent, as concluded before from the isolated airfoils experiments, the primary role of the separation in the initiation of transition. In the non-separated-flow transition no visualization is provided as to confirm or discard the local interaction between the mean flow and external disturbances downstream the minimum pressure point enabling the boundary layer to trigger transitional waves.

Roberts (1975) characterized transition within turbomachinery cascades in four categories as a function of Re. First, for large Re ($Re>10^6$) flow transition occurs upstream the boundary layer separation point; second, for moderate Re (typically $Re\approx2x10^5$), the laminar boundary layer separates before transition is completed; third, as the Re continues to decrease, the laminar free shear layer grows in length, affecting the flow outside the boundary layer; and as the Re is further decreased ($Re\approx5x10^4$), the separation region becomes so long that reattachment on the blade surface does no longer occur. For further decreases of Re, there is little change within the flow field around the airfoil. Despite the precise delimitation of the four scenarios for the occurrence of transition in airfoil cascades, Roberts' model does not explain how transition starts, i.e., the receptivity issue or how the primary transitional instability characteristics may vary from one case to the other.

To predict transition properly in separated flows, Mayle (1991) stated the need to perform a series of systematic tests for which separation, Re and free-stream turbulence level are varied over a wide spectrum typical of internal and

external cascade flows. However, it is suggested that the important factors affecting the boundary layer transition within turbine blade passages are free-stream turbulence, pressure gradient, and passing wakes, whereas secondary effects are surface curvature, compressibility, and heat transfer (e.g., Mayle, 1991 and Walker, 1993). Although some researchers believe that data from low free-stream turbulence experiments are not valuable for practical purposes (e.g., Mayle, 1991), others have found that observations at low free-stream turbulence levels provide useful insights on the transitional flow phenomena (e.g., Dring et al., 1982; Walker, 1993; Van Fossen et al., 1995).

2.2. Theoretical Investigation

Despite the limited quantitative description of the transition phenomenon, the experimental results stimulated theoretical investigations. Large efforts to explain theoretically the transition phenomenon were initiated many decades ago with remarkable succes within the past forty years. The theoretical work has been based mostly on linear stability theory and asymptotic expansions, summarized in the next sub-sections.

2.2.1. Linear Stability Theory. The linear stability theory (LST) enables the investigation of how laminar flows are affected by infinitesimal small disturbances. As for the stability study, the question is whether these small disturbances superimposed to the mean flow decay or increase with time and space, the mean flow is considered then stable or unstable, respectively (Schlichting, 1979). The LST main postulate is that the disturbance growth only occur in the linear range. This approach has succeeded in the prediction of the least stable modes of perturbation that are likely to appear within flows ongoing natural transition. These modes are described by the frequency, wavelength and velocity of propagation and correspond to the primary T-S instability associated to natural transition.

The LST can be subdivided into two main branches, depending on whether additional assumptions are made. Thus, the earliest and more extensive studies on LST assumed that in addition to the linearized disturbance evolution,

the mean flow is parallel and fully developed. These assumptions taken into the Navier-Stokes and mass conservation equations lead to the Orr-Sommerfeld equation (Schlichting, 1979) which, when solved, provides the final step of the analysis. The solution of the Orr-Sommerfeld equation is limited in the literature to simple geometries including plane-Poiseuille, plane-Couette, combined plane-Couette and plane-Poiseuille, Blasius boundary layer and Falkner-Skan profiles (e.g., Betchov and Criminale, 1967; Drazin & Reid, 1991). Despite the popularity and relatively easy implementation of this analysis, the parallel assumption sometimes has been suggested as the reason of differences with experimental observations.

Most of the latest studies on stability analysis do not assume the mean flow to be parallel. For example, Fasel & Konzelmann (1990) studied the boundary layer stability in flat plate flows by solving the Navier-Stokes and mass conservation equations. Eagles & Smith (1980) used perturbation methods to study the effects of non-parallelism in the linear stability of the channel flow. Oliveira (1992) numerically investigated the linear stability of radial flows using finite volume to compute the mean flow from the steady Navier-Stokes equations and solving the derived set of linear partial differential equations for the perturbation. In general, the stability studies which consider non-parallel flow effects have shown better agreement with the experimental observations on the onset of T-S waves in natural laminar to turbulent transition.

Today, LST is considered a useful tool in validating either data from experiments or numerical codes for simple or complex geometries. In the last case, LST provides an approximation to validate the existence of primary T-S transitional instabilities.

2.2.2. Asymptotic Expansions. The asymptotic expansions in terms of a small or a large parameter have been applied to provide an approximate solution to complex non-linear equations. This approach is based on more general perturbation techniques (Nayfeh, 1981). In the approximate solution of the Navier-Stokes equations, the time and spatial coordinates are scaled in terms of a

small parameter $\varepsilon = Re^{-\sigma}$ (e.g., for boundary layer flows, $\sigma=1/8$) in the limit when $Re \to \infty$. In the study of the boundary layer flow, two main regions of interest are identified: the boundary layer itself and the outer region. One asymptotic expansion is developed for each region and both expansions are forced to match in the boundary, then forming a composite expansion. When two different regions are distinguished within the boundary layer, the composite expansion consists of two inner expansions in addition to the outer expansion. The domains of validity of each expansion are often denominated decks (Naifeh, 1981) and therefore the problem is often referred as a triple-deck problem.

In the study of the boundary layer stability, a triple-deck structure is considered with each region differentiated as: lower deck, main deck and upper deck. The lower deck is located in the layer closer to the wall in which the full Navier-Stokes equations hold. The main deck corresponds to the upper region within the boundary layer and its flow is modeled as a linearized inviscid rotational flow. The upper deck encompasses the outer region and its flow is modeled as a linearized inviscid irrotational flow. Asymptotic expansions of an interacting boundary layer with the triple-deck structure have been widely used (e.g., Goldstein, 1985a, 1985b; Goldstein & Hultgren, 1987, 1989; Heinrich et al., 1988; Kerschen et al., 1990; Kozlov & Ryzhov, 1990; Hammerton & Kerschen, 1991; Crouch, 1991). Quantitative agreement with experimental results, based on finite Re, is hardly attainable, especially in boundary layer receptivity studies (Kozlov & Ryzhov, 1990). However, the asymptotic approach has enabled the identification of general features common to different mechanisms of receptivity, which may also hold for moderate Re. The quantitative description has been achieved later either by using accurate numerical calculations in the framework of a refined model or on the basis of accurate experimental data available.

As indicated in section (2.1) on experimental results, the theoretical work shows that the receptivity, here associated to the instability wavelength modulation, takes place in regions of the boundary layer where the mean flow exhibits rapid changes in the streamwise direction. This occurs near the leading

edge or in any region farther downstream, where some local feature forces the boundary layer to adjust on a short streamwise length scale.

2.3. Numerical Investigation

2.3.1. Flat Plate. Considering the high cost of experimentation and the limitations of obtaining quantitative field data, computational models have been progressively developed leading to a better understanding of the receptivity and stability within the boundary layer on flat plate flows undergoing natural transition.

For example, the boundary layer stability in semi-infinite flat plate has been studied using finite difference Direct Numerical Simulations (DNS) by Fasel (1976, 1989) and Kloker & Fasel (1989). These studies focused on the spatial and temporal evolution of forcing time-dependent disturbances introduced to the flow field and the reaction of the flow to such disturbances. The results were in fairly good agreement with linear stability theory and experimental measurements in the description of the early stages of the laminar to turbulent transition.

The leading edge receptivity has been also numerically investigated. Studies based on finite difference DNS explored the temporal and spatial evolution of T-S waves around an elliptic leading edge (Lin et. al., 1991; Buter & Reed, 1991). These works demonstrated the presence of T-S waves starting at the ellipse-flat plate juncture. A sharper leading edge was found to be less receptive.

Spectral DNS of the boundary layer receptivity to sound waves has been done by Gatski & Grosch (1985). This study was based on an infinitely thin flat plate and the receptivity was studied around the leading edge. Results were unclear since they appeared distorted by short and long wavelength modulation of the disturbance profiles. The authors suggested the necessity of long forcing times during the simulation in order to establish an equilibrium flow over a large portion of the boundary layer and perform a reliable study of the forced receptivity.

2.3.2. Airfoil Cascades. Computational simulations have been performed to explore the dynamics of the flow in turbomachinery. For the numerical simulation of flows in annular airfoil cascades, three-dimensional (e.g., Rai, 1989; Madavan et al., 1990), quasi-3D (e.g., Baskharone & McArthur, 1990) and two-dimensional (e.g., Deconinck & Hirsch, 1981) models have been used. The two-dimensional model is based on the pattern resulting after a co-axial cylindrical section is opened and projected onto a plane. The pattern of airfoils thus obtained is known as a two-dimensional cascade, and the section between two contiguous blades is named the airfoil-to-airfoil surface.

Natural transition to turbulence in two-dimensional cascades has been investigated by Fortin et al. (1987) using DNS. Their investigation focused on the analysis of the flow dynamics using bifurcation theory and strange attractors concepts. They found a first bifurcation and an associated vortex street ejecting from the airfoil trailing edge ocurring above Re=600. Subsequent period-doubling bifurcations as Re increased to 1700 and 1900 were observed in the route to a highly chaotic scenario at Re=2200.

Numerical studies at low Re found similarities in the qualitative features of unsteady flows compared to the data obtained at much higher Re within airfoil cascades. For example, Baskharone & McArthur (1990) modelled the flow-governing equations by introducing in the elliptic term an accurate approximation of the shear stress components that are created by the spanwise velocity gradients. Their computed quasi-three dimensional distribution of non-dimensional pressure and flow exit angle for a gas turbine stator blade at Re=2000 were compared to experimental data at $Re=2.58x10^5$ obtained with the same geometry. Both results were in good qualitative agreement. Similar results were obtained by Renaud (1991). He performed DNS of three-dimensional flows through axial turbine cascades. The numerical predictions at Re=1000 reproduced the qualitative aspects of experimental flow measurements on the same cascades at $Re=5.9x10^5$. Good agreement was found in the locations of saddle and separation points, total pressure loss distributions and separated

region size. The major differences between the numerical and experimental results were the thickness of the boundary layer and the severeness of the blade surface separation observed in the computed results.

2.4. Previous Work on Fluctuating Kinetic Energy Transport

The Fluctuating Kinetic Energy (FKE) equation has been extensively used in the evaluation of turbulent flows characteristics, in which case is named Turbulence Kinetic Energy (TKE) equation. For example, Humphrey & Whitelaw (1980) considered the production term in the transport equation for the Reynolds stresses in the context of discussing turbulent flow in non-circular ducts with rough walls. Goel & Amano (1986) investigated the mean and turbulence kinetic energy equations in turbulent flow over a step. They concluded that the production and dissipation rates of the turbulence energy predominate in the region upstream of the reattaching point and decay rapidly downstream whereas the convection and diffusion rates do not change appreciably in the streamwise direction. Hirota et al. (1992) considered the TKE production and convection for flows through square ducts with rib-roughened walls. They found that the Reynolds shear stresses play the most important role in the production of TKE both in smooth and rough ducts although, near the rough wall, the contributions of the normal and shear Reynolds stresses were almost of the same magnitude. Lyons & Hanratty (1991) and Kasagi et al. (1992) considered the budget of the TKE equation in fully-developed turbulent plane-channel flows and found that, away from the wall, production balances dissipation. Kim (1988) and Kasagi et al. (1992) discussed the budgets of Reynolds stresses and heat fluxes in plane-channel flows, and observed a strong correlation between the temperature fluctuations and the streamwise velocity fluctuations. Reynolds (1974) introduces in his book the experimental results by Townsend (1956, 1970) on the TKE distribution across a turbulent wake and in the outer part of a constant-pressure boundary layer. Common features found in both cases are: a) dissipation is negative everywhere (lost of energy); b) production has the opposite sign and is maximum where the velocity gradients

are largest; c) diffusion is, in general, from a region of high intensity to one of low intensity; in each case, it is towards the spreading boundary in the outer part of the shear layer. Some differences in the two energy balances are: a) in the wake, there is no region where dissipation and production are dominant; b) mean-flow convection is significant only in the outer half of the boundary layer but is important throughout the wake. All these budget equations were considered only at certain streamwise locations as a function of the transverse direction in a simple geometry and for high Re flows with the solely interest of studying turbulence features.

Majumdar & Amon (1997) recently presented results of the study of the oscillatory momentum transport in transitional flows within communicating channels. The objective of their work was to identify mechanisms responsible for sustaining the fluctuating flow by evaluating the FKE terms from the velocity and pressure obtained via DNS of the governing equations. They found that the pressure fluctuation and the production terms are mainly responsible for the exchange of energy between the mean and the fluctuating flow. The pressure fluctuation contributes to sustaining the flow fluctuations in the vortical communicating region whereas the production term is mainly responsible for sustaining the FKE in the near-parallel channel flow.

No research has been performed, previously to our investigation, either on the boundary layer receptivity and stability in axial airfoil cascade flows or on the use of the FKE budget to interpret the nature of the onset of natural transition and the spatial evolution of T-S waves. Our investigation addresses these fundamental issues by performing DNS of the governing equations and computing the terms from the FKE budget throughout the entire flow domain. Budgets at locations across the boundary layer enable identification of the formation and evolution of T-S waves and the effects caused by monochromatic controlled disturbances superposed at the entrance of the flow.

CHAPTER 3

OBJECTIVES AND SCOPE OF THIS INVESTIGATION

The purpose of this investigation is to study the boundary layer receptivity and stability to natural and superimposed free-stream disturbances within cascade flows. The cascade geometry chosen for our study corresponds to the midspan airfoil-to-airfoil surface of an experimental axial stator (Dring et al., 1988). The investigation is divided into three major parts: (a) study of the receptivity and subsequent evolution of T-S primary waves within the separated boundary layer in an unperturbed or basic unsteady flow; (b) study of the boundary layer receptivity to forced free-stream disturbances superposed to basic steady flows; and (c) study of the interaction between the boundary layer naturally-generated T-S waves and forced free-stream disturbances superposed to basic unsteady flows.

In fulfilling the main objectives of our research, we planned a layout of numerical simulations sub-divided into basic flow and perturbed flow simulations. The basic flows range from steady-state regimes to self-sustained oscillatory regimes. The perturbed flows result from the introduction of monochromatic time-harmonic disturbances at the inlet boundary of the flow domain.

To study the generation of T-S waves and their further evolution within basic and perturbed flows, we propose the direct observation of the fluctuating flow field and the evaluation of the FKE budget. We believed that since the FKE budget encompasses the transport, production and dissipation of fluctuating kinetic energy within the fluid flow, it could provide insightful information on the receptivity and the stability of the boundary layer.

Direct Numerical Simulation of the Navier-Stokes and mass conservation equations is utilized as the numerical approach for solving the problem. The proposed numerical method is based on spectral element spatial discretization

and a semi-implicit finite difference temporal discretization. High-order spectral elements are advantageous for this research because of the exponential convergence and typical high resolution close to the wall where transitional waves are more likely to be generated.

Evidence of important qualitative features of high Re cascade flows being satisfactorily reproduced within low Re simulations (e.g., Baskharone & McArthur, 1990; Renaud, 1991), motivated us to expect that results feasible with DNS at low Re would improve the understanding of the initial stages of natural transition within boundary layers in high Re engineering flows.

CHAPTER 4

PROBLEM FORMULATION AND METHOD OF SOLUTION

4.1. Modeling and Mathematical Formulation

Until recently, most of the numerical investigations on transitional flows had focused on the study of flat plate boundary layers and on fully-developed internal flows. The flow within the airfoil-to-airfoil surface differs from the typical flat plate flow because of the high pressure gradient and the steep change in surface curvature. Moreover, because of the bounded geometry of the airfoil-to-airfoil surface, the stability characteristics might be closer related to those encountered along the entrance region for a channel flow. However, leading edge and curvature effects would make it a too simplified model. Therefore, to study the receptivity and stability of the boundary layer in a cascade geometry, we resorted to use the actual geometry.

4.1.1. Description of the Physical Model. This research addresses the numerical study of the boundary layer receptivity and stability in an incompressible, viscous flow through the midspan axial-stator airfoil-to-airfoil surface. The two-dimensional physical domain, shown in Fig. 1, corresponds to a low-solidity-ratio, experimental axial gas turbine first stator (Dring et al., 1988). In addition to the airfoil-to-airfoil passage, the geometry under consideration includes upstream and downstream extensions to account for the inflow and the wake regions, respectively. The airfoils have chord length c of 0.21m (0.7ft), axial blade chord c_x of 0.153m (0.503ft), pitch h of 0.20m (0.64ft), solidity ratio s_r=h/c of 0.914, and angles of stagger β and attack α of 45 degrees, each.

The two-dimensional model used in our investigation has a relatively low computational cost compared to an equivalent three-dimensional model. It is partially justified since data from previous experiments on this geometry at even higher Re, indicate a nearly two-dimensional flow at the midspan section of the stator blades (Dring et al., 1988). However, the two-dimensional model is

expected to predict higher pressure loading and thicker boundary layer in the suction side of the blade because this model does not account for the spanwise pressure drop and secondary flow which causes a migration of blade boundary layer fluid toward the midspan region. The two-dimensional model is also justified because the earliest stage of the boundary layer natural transition consists on the evolution of dominant two-dimensional instabilities in accordance to Squire's theorem and experimental observations (Schlichting, 1979). Therefore, we believe that the spanwise-averaged values provided by two-dimensional simulations should enable us to understand the main aspects of the receptivity phenomenon and the primary instability evolution before three-dimensional effects become important. Nevertheless, selected three-dimensional simulations are performed to partially evaluate and validate the two-dimensional results.

4.1.2. Measurement of the Receptivity and Stability. The study of the boundary layer receptivity involves the flow investigation around the region where the instability wavelength modulation occurs. The receptivity is evaluated by quantifying the instability amplitude and the mean flow variations. For basic flows, the study considers the boundary layer receptivity to naturally generated disturbances within the flow as a consequence of the interaction of the incoming stream and the blade leading edge. The examination of the perturbed flow considers the boundary layer receptivity to time-harmonic monotonic perturbations convecting from the entrance of the computational domain. Various frequencies and amplitudes are considered in the study of perturbed flows.

The boundary layer stability is evaluated by measuring its ability to dampen or enhance disturbances traveling within the boundary layer. These disturbances include the naturally-generated instabilities above Re_c and perturbations artificially superimposed. Although disturbances that exist in real flows are finite in amplitude and stochastic in nature, it is convenient, in order to draw fundamental observations, to study the perturbed flow characteristics under the effect of a monochromatic time-oscillatory disturbance.

4.1.3. Mathematical Model. The continuous problem is formulated using the Navier-Stokes and mass conservation equations in non-dimensional form:

$$\frac{\partial \vec{u}}{\partial t} + \vec{u}.\nabla\vec{u} = -\nabla p + \frac{1}{\mathrm{Re}}\nabla^2\vec{u} \quad \text{in } \partial\mathrm{D} \tag{1}$$

$$\nabla.\vec{u} = 0 \quad \text{in } \partial\mathrm{D} \tag{2}$$

where, ∂D is the computational domain and the non-dimensionalization is given in the nomenclature section. The mathematical problem is subject to the following boundary conditions:

a) inflow

a.1) basic flow

$$u_{H-A} = 1 \; ; \; \mathrm{v}_{H-A} = 0$$

a.2) perturbed flow

$$u_{H-A} = 1 + u' \; ; \; \mathrm{v}_{H-A} = 0$$

where, $u' = \varepsilon.\sin(\omega_d.t)$

b) outflow

$$\left.\frac{\partial u}{\partial x}\right|_{(D-E)} = 0$$

$$\left.\frac{\partial v}{\partial x} + \frac{\partial u}{\partial y}\right|_{(D-E)} = 0$$

c) blade wall

$$u_{B-C} = u_{G-F} = 0$$

d) meridional bounds

$$u_{A-B} = u_{G-H} \; ; \; u_{C-D} = u_{E-F}$$

$$\mathrm{v}_{A-B} = \mathrm{v}_{G-H} \; ; \; \mathrm{v}_{C-D} = \mathrm{v}_{E-F}$$

The reference corners A through H are depicted in Fig. 1.

4.2. Numerical Methodology

As computer speed and memory capabilities increase, and improved computational algorithms and numerical techniques are developed, DNS has become a useful tool in the study of the transition from laminar to turbulent regime within complex geometries. The accuracy of DNS is provided by the numerical approximation within the temporal discretization of the governing equations and the spatial discretization of the computational domain. In fluid dynamics, despite DNS being currently limited to modest Re which are usually low for many engineering applications, these simulations have proven to be useful in investigating nonlinear interaction in transitional and weakly turbulent flows (e.g., Deane & Mavriplis, 1991; Tan, 1989; Amon & Patera, 1989).

The computational domain is represented as a set of macro-elements with the solution and geometry approximated by high-order Legendre polynomial expansions within each macro-element. The spatial discretization of the domain is conducted using the spectral element technique (Patera, 1984; Korczag & Patera, 1986; Amon, 1993). The spectral element technique is a high-order, weighted-residual technique that combines the geometric flexibility of the finite element technique with the accuracy and rapid convergence of spectral methods.

The temporal discretization of the Navier-Stokes equations must accomplish three major objectives. First, limitations in computer time suggest that the non-linearities be treated explicitly, that is, the convective term should be calculated from values of the velocity from the previous time steps. Second, the viscous term should be treated implicitly to avoid unreasonable time-step restrictions. These time-step restrictions would be prohibitive because of the high resolution of spectral techniques adjacent to boundaries (Gottlieb & Orszag, 1977). Finally, the pressure should also be calculated implicitly, because of the divergence-free velocity imposed at each time step. In response to these needs, a time-stepping scheme based upon a consistent choice of approximation spaces for the pressure and velocity within the semi-discrete formulation of the time-dependent term in the Navier-Stokes equations is used. The complete solution of the Navier-Stokes equations involves first treating the wave-like equation for the non-linear

convective terms explicitly, and then solving the resultant Stokes problem at each time-step with an Uzawa iterative procedure (Rønquist, 1988). The following two sub-sections describe the discretization procedure.

4.2.1. Spatial Discretization. For two-dimensional domains, the isoparametric spectral element spatial discretization proceeds by first breaking the domain into non-degenerate quadrangles, named macro-elements. Three-dimensional domains are broken up into hexahedral or brick elements, named also macro-elements, of which each face corresponds to a non-degenerate quadrangle. The macro-elements are iso-parametrically mapped from the physical into the computational space. Within each macro-element, a local Cartesian mesh is constructed corresponding to a NxN(xN) tensor-product Gauss-Lobatto-Legendre collocation points. The Gauss-Lobatto points are clustered near elemental boundaries and are chosen because of their accurate approximation, interpolation and quadrature properties.

The convective step is formulated using a pseudo-spectral (collocation) approach. This allows for economical treatment of the non-linear velocity terms. For the viscous and pressure steps, the discrete equations are obtained for each element by inserting the interpolants and the transformed nodal collocation values into the variationally-formulated form of the equation. Then, a Galerkin, weighted-residual technique is implemented. The resulting equations are integrated, requiring stationarity at the collocation points. Once the system of discrete equations is obtained for each element, the global matrix is constructed using direct stiffness summation.

Assembly of the global matrix is accomplished using parallel static condensation in which the nodes, and their corresponding degrees of freedom, are decoupled into those lying on the boundary of elements and those interior to an element. The boundary nodes are determined first by inverting the condensed system, which is of greatly reduced rank, and then, the interior nodes are computed.

In most of the two-dimensional simulations a mesh with 784 macro-elements and 25 nodes per macro-element is used. Computed results for the same number of elements and 49 nodes demonstrating the mesh-independence of the results are also included. This mesh refinement study indicates that the coarser mesh is appropriate to resolve the smallest length-scale phenomena present in the flow for the range of Re explored in the investigation. The element subdivision of the spectral element mesh for the airfoil-to-airfoil surface of three contiguous airfoils is displayed along with the collocation points in Fig. 2.

4.2.2. Temporal Discretization. The temporal discretization is accomplished using consistent approximation spaces for the pressure and velocity to ensure a well-posed formulation for the resulting, implicit Stokes problem (Fischer, 1989). The convective term is treated explicitly by a third-order Adams-Bashforth multi-step scheme and the viscous term implicitly by a first-order backward differentiation scheme. The velocity divergence-free constraint is imposed at each time step, so the pressure is computed implicitly using the Uzawa algorithm.

To satisfy the Ladyzhenskaya-Brezzi-Babuska or inf-sup condition, which guarantees the existence of a unique (Temam, 1977; Canuto et al., 1988) and stable (Gunzburger, 1989) solution, the associated trial functions for the pressure are polynomials of degree N-2 rather than the N-degree polynomials used for the velocity. The trial functions are based upon Gauss quadrature points for the pressure, whereas Gauss-Lobatto for the velocity (Rønquist, 1988). This formulation has the significant feature that the approximation for the pressure does not extend to the macro-element boundaries. Hence, no apriori pressure boundary conditions are required when solving (1) and (2), as it is physically the case.

The Uzawa solution scheme for the current problem applies a variational procedure to the non-dimensionalized governing equations and boundary conditions (1) and (2). Therefore, a discrete system of equations in the two-

dimensional domain for the velocity and pressure at time step n+1 is obtained (Fischer, 1989):

$$\begin{bmatrix} \frac{1}{\mathrm{Re}}A+\frac{1}{\Delta t}B & 0 & -D_1^T \\ 0 & \frac{1}{\mathrm{Re}}A+\frac{1}{\Delta t}B & -D_2^T \\ -D_1 & -D_2 & 0 \end{bmatrix} \begin{Bmatrix} \mathrm{u}^{n+1} \\ \mathrm{v}^{n+1} \\ p^{n+1} \end{Bmatrix} = \begin{Bmatrix} \left(\frac{\mathrm{B}}{\Delta \mathrm{t}}\mathrm{u}^n + AB_1^n\right) \\ \left(\frac{\mathrm{B}}{\Delta \mathrm{t}}\mathrm{v}^n + AB_2^n\right) \\ 0 \end{Bmatrix} \tag{3}$$

where A is the mixed discrete Laplace-pressure operator, $\mathrm{D_i}$ is the derivative operator associated with the ith-direction, B is the mass matrix and AB is the Adams-Bashforth scheme over the nonlinear term given by:

$$AB_i^n \equiv \sum_{q=0}^{2} \alpha_q \left(u_i^{-n-q}.\nabla u_i^{-n-q}\right).\hat{e}_i \quad ; \quad \mathrm{i=1,2} \tag{4}$$

$$\alpha_0 = 23/12 \qquad \alpha_1 = -16/12 \qquad \alpha_2 = 5/12$$

where u_1 represents u and u_2 represents v, the x- and y-components of the non-dimensional velocity, respectively.

Block Gaussian elimination is performed on (3) to decouple the pressure and velocity into three systems of equations.

The pressure can be solved directly at each time-step from,

$$Ep = -\sum_{i=1}^{2} D_i \left(\frac{1}{\mathrm{Re}}A+\frac{1}{\Delta t}B\right)^{-1} AB_i^n \tag{5}$$

where,

$$E = \sum_{i=1}^{2} D_i \left(\frac{1}{\mathrm{Re}}A+\frac{1}{\Delta t}B\right)^{-1} D_i^T \tag{6}$$

The velocity is computed with two additional solves of the elliptic modified Helmholtz operator, $\left(\frac{1}{\mathrm{Re}}A+\frac{1}{\Delta t}B\right)$.

The matrix *E* is ill-conditioned, requiring a pre-conditioner based upon additional A solves (Fischer, 1989). The iterative, conjugate gradient method is

an appropriate means of solving the system (5). The scheme, as presented, is first-order accurate in time, however, the third-order Adams-Bashforth treatment of the convective operator is used because of the relatively large portion of the imaginary axis which lies within its stability region (Gear, 1971).

4.3. Data Manipulation Strategy

Our study required the accurate representation of the time-averaged and time-dependent flow fields within the entire domain. The time-averaged or mean flow distribution usually is expected to reflect the degree of flow destabilization. The flow instabilities are visualized through the temporal and spatial distribution of the fluctuating field. The temporal distribution of the fluctuating field at selected locations allows us to measure the oscillatory frequency of the instabilities, while the representation of the spatial evolution of the instabilities helps to visualize the wavelength modulation phenomenon, i.e., the transformation of the long-wavelength instability into the T-S wave. The next sub-sections describe briefly how the mean and fluctuating parameters are computed, the technique used in the determination of the oscillatory frequency and the description of the Fluctuating Kinetic Energy (FKE) equation.

4.3.1. Mean and Fluctuating Components of the Flow Field. The mean or time-averaged fields are computed by performing simulations starting from asymptotically-converged cases and then, the data is accumulated and averaged within one period of the flow oscillation. Previous determination of the frequency of oscillation is a fundamental step in fulfilling this objective. Hence, the fluctuating fields are computed by subtracting the mean field from the instantaneous field.

4.3.1.1. Calculation of derivatives. The computation of the shear stress, vorticity and FKE terms involves the spatial derivatives of the flow field. The derivatives are computed spectrally at every time-step through matrix multiplication. Scalar components (x-velocity, y-velocity and pressure) are represented as N^{th}-order polynomials, $g(\xi,\eta)$ on the two-dimensional mapped domain, within $\xi,\eta \in [-1,1]$. This polynomial is expanded as:

$$g(\xi,\eta)=\sum_{j=0}^{N}\sum_{i=0}^{N}g(\xi_i,\eta_j).h_i(\xi).h_j(\eta) \tag{7}$$

The Lagrangian interpolants, $h_j(\xi)$ are N^{th}-order polynomials such that :

$$h_j(\xi_i)=\delta_{ij} \quad \text{for all (i,j)} \in \{0,...,N\}^2 \tag{8}$$

The nodal Lagrangian-Legendre interpolants, h_j, can be written as :

$$h_j(\xi)=\frac{(1-\xi^2)L_N'(\xi)}{N(N+1)L_N(\xi_j)(\xi-\xi_j)} \tag{9}$$

where $L_k(\xi)$, k=1,2,3,... is the Legendre k^{th}-order polynomial :

$$L_k(\xi)=\begin{cases}1 \quad for\ k=0\\ \xi \quad for\ k=1\\ \xi.L_{k-1}-\dfrac{(k-1)^2}{(2k-1).(2k-3)}L_{k-2}\end{cases}$$

and

$$L_k'(\xi)=\frac{(k.\xi.L_k-k.L_{k-1})}{(\xi^2-1)}$$

(' denotes differentiation.)

The local Gauss-Lobatto-Legendre collocation points are related to the global physical coordinates x and y by :

$$\begin{aligned}&\xi_0,\eta_0=-1\\ &\xi_i,\eta_i(i=1,\ldots,N-1)=\ zeroes\ of\ L_N'\\ &\xi_N,\eta_N=1\end{aligned} \tag{10}$$

Next, the spatial derivatives as a function of the local derivatives are computed. The first local partial derivatives of the polynomial $g(\xi, \eta)$ are given by :

$$\begin{aligned}\frac{\partial g(\xi,\eta)}{\partial\xi}&=\sum_{j=0}^{N}\sum_{i=0}^{N}g(\xi_i,\eta_j).\frac{\partial h_i(\xi)}{\partial\xi}.h_j(\eta)\\ \frac{\partial g(\xi,\eta)}{\partial\eta}&=\sum_{j=0}^{N}\sum_{i=0}^{N}g(\xi_i,\eta_j).h_i(\xi).\frac{\partial h_j(\eta)}{\partial\eta}\end{aligned} \tag{11}$$

4.3.1.2. Determination of the separation and reattachment points. The location of the points over the airfoil suction wall where the boundary layer detaches and reattaches is determined as a function of time by computing the shear stress on the blade wall. The non-dimensional wall shear stress is computed as :

$$\tau_w = \left(\frac{\partial u_t}{\partial n} + \frac{\partial u_n}{\partial t} \right) \tag{12}$$

where, the indexes 'n' and 't' denote normal and tangential to the wall, respectively. Since close to the wall the flow is quasi-parallel, the wall shear stress measures the velocity gradient normal to the wall. Therefore, the shear stress is positive before the separation, becomes zero at the separation, and is negative within the separated region.

4.3.1.3. Shear stress and vorticity. To determine the degree of deformation and rotation of fluid elements within the boundary layer, as these characteristics might be related to the degree of destabilization achieved naturally or artificially, we compute the x-y shear stress τ_{xy} and the z-component of the vorticity ω_z, respectively. These non-dimensional parameters are computed as :

$$\begin{aligned} \tau_{xy} &= \left(\frac{\partial u}{\partial y} + \frac{\partial v}{\partial x} \right) \\ \omega_z &= \left(\frac{\partial v}{\partial x} - \frac{\partial u}{\partial y} \right) \end{aligned} \tag{13}$$

4.3.1.4. Computation of the boundary layer thickness. The boundary layer thickness δ and its growth in the streamwise direction are determined by the condition of having the boundary layer limit at the point where the vorticity equals 1% of the vorticity on the wall, following lines perpendicular to the airfoil surface.

4.3.2. Fast Fourier Transform. A physical time-varying process can be described either in the time domain by the values of some quantity h (e.g., velocity or pressure) as a function of time h(t), or else in the frequency domain where the process is specified by giving its amplitude H (generally a complex

number indicating also phase) as a function of frequency, i.e., H(f). The connection between these two representations is given by the Fourier transformation.

In the most common situations the function h(t) is sampled at evenly spaced intervals in time. The data is manipulated and analyzed via Discrete Fourier transformation (DFT). DFT is efficiently accomplished through Fast Fourier transformation (FFT). In the framework of this research, FFT is used in the analysis of the velocity components as a function of time. The frequency spectrum obtained through FFT gives the fluctuating modes present within basic and perturbed flows.

4.3.3. Fluctuating Kinetic Energy (FKE) Budget. As one of the fundamental contributions of this investigation, we evaluate the energy exchange between the flow instabilities and the mean flow. This includes the energy necessary to maintain the flow oscillations and the diffusion and dissipation of that energy. The kinetic energy equation for the fluctuating components of the velocity and pressure (14) results from the time-averaged manipulation of the momentum and mass conservation equations, departing from the Reynolds decomposition (Hinze, 1987). This equation represents the conservation of FKE in the elementary control volume depicted in Fig. 3 (Bradshaw, 1975). Equation (14) states that within an elementary control volume the balance among the diffusive transport of FKE by the fluctuations, the work of the fluctuations to diffuse through the viscous field, the production and dissipation must equal the time rate of increase of FKE and the convective diffusion of FKE by the mean flow. This equation is expressed in non-dimensional form as:

$$\underbrace{\frac{D}{Dt}\overline{q'}}_{T1,T2} = \underbrace{-\frac{\partial}{\partial x_i}\overline{u'_i\left(p'+q'\right)}}_{T3} \underbrace{-\overline{u'_i u'_j}\frac{\partial U_i}{\partial x_j}}_{T4} + \underbrace{\frac{1}{\mathrm{Re}}\frac{\partial}{\partial x_i}\overline{u'_j\left(\frac{\partial u'_i}{\partial x_j}+\frac{\partial u'_j}{\partial x_i}\right)}}_{T5} \underbrace{-\frac{1}{\mathrm{Re}}\overline{\left(\frac{\partial u'_i}{\partial x_j}+\frac{\partial u'_j}{\partial x_i}\right)\frac{\partial u'_j}{\partial x_i}}}_{T6}$$

$$\Downarrow$$

$$T1 = \frac{\partial}{\partial t}\left(\frac{u'_i u'_i}{2}\right)$$

$$\mathrm{T2} = \frac{\partial}{\partial x_i}\left(U_i \frac{u'_j u'_j}{2}\right) \qquad (14)$$

where,

q' : fluctuating kinetic energy FKE=$(u_1'^2+u_2'^2)/2$

$-u'_iu'_j$: fluctuating (Reynolds) shear stress

U_i : time-averaged velocity

T1 : time rate of increase of FKE

T2 : convective diffusion of FKE by the mean flow

T3 : work of the total dynamic pressure of the fluctuations

T4 : production of FKE

T5 : work of the viscous shear stresses of the fluctuations

T6 : viscous dissipation of FKE

Terms T1-T6 are non-dimensionalized by c / U_∞^3.

We validated the kinetic energy subroutine in two ways. First, the sum of the fluctuating components of the velocity, Σu′ and Σv′, within one period of the flow fluctuation must be very small (e.g., in the order of the machine round-off error); and second, the sum of terms T3 through T6 must be approximately, within the round-off error of the machine, equal to T2. The second validation was performed within the suction-side boundary layer and the quasi-potential

region between the two airfoils. The validation confirmed that T1 is neglegible as it should be for asymptotically converged flows.

All the terms, except T1, are computed from the velocity and pressure fields numerically calculated from the governing equations. After demonstrating that T1 is negligible and given that T3 is very sensitive to the large velocity and pressure gradients close to the airfoil walls, we decided to drop T1 from (14) and obtain T3 from the algebraic balance of the equation.

The analysis based on the FKE budget allowed us to further the study on the two identified forms of transitional wave generation or receptivity; one related to Re_c and the other related to the monochromatic time-harmonic perturbation. The discussion of the energy transfer mechanisms for these two forms of receptivity provides a complementary explanation to the receptivity phenomenon since it addresses the issue of how the long wavelength instabilities and the short wavelength transitional instabilities exchange and transform energy. The FKE budget also permitted us to characterize the energy exchange and transformation associated to the T-S wave evolution.

In the analysis of turbulent flows, the equation (14) suggests a cascade path of energy exchange or transformation (Hinze, 1987). The sequential transformation of energy until it is dissipated is explained as the mean flow releases energy to the turbulent fluctuations at large scales and these fluctuations dissipate energy at very small scales. This can be also understood through the interaction between mean motion and fluctuations in which energy is extracted from the mean motion through work of deformation against the Reynolds shear stresses, converted into turbulence energy and then partially converted through work of deformation of the viscous shear stresses into heat. Part of the energy gained at large scales by the flow fluctuations may also be convected and diffused along with the mean motion, thus, balancing (14).

In turbulent flows, the dissipation of energy at small scales occurs only if there exists a dynamical mechanism that transfers energy from large scales to small scales. This mechanism is the vorticity (Tennekes & Lumley, 1972) and it is

connected to the generation of Reynolds stresses through the transport and stretching of vorticity due to the mean motion (Hinze, 1987). The relatively low Re regimes, compared to engineering applications, provided a weakly transitional flow in which viscous shear stresses are expected to be in the same order of magnitude if not larger than the Reynolds shear stresses. Therefore, the cascade path for the energy transformation, based on the existence of the intrinsically three-dimensional vortex stretching phenomenon, was not accounted for in the analysis.

From the expressions of the energy terms in (14), it is possible to predict some features of the energy exchange within the flow. For example, the production of FKE, T4, may be affected in two different ways : when $i \neq j$, T4 usually gives a positive contribution to the kinetic energy of the instabilities (Hinze, 1987). Lin (1955) demonstrated that viscous effects at the wall lead to a phase shift between the streamwise and the transversal velocity components of a two-dimensional disturbance, and consequently to a positive value of the Reynolds shear stress $-\rho\overline{u_1' u_2'}$. Since close to the wall, except for separated regions, $\partial U_1/\partial x_2 > 0$, a positive value of the production T4 is expected near the airfoil surfaces within the boundary layer. When $i=j$, T4 tends to be negative for spatially accelerated flows and positive for retarded flows; therefore, a decrease of static pressure in the flow direction (favorable pressure gradient) inhibits the fluctuations and an increase in static pressure (adverse pressure gradient) promotes flow fluctuations.

CHAPTER 5

RESULTS AND DISCUSSION

5.1. Flow Field Dynamics

This section presents the numerical results on the receptivity and stability study for basic flows and for perturbed flows. The results include global flow visualization, as well as time-averaged and oscillatory field distributions within the boundary layer close to the airfoil wall. Linear stability analysis is performed using the parallel plate geometry for the same Re and the most unstable modes are used as a reference to confirm the generation of T-S waves. The receptivity, measured as the interaction between the external disturbances and the boundary layer, is globally visualized and locally quantified from time-averaged effects occurring in the fluctuating field. Results from the mesh dependence study of the computed flow fields are also included to justify the two-dimensional mesh used in our simulations. A survey with the performance of the numerical code running on several platforms is included in Table I.

At the end of this section, we present a comparison between numerical predictions for the mean basic flow at Re=1000 and experimental data based on a similar geometry at Re=5.9×10^5. Despite the difference between the two Re, this comparison intends to explore the qualitative similarities between the numerical and experimental flow fields.

The simulations covered steady-state and self-sustained fluctuating basic flows in the Re range of 231-1000. The superposed disturbance frequency $\omega_d=\omega_d^*.c/U_\infty$ and amplitude $\varepsilon=\varepsilon^*/U_\infty$ vary within 8.8-1100 and 0.005-0.02, respectively. The frequency range includes the natural frequency, $\omega_n \approx 29.6$, observed in the self-fluctuating flow for Re=1000, allowing us to study the flow at lower and at several orders of magnitude higher forcing frequencies. The range of the disturbance amplitude extends from a relatively small to a moderate

intensity, compared to the amplitude of the fluctuations observed within the self-sustained basic fluctuating flows.

5.1.1. Basic Flow. A typical pressure field found in the airfoil cascade is shown in Fig. 4 for Re=1000. It depicts the characteristic favorable pressure gradient (FPG) along the quasi-potential flow region and over the pressure side of the airfoil. Along the suction side, the boundary layer is subject to an entrance region under FPG. The pressure gradient becomes adverse after the minimum pressure point (MPP) is reached at about 40% of the axial blade chord from the leading edge.

Figure 5 shows the boundary layer thickness δ, non-dimensionalized by the blade chord c, along the airfoil suction-side wall. The distribution depicts a faster growth within the adverse pressure gradient (APG) region compared to the growth under FPG. The adjusted expressions for δ/c as a function of the non-dimensional arclength s/c and the arclength-based Reynolds number Re_s are summarized in Table II.

5.1.1.1. Boundary layer separation and flow bifurcation. Figure 6 shows streamtraces for basic flows at Re=231 and Re=1000. For Re=231, the boundary layer remains attached to the airfoil wall. For Re>400, the strong APG causes the suction-side boundary layer detachment downstream the MPP, and reattachment occurs close to the trailing edge. For Re=400, the boundary layer separation and reattachment points (SP and RP, respectively) are stationary and no signs of vortex shedding are observed. However, for the same Re, small fluctuations are noticed in the time domain, indicating the onset of a bifurcation from steady-state to self-sustained fluctuating flow. For Re=1000, temporal flow fluctuations are more evident and a spatial wavy pattern along with incipient vortex shedding are observed (see Fig. 6b).

5.1.1.2. Visualization of T-S waves. A spatial distribution of the fluctuating magnitude of the velocity, hereafter called the speed Sp', at a characteristic time for Re=1000 is shown in Fig. 7. Fig. 7a depicts the cascade wake unsteadiness,

while Fig. 7b depicts the propagation of short wavelength instabilities downstream the MPP within the suction-side boundary layer.

The temporal evolution of the fluctuating component of the speed, Sp', for Re=1000 is depicted in Fig. 8 at eight locations along the suction side boundary layer, at a distance $d_n/c=0.0115$ from the blade wall. The instabilities generate and start slowly growing around the leading edge. Nearby the MPP, the growth of the instability becomes exponential and reaches a peak slightly upstream of the SP. Then, the amplitude decreases approximately 50% until the SP where a local minimum occurs. Between the peak and the minimum at the SP, as we show subsequently, a wavelength modulation occurs. The instability wavelength drastically shortens and the amplitude grows again exponentially at a rate much faster than before, reaching a maximum at about 20% of c_x from the trailing edge. Thereafter, viscous effects imposed by a rapidly growing and thick boundary layer damp out the instability amplitude before it reaches the trailing edge.

The oscillatory frequencies of the instabilities are obtained from Fourier power spectra of the time-dependent velocities at characteristic spatial locations P1, P2 and P3 indicated in Fig. 1. The Fourier spectrum of the x-velocity component at location P1 corresponding to basic or unperturbed flow for Re=1000 is shown in Fig. 9. A dominant mode of frequency $\omega=29.6$, named hereafter natural frequency ω_{2D_1000}, is observed. The same frequency is detected at other locations (P2 and P3) but with lower amplitudes. Location P1, shown in Fig.1, is close to the region where the wavelength modulation takes place. P2 is located at the entrance of the cascade passage and only captures by diffusion the unsteadiness associated to the boundary layer fluctuations. P3, though located within the suction side boundary layer, is far downstream the modulation point, close to the trailing edge where the instability interacts with the highly unsteady wake. Table III presents, as a reference, the dimensional values of the natural frequency ($\omega^*_{2D\_1000}$) and the free-stream velocity (U_∞) for Re=1000, using the air properties at room temperature.

Linear stability analysis of the Orr-Sommerfeld equation using the parallel-plate geometry allowed us to estimate a range for the frequencies of the least stable mode for the airfoil cascade geometry. The non-dimensional frequency of the least stable mode ω_{LS}, listed for various Re in Table IV, agreed in the order of magnitude with the fluctuating frequency of the computed instability, partially confirming that it corresponds to a primary transitional instability, i.e., a T-S wave. A second evidence is based on the observed wavelength modulation phenomenon itself. The spatial wavelength modulation is depicted in Fig. 10 in the plot of Sp' vs x close to the suction-side wall at three different times. This figure shows the initial long wavelength instability triggered around the leading edge. The subsequent instability evolution occurs with this initial wavelength until it reaches the MPP. Between the MPP and the SP, a gradual conversion of the wavelength occurs. The APG promotes the growth of the instability though, as it approaches the SP, while the wavelength is drastically reduced, the amplitude of the instability is forced to decay. This result is in agreement with extensive experimental (e.g., Kachanov et al., 1982; Nishioka & Morkovin, 1986) and theoretical (e.g., Kerschen, et al., 1990; Goldstein & Hultgren, 1987, 1989) studies which have shown that the instability wavelength modulation process giving rise to T-S waves takes place in regions of the boundary layer where the mean flow exhibits rapid changes in the streamwise direction. Therefore, our conclusion of being in presence of the very beginning of the transition is reinforced. In addition, the high Re experiments done by Dring et al. (1982) with the same cascade geometry used in this work, although did not prove boundary layer separation, indicated the existence of T-S waves close downstream of the MPP within the suction-side boundary layer.

5.1.1.3. Origin of the T-S waves. Figure 11 shows contour plots of the fluctuating component of the speed, Sp', at four times within the fundamental period of fluctuation. This sequence of events demonstrates the interconnection between the vortex shedding and the generation of T-S waves. Vortices are ejected from the airfoil trailing edge as the response to the continuous relaxation-

contraction of the unsteady bubble which at the same carries the T-S waves convecting from the SP. The momentum of the ejected vortices is partially diffused upstream towards the suction wall of the lower airfoil driven by the APG and contributes to the wavelength modulation process and the subsequent evolution of the T-S waves. From Fig. 11 it is apparent that the wavelength modulation occurs as the consequence of the refraction suffered by the long wavelength instability generated at the leading edge when approaching the separated bubble. The long wavelength instability when nearing the separated bubble encounters a relatively high resistance offered by the recirculation and then, at the entrance of the bubble, the instability is required to diminish its phase speed and consequently to reduce its wavelength. To corroborate this hypothesis, a similar analysis was performed on the flow for Re=600. This Re is high enough above Re_c to show moderate time dependency, but small enough to have a reduced separated bubble compared to the case for Re=1000. The flow natural frequency of fluctuation captured via Fourier analysis at P1 (see Fig.1 for location) is ω_{2D_600}=24.4. Figure 12 shows contour plots of Sp' at four times within one period of the natural fluctuation. From this figure we may conclude the following: (a) at Re=600, despite having a markedly different separation point compared to Re=1000, the intensity of the fluctuations within the boundary layer are larger around the leading edge; (b) the long wavelength instability generated at the leading edge is affected by diffused momentum of the fluctuations from the wake as it occurs at Re=1000; (c) close to the wall, downstream the MPP it appears a large wavelength instability that extends towards the separated bubble; (d) no signs of short-wavelength T-S waves are seen within the flow. This might be a consequence of the still low time dependency of the flow and the inherent difficulty in capturing the receptivity and the early evolution of the transitional instabilities. We did not attempted to perform another simulation at 600<Re<1000 to validate the hypothesis of the wave refraction because the separated bubble would become larger and therefore not suitable to be compared to the case at Re=1000.

5.1.1.4. Mesh study. A study of mesh dependence of the results for Re=1000 was performed to assure the appropriate resolution of the length scales. The flow field obtained with a mesh of 784 macro-elements and 25 nodes per element was compared to results computed with a mesh having the same macro-element discretization and 49 nodes per element. The location of the boundary layer separation agreed within 0.5%. The maximum velocity differed in less than 3.2% between the two meshes. Therefore, the coarser mesh used in this work proved to be not only computationally economical but enough accurate to solve the problem.

5.1.1.5. Comparison with experimental data. Figure 13 depicts the comparison between the mean flow pressure coefficient C_p obtained numerically for Re=1000 and the experimental data measured at $Re=5.9x10^5$ (Dring et al., 1988). The qualitative behavior of the C_p computed for the basic flow at Re=1000 and the C_p experimentally measured at the much higher Re is similar. There is good agreement for the leading edge flow overspeed, the location of the MPP over the suction side and the smooth acceleration from the leading edge to the trailing edge over the pressure side. The pressure gradient on the suction side is steeper in the experimental results downstream of the leading edge. The difference between the experimental data and the simulations is approximately 10% of the total FPG. Dring et. al. (1988) concluded from their experiments that there was no boundary layer separation based on the mild APG, representing a smooth deceleration from the MPP to the trailing edge over the airfoil suction side. However, here we reproduced a similar qualitative pressure gradient and found a clear region of separation covering 30% of the axial chord from a location downstream the MPP to the trailing edge. This disagreement may be explained by either the large difference in Re between the experiments and the simulations or by the absence of direct visualization during the experiments. The satisfactory correspondence of non-dimensionalized pressure gradients between low Re numerical predictions and high Re experiments is encouraging. This agreement anticipates the relevance of DNS results for low Re in the investigation of

fundamental aspects of the excitation and evolution of transitional instabilities affected by complex pressure fields.

5.1.2. Perturbed Flow. Perturbed flow simulations were performed by superposing an artificial disturbance onto the basic flow. These disturbances were superposed to the basic flow inlet boundary condition and as time-harmonic oscillations with frequencies and amplitudes in the ranges $8.8 \leq \omega_d \leq 1099.5$ and $0.005 \leq \varepsilon \leq 0.02$, respectively.

5.1.2.1. Perturbation field. The time-harmonic oscillations superposed onto the basic flow act as a generator of Stokes waves. These waves travel downstream the blade leading edge and are particularly intense within the viscous layer. The Stokes wave, solution for a double infinite wall oscillating parallel to itself in a medium at rest (Goldstein & Hultgren, 1987, 1989), is the equivalent solution to the problem with the oscillating stream and the stationary walls. The Stokes waves have an associated longitudinal pressure fluctuations and, therefore, may also be recognized as acoustic waves (Wlezien, 1995) with its typically infinite wavelength. Figure 14 depicts the speed Sp and pressure fields associated to the pure Stokes wave, generated from a perturbation with $\omega_d=26.4$ and $\varepsilon=0.02$, traveling within the cascade geometry at four times within its fundamental period of oscillation. The pressure field oscillations, in phase everywhere and with a larger amplitude than the encountered in the basic flow pressure fluctuations, confirms the acoustic-type nature of the time-harmonic perturbation. The velocity field though, shows a non-uniform phase distribution with moderate amplitudes compared to those in the basic flows. It is seen how the maximum intensity of the perturbation is reached close to the airfoil wall and in a bridge built between the trailing edge and the MPP of the upper and lower airfoils, respectively. This result indicates that the pressure field associated to the flow within the cascade geometry is naturally given to promote the interaction between the upper airfoil trailing edge and the lower airfoil suction wall.

Since the results for the perturbed flows show a clear distinction between the basic steady state regime (subcritical) and the basic self-sustained fluctuating regime (supercritical), we present the analysis in one subsection for each case.

5.1.2.2. Subcritical flow regimes. The subcritical basic flow (Re=231) responds to the superposed perturbation in two ways; if ω_d is chosen to be far from the natural frequency of fluctuation of the supercritical basic flow ω_{2D_1000}, the basic flow behaves indifferently, while if ω_d is chosen to be close to ω_{2D_1000}, short wavelength instabilities are excited within the suction-side boundary layer downstream the MPP, becoming specially intense just downstream the trailing edge within the wake. Since the perturbation has a quasi-infinite wavelength, the residual effects left on the basic flow by the action of the perturbation are captured by plotting the speed Sp' at the moment when the superposed perturbation vanishes. These results are shown in Fig. 15 for the perturbed flow at Re=231 with ε=0.02 and (a) ω_d=88.0; and (b) ω_d=26.4. The fluctuating speed field Sp' shows that, for ω_d=26.4, vortical instabilities are excited downstream the MPP above the airfoil suction side. These instabilities propagate in the streamwise direction reaching their largest intensity within the wake. The excited instabilities fluctuate with the forcing frequency, as demonstrated from the Fourier spectra in Fig. 16a, and with a reduced wavelength compared to the forcing acoustic-type wave (see Fig. 15). To certify the T-S-type nature of the excited wave, we attempt to visualize the wavelength modulation, characteristic during the generation of T-S waves. Figure 16b depicts the plot of the fluctuating speed Sp' at Re=231 along lines quasi-parallel to the airfoil suction-side wall with ω_d=26.4 and ω_d=88.0. Although it was certainly difficult to totally wipe the Stokes wave off, it is clear from the figure the formation of short wavelength instabilities just downstream the MPP when the perturbation frequency approximately matched the natural frequency ω_{2D_1000} (case with ω_d=26.4). The mismatching of the natural frequency (case with ω_d=26.4) apparently does not cause major changes within the basic flow. From Fig. 16 it is also demonstrated

the important role of the APG which hastens the generation and evolution of the boundary layer T-S waves for the case with ω_d=26.4. Within the boundary layer, the amplitude of the T-S wave reaches its maximum very close to the wall and becomes almost uniform far apart from the wall. Close to the wake, the excited T-S wave amplitude experiences a rapid growth which is largely noticed farther from the wall in concordance with the fact that shed-like instabilities are developing downstream the trailing edge.

5.1.2.3. Supercritical flow regimes. Results for supercritical regimes proved that perturbations with frequencies far from ω_{2D_1000} did not affect either existent T-S waves or the intensity of the vortical structures being shed within the wake. Forcing frequencies close to ω_{2D_1000} did enhance the amplitude of existent T-S waves and the instabilities within the wake. Figures 17a and 17b show the power spectra of the x-velocity component at location P1 (see Fig. 1 for location) for Re=1000 and ε=0.02 with ω_d=88.0 and ω_d=26.4, respectively. In the first case (ω_d=88.0), both ω_{2D_1000} and ω_d appear as two independent superposed modes. In the second case (ω_d=26.4), ω_d is close to ω_{2D_1000}, and a strong coupling between forcing mode and natural mode occurs with a resultant power greater than the sum of the contributions of each mode.

A global visualization of the boundary layer receptivity and stability is depicted in Fig. 18 with a carpet plot of the fluctuating speed Sp' for Re=1000 at the moment when the forced perturbation vanishes for (a) the entire domain, and (b) the airfoil suction-side boundary layer. The plots contrast the appearance of the Sp' field within the basic flow and for the two perturbed cases referred above. The clear enhancement in the T-S waves and vortex shedding is noticed for the case with ω_d=26.4, while the instability amplitude is not affected by the perturbation with ω_d=88.0. The flow behavior for the case with ω_d=26.4 demonstrates the non-linear interaction between the perturbation and the natural instabilities giving rise to a resonance phenomenon that enhances the amplitude of the existent T-S waves and wake instabilities.

5.1.2.4. Receptivity measurement. To quantify both the excitation of T-S waves and their resonant interaction with the superposed disturbance, the effect of amplitude and frequency of the superposed disturbance caused on the intensity of the boundary layer receptivity is quantified. The receptivity is locally evaluated as a proportional measure of the change in amplitude of existent T-S waves, or of the amplitude of excited T-S waves. The receptivity is investigated as a function of Re, ω_d and ε. We compute the receptivity by measuring the time-averaged amplitude of the speed fluctuations, Sp'_{amp} , at a selected location. Sp'_{amp} is defined in two different ways depending on whether the unperturbed basic flow is steady or not. For steady basic or unperturbed flows (Re<375), Sp'_{amp} is defined as the time-averaged amplitude of Sp' in the perturbed flow. For self-sustained fluctuating basic flows (Re>400), Sp'_{amp} is the difference between the time-averaged perturbed Sp' and the time-averaged unperturbed Sp', i.e., the gain in amplitude of the basic flow instability.

Figures 19a, 19b, 19c depict the results at P1 (see Fig.1 for location) at Re=231, 400 and 1000, respectively. For $\omega_d \geq 88.0$, Sp'_{amp} is described by a plateau proportional to the amplitude of the superposed disturbance ε. This linear behavior is independent on Re and is a consequence of the absence of interaction between the T-S waves that might exist within the basic flow and the superposed disturbance. The above mentioned plateau only reflects the amplitude of the superposed Stokes wave placed onto the basic flow. In this case, the Stokes wave sweeps the airfoil passage and its only effect is the contribution to the time-dependency of the flow. Therefore, the Stokes wave neither excites subcritical flow instabilities nor enhances the supercritical flow T-S waves for frequencies far larger than ω_{2D_1000}. When the perturbation frequencies are close to ω_{2D_1000} (ω_d=26.4), a steep increase in Sp'_{amp} occurs. The difference between this amplitude and the amplitude obtained for $\omega_d \geq 88.0$ represents a non-linear enhancement of the amplitude of the existent T-S waves or the amplitude of subcritical T-S waves triggered by the interaction between the Stokes wave and

the boundary layer. The behavior encountered for $\omega_d \approx \omega_{2D\_1000}$ obeys to the time-scale matching between the superposed Stokes waves and the T-S waves. Therefore, it occurs not only a superposition of the Stokes wave onto the basic flow, but also a non-linear interaction between the Stokes wave and the boundary layer with intensity that depends on Re. The enhancement is markedly higher for the resonance cases (Re ≥ 400) than for the cases in which the effect is the excitation of T-S waves (Re=231). The resonance at the current location causes the amplitude of the instability to increase more than 100% above what it would grow just by adding the amplitude of the superposed Stokes wave in that location.

For $\omega_d < 26.4$, although described with limited data, Sp'_{amp} shows a trend to recover the plateau appearance observed for $\omega_d \geq 88.0$, though less steep for Re≤400.

5.2. Fluctuating Kinetic Energy Budget

The next sub-sections describe the numerical results pertaining to the FKE budget. We include results based on the mean flow vorticity, viscous shear stress (named shear stress from hereafter), Reynolds shear stress and the fluctuating kinetic energy itself to help in the interpretation of the FKE budget. Figure 20 depicts the airfoil with locations along the suction side and normal direction to the wall at different positions downstream the leading edge, as they will be referred to in the figures.

5.2.1. Basic Flow.

The FKE budget analysis is presented in this sub-section for a supercritical basic flow at Re=1000. The objective is to explain the boundary layer receptivity and stability characteristics within self-sustained oscillatory basic flows.

5.2.1.1. Mean flow characteristics. Figures 21a through 21h show the plots of the tangential velocity, vorticity, shear stress, Reynolds shear stress and fluctuating kinetic energy at different perpendicular locations along the suction-side boundary layer under favorable pressure gradient (FPG) and adverse pressure gradient (APG). The regions under FPG and APG are separated in the

figures by the minimum pressure point (MPP). The section of the boundary layer under FPG is characterized by the largest vorticity production and shear stress on the wall although these two parameters diminish steeply approaching the boundary layer outer region. The section of the airfoil under APG is characterized for presenting an inflection point in the velocity profile at every transversal station. Since the flow close to the airfoil wall has a large component parallel to it, the vorticity (ω_z) and shear stress (τ_{xy}) are generated at the wall and maximized around the inflection point. The inflection point plays a primary role in the degree of enhancement suffered by the flow instabilities when the flow is perturbed as we will show later. The time-averaged kinetic energy of the fluctuations $\overline{q'}$ rapidly increases as the flow convects from the leading edge towards the trailing edge. Under APG as expected, is enhanced faster and preferentially towards the boundary layer outer edge as a consequence of the interaction with the wake instabilities (see also Fig. 11). The intensity of the Reynolds stresses $\overline{u_t' u_n'}$ is similarly enhanced towards the trailing edge, though under APG its distribution alternates from positive and moderate close to the wall, as predicted by Lin (1955), to negative and large towards the outer edge of the boundary layer.

5.2.1.2. Time-average equilibrium of the flow. The calculation of the FKE terms T2-T6 is accomplished within the entire domain. However some scatter in the pressure term (T3) product of the large gradients and the discontinuity in the derivatives across the boundary of contiguous elements suggested us to calculate the pressure term as the balance of the FKE. However, for this calculation to be accurate, it requires that T1 be negligible. Figure 22 shows (a) T3 directly computed from the fluctuating velocity and pressure fields; and (b) T3 obtained from the balance of the FKE equation, neglecting T1. In the comparison, T3 is shown within the airfoil suction-side boundary layer. The comparison shows that T3 obtained from the balance of the FKE equation, while smoothing out the scatter in the computed T3, reproduces accurately the main features of the

computed term. Neglecting T1 is consistent with the fact that although we are considering unsteady flows, in time-average, the flow is steady and in equilibrium without localized gain or loss of FKE. From now on, the T3 shown in the FKE budgets is the calculated to balance the equation, while T1 is assumed to be zero everywhere.

5.2.1.3. FKE budgets. Figure 23 shows the FKE budget for Re=1000 in five different stations: beyond the leading edge (L_3), downstream the minimum pressure point -MPP- (L_5), at the separation point (L_6), in the middle of the separated bubble (L_7) and close to the trailing edge (L_8). The FKE budgets are presented as a function of the normal distance to the wall d_n, non-dimensionalized by the local boundary layer thickness δ. At the entrance (L_3), moderate dissipation of energy T6 over the wall is accompanied by a favorable fluctuating pressure term T3 which provides the FKE uniformly across the the section to sustain the convection T2 of the long wavelength instability generated at the leading edge. The production term T4, as expected under FPG, is almost negligible within the lower half of the boundary layer, while negative within the upper half. A negative T4 indicates that the mean flow withdraws energy from the instability and promotes its stabilization. Between the MPP and the separation point (SP) at L_5, the FKE budget describes the energy transport during the wavelength modulation process that gives rise to the receptivity phenomenon, i.e., the generation of T-S waves. While the fluctuating pressure field T3 offers resistance to the convection of the instability within the lower half of the boundary layer, the production is intensive around the inflection point and assists the wavelength modulation. The largest production of FKE around the inflection point reflects the highest level of shear stress and vorticity we observed around the inflection point in the mean flow (see Fig. 21e). Since the shear stress and the vorticity are measures of the level of deformation and rotational velocity of the fluid particles, respectively, it is expected that the largest deformation of the mean flow causes the largest amount of work against the fluctuating shear stresses, i.e., T4. Within the boundary layer upper half, the

production becomes negligible and the fluctuating pressure, T3, becomes the driving force that sustain the instability convection along with the mean flow, T2. The distribution of the Reynolds stresses across the station, shown in Fig. 24., confirms that the largest momentum exchange of the fluid fluctuation in the tangential and normal direction $\overline{u_t' u_n'}$ occurs towards the outer edge of the boundary layer.

To further the study of the receptivity using the FKE terms, we plot the distribution of T2, T3 and T4 over the area where the wavelength modulation occurs. Figures 25a, 25b and 25c depict the distribution of T2, T3 and T4, respectively, within the airfoil suction-side boundary layer between the MPP and the SP. The three figures show characteristic behaviors around the inflection point of the velocity profile, located at about 0.3δ from the wall in the middle of the section between the MPP and the SP. The wavelength modulation is marked by a progressive reduction of the instability convection, T2, reaching a minimum in the middle of the section followed by a progressively recovery towards the SP. The fluctuating pressure field (T3), while contributing moderately to the instability convection within a sub-layer very close to the wall, offers resistance to the instability development around the inflection point and probably is the opposite force that explains the reduction of wave phase speed that forces the refraction of the wave. The production term T4, while intense around the MPP and immediately downstream the SP, is reduced considerably towards the middle of the section between the MPP and the SP. The reduction of the production of FKE during the intermediate phase of the wavelength modulation might result from the instability wavelength contraction that is done against the mean flow and therefore, while in process, requires the transport of FKE to the mean flow.

The characteristics of the T-S wave evolution are understood from the observations at stations L_6, L_7 and L_8. The FKE budgets at stations L_6, L_7 and L_8, show the FKE transport at the SP, the middle of the bubble and further downstream close to the trailing edge, respectively, as shown in Fig. 23. The FKE

budgets at these three stations are qualitatively similar and quantitatively larger for the stations L_7 and L_8 compared to the station L_6. The larger energy transport at L_7 and L_8 obeys to the evolution of T-S waves within the bubble. At all three locations, both ω_z and τ_{xy} are maximum around the IP as seen in Figs. 21f through 21h. Within the lower half of the boundary layer the vorticity increases towards the center, and the unsteady pressure gradient (T3) offers moderate resistance to the FKE transport. The FKE production, T4, within the separated boundary layer shows a diffusive distribution indicating that energy is transferred within the lower half to account for the convection along the mean flow, while energy is released back to the mean flow by about the same proportion within the upper half. Within the upper half of the boundary layer the convection of the instability along with the mean flow (T2) is proportional to the distance from the wall and is promoted by the fluctuating pressure gradient (T3) in the transversal direction. Therefore the propagation of T-S waves within the airfoil boundary layer can be seen as promoted by two agents. Within the boundary layer lower half, the propagation of T-S waves is supported by the work of deformation or restoration of the mean flow under adverse pressure gradient against the fluctuating stresses (T4). Within the upper half, T-S wave propagation is sustained by the pressure fluctuations which assist the wave convection and the transfer of energy to the mean flow.

5.2.2. Subcritical Perturbed Flow. This sub-section extends the FKE budget analysis to subcritical perturbed flows. We consider the energy transport associated to the artificial generation of T-S waves by the coupling of the superposed perturbation and the existent length and time scales within a subcritical regime (Re=231).

In the measure of the receptivity in section 5.1.3 we found that, when the subcritical flow is perturbed with the appropriate frequency, excitation of T-S waves occurred. This is visualized as a global reaction of the flow with the larger intensity observed within the wake and the airfoil suction-side boundary layer. The forcing frequency is chosen to have values that either closely match or

largely mismatch the natural frequency encountered within the basic flow at Re=1000 (ω_{2D_1000}=29.6).

5.2.2.1. Mean flow changes. Figures 26a through 26e show the changes in the mean flow caused on the subcritical flow (Re=231) by the forcing disturbance for ω_d=26.4 and ω_d=88.0. For the two perturbation frequencies selected for the comparison, the variation in the mean velocity (speed, Sp) profiles shows in Figs. 26a and 26b a similar parabolic enhancement within the boundary layer under FPG (represented at L_2 and L_4). Downstream the MPP (at L_5), mean flow changes are almost identical for the two frequencies with differences observed only on the averaged fluctuating kinetic energy $\overline{q'}$ and the Reynolds shear stresses $-\overline{u_t' u_n'}$. These differences mark the initiation of the flow destabilization observed previously in the plots of the fluctuating component of the speed Sp' in Fig. 16b. Further downstream, at L_7, in the middle of the APG region, although the boundary layer remains attached, the fluid flow destabilization is enhanced towards the upper half of the boundary layer. Although the mean speed, vorticity and shear stresses do not experience large changes comparing the two cases, the flow destabilization is markedly related to the generation of flow unsteadiness as indicated by the large $-\overline{u_t' u_n'}$ and $\overline{q'}$ within the boundary layer upper half for the case with ω_d=26.4. Closer to the trailing edge, at L_8, the changes in the mean flow are even more pronounced for the case with ω_d=26.4. The mean speed augments drastically across 60% of the boundary layer thickness compared to the case with ω_d=88.0, while the shear stress and vorticity are enhanced mainly close to the wall and close to the outer edge of the boundary layer. The Reynolds shear stress $-\overline{u_t' u_n'}$ and the averaged FKE $\overline{q'}$ perform again as excellent monitors of the boundary layer destabilization depicting larger intensity for the case with ω_d=26.4.

5.2.2.2. FKE budgets. FKE budgets at stations L_2, L_4, L_5, L_7 and L_8 are presented in Figs. 27a through 27e, respectively. At stations L_2 and L_4 the flow field is under FPG and the superposed perturbation enhances uniformly the transport of

the FKE by the fluctuating pressure above 30% of the boundary layer thickness independently of the perturbation frequency. However, within the lower 30% of the boundary layer thickness the development of a Stokes-like layer is noticed as the intensity of the fluctuating pressure transport of FKE is proportional to the perturbation frequency. This behavior reflects the acoustic nature of the Stokes wave generated at the contact between the superposed disturbance and the airfoil wall. The Stokes layer is noticed also in the next stations, though the intensity becomes negligible as secondary effects related to the flow destabilization appear, as discussed later. The uniform and positive distribution of T3 within the upper region of the boundary layer provides the necessary energy to convect the Stokes wave along with the mean flow (T2). The non-uniform and frequency-dependent T3 within the Stokes layer, sustains the convection of the Stokes waves close to the wall where the viscous demands (T5) are more significant. At station L_5, the boundary layer is under APG and the Stokes layer is still noticeable. Above the Stokes layer, the distributions of T2 and T3 are reversed compared to the precedent stations though, do not show differences between the two cases.

Further downstream under APG, at station L_7, for the case with ω_d=26.4, the boundary layer receptivity is evident. The receptivity occurs as the fluctuating pressure field (T3) offers an enhanced resistance to the evolution of the Stokes wave. This resistance assists the wavelength modulation that is taking place and that gives rise to the generation of the T-S wave, previously observed in Fig. 16b, under a preferential perturbation frequency (ω_d=26.4). The wavelength modulation is supported with FKE supplied by the mean flow convection (T2). Underneath the Stokes layer, the FKE budget does show the non-uniform frequency-related distribution of T3 observed in the previous stations.

At L_8 the roles of T2 and T3 are reversed for both cases (ω_d=88.0 and ω_d=26.4). The T-S waves generated for the case with ω_d=26.4 are convected away (T2) assisted by a favorable and enhanced fluctuating pressure gradient (T3). The FKE energy provided by T3 also supports the work of the fluctuations (T-S

waves) to deform the mean flow (T4) as they become larger while approaching the wake.

5.2.3. Supercritical Perturbed Flow. We now consider the energy exchange when the superposed perturbation interacts with existent T-S waves in a supercritical regime at Re=1000.

In section 5.1.3 we described that, when the supercritical flow is perturbed with the appropriate frequency, resonance in the amplitude of the existent T-S waves occurred. As for subcritical flows, this is visualized as a global reaction of the flow with the larger intensity registered within the wake and the suction-side boundary layer. The forcing frequency is chosen to have values that either closely match or largely mismatch the natural frequency encountered within the basic flow at Re=1000 (ω_{2D_1000}=29.6).

5.2.3.1. Mean flow changes. Figures 28a through 28e show the changes in the boundary layer mean flow field as a consequence of superposing a perturbation with ε=0.02 and, ω_d=26.4 and ω_d=88.0 for Re=1000 at stations L_2, L_4, L_5, L_7 and L_8, respectively. Under FPG, at L_2, Fig. 28a shows the variation in the mean speed profiles with a deficit very similar for both frequencies. The variation of the mean ω_z and τ_{xy} is also independent on the perturbation frequency and confirms that the superposed perturbation, at this station, has not interacted effectively with the boundary layer instabilities. Further into the FPG region, at L_4, Fig. 28b shows small variations in the mean flow field, if we consider the order of magnitude compared to the following stations. However, there is a consistent excess of vorticity and shear stress close to the wall for the case with ω_d=88.0 compared to the case with ω_d=26.4, which might be a consequence of the frequency-related enhancement within the Stokes layer explained in section 5.2.2.2.

Slightly downstream the MPP, at L_5, Fig. 28c shows a substantial bell-type augmentation in the mean speed $\Delta\overline{Sp}$ for the case with ω_d=26.4, while the mean speed does not change for the case with ω_d=88.0. The maximum enhancement of

the mean velocity, noticed for the case with ω_d=26.4, occurs around the inflection point (IP). The bell-type enhancement of the mean speed originates a cross section asymmetric distribution of $\Delta\overline{\omega_z}$ with the largest intensity on the wall accounting for 5% of the mean vorticity on the wall for the basic flow (see Fig. 21e). The asymmetric distribution of $\Delta\overline{\omega_z}$ reflects the added tendency to rotate in the clockwise direction for the fluid under the IP and in the counter-clockwise direction for the fluid above the IP. The intensity of the added vorticity reaches a maximum, although with opposite signs, under and above the IP, and becomes zero at the IP and at the outer limit of the boundary layer. The mean shear stress $\Delta\overline{\tau_{xy}}$ depicts a large enhancement within the lower half of the boundary layer for the case with ω_d=26.4 compared to the case with ω_d=88.0. Although $\Delta\overline{Sp}$, $\Delta\overline{\omega_z}$ and $\Delta\overline{\tau_{xy}}$ depict characteristic enhancements for the case with ω_d=26.4 at station L_5, the Reynolds shear stress and the mean FKE, $-\overline{u_t' u_n'}$ and $\overline{q'}$, respectively, do show enhancements, though of small magnitude, for the case with ω_d=88.0. Therefore, at station L_5, located within the region where the receptivity takes place, the flow destabilization by the preferential frequency is demonstrated in the mean flow distortion but not in the fluctuating-related quantities.

Further downstream, at stations L_7 and L_8, within the separated bubble, the mean flow destabilization is more evident and even the fluctuating-related quantities $-\overline{u_t' u_n'}$ and $\overline{q'}$, are markedly larger for the case with ω_d=26.4 compared to the case with ω_d=88.0. The enhancement observed in the quantities $-\overline{u_t' u_n'}$ and $\overline{q'}$, occurs within the upper half of the boundary layer and is proportional to the distance from the wall. Therefore, although the receptivity is apparently not affected by the disturbance, resonance in the amplitude of existent T-S waves does occur as the result of the interaction between these waves and the induced Stokes waves when the frequency of the superposed perturbation matches approximately the natural frequency of the flow at Re=1000 (ω_{2D_1000}=29.6).

5.2.3.2. FKE budgets. FKE budgets at stations L_2, L_4, L_5 and L_7 are presented in Figs. 29a through 29e, respectively. At stations L_2, L_4 and L_5, the results are in excellent agreement with the FKE budgets from the perturbed subcritical flow, confirming that up to station L_5 the perturbation has just superposed to the basic flow without nonlinear interaction.

In the region of APG, at stations L_7 and L_8, the FKE transport, shown in Figs. 29d and 29e, is remarkably different to what happens to the subcritical flow (Re=231, Figs. 27d and 27e). Within the bubble the FKE budgets reflect the energetic interaction between the T-S waves and the induced Stokes waves according to the perturbation frequency. The case for the larger frequency (ω_d=88.0) not only shows levels of enhancement in the energy transport mechanisms lower than for the case with frequency approximately matching the natural frequency (ω_d=26.4), but a different qualitative distribution. For example, at station L_7 the flow perturbed with ω_d=88.0 depicts negative levels of production (T4) indicating that the fluctuations attributed to the induced Stokes waves and the evolving T-S waves release energy to the mean flow. At the same time, that energy is provided to the waves by a favorable fluctuating pressure gradient, thus balancing the energy transfer. At the same station, the flow perturbed with ω_d=26.4 shows a marked interaction between the Stokes wave and the T-S waves traveling within the bubble, as the FKE production is promoted within the lower half of the boundary layer and inhibited within the upper half. The fluctuating pressure gradient (T3) plays a fundamental role in the convection of the T-S waves within the upper half of the boundary layer. At the station L_8, the FKE budget, depicted in Fig. 29e, is qualitatively similar to the FKE budget computed for the perturbed subcritical regime (Fig. 27e), though more intense for the case with resonance (ω_d=26.4). Thus, the fluctuating pressure gradient (T3) sustains the convection of the enhanced T-S waves along with the mean flow and provides the energy to support the work of the fluctuations (coupled T-S and Stokes waves) to deform the mean flow (T4) as they become larger while approximating the wake.

5.3. Three-dimensional Validations

To endeavor the validation of the results from the two-dimensional analysis, we initiated a preliminary extension of the study to three dimensions. Due to limitations with the computer memory and time we could only perform DNS for flows at Re=400. For this Re, the two-dimensional basic flow has shown a separated boundary layer and weak fluctuations. The three-dimensional validation of the basic flow is based on a comparison between the mean flow fields for the two-dimensional case and the three-dimensional case at the midspan plane. The main features to contrast are the flow streamtraces and the pressure field. The streamtraces allow us to compare the flow direction, the wake spatial waviness and the separated bubble.

We include also an extension for a perturbed case. The three-dimensional basic flow field (Re=400) is perturbed with a two-dimensional time-harmonic disturbance similar to the one used in the two-dimensional study. We compare the amplitude of the existent instabilities within the basic flow and the amplitude of the instabilities in the perturbed flow at the instant when the superposed perturbation vanishes. For the perturbed case, we use the perturbation amplitude and frequency of ε=0.02 and ω_d=26.4, respectively, as this frequency is found to trigger or enhance T-S waves within the two-dimensional flow.

The three-dimensional simulations are performed using a mesh with 630 macro-elements and 5 nodes in each direction per element. This mesh has 5 layers in the spanwise direction and 126 projected elements per layer, i.e., at the midspan, this mesh is about 6 times coarser than the two-dimensional 784-element mesh.

5.3.1. Basic Flow. Figure 30a shows the 630-macro-element three-dimensional mesh and Fig. 30b shows an open view of the mesh with the macro-elements along with the 5 nodes per direction used for the validation of the two-dimensional basic flow at Re=400. Time evolution of the x-velocity at locations close to the separated bubble shows a weak but stable fluctuation with frequency

ω_{3D_400}=13.8. This frequency is in fair agreement with ω_{2D_400}=21.1 obtained from the two-dimensional case. In both cases, the measurement of the frequency is made at a point in the interior of the separated bubble since it registers the largest unsteadiness within the boundary layer.

The streamtraces and the mean pressure field for the three-dimensional simulation at the midspan section and for the two-dimensional simulation are shown in Figs. 31a and 31b, respectively.

The size of the separated bubble for the three-dimensional case is larger than the obtained from the two-dimensional simulation suggesting, at a first inspection, the possible influence of three-dimensional vortices developing a secondary flow in the z-direction. However, the z-component of the velocity at the midspan in the three-dimensional simulation demonstrated (not shown here) to be 4 to 5 orders of magnitude smaller than the x- and y-components. Therefore, despite the marked differences between the two- and three-dimensional results, the last ones point towards the two-dimensionality of the flow field at the midspan and reveal the need of a mesh-dependence study, not performed yet, on the three-dimensional case. Thus, the three-dimensional simulations, at the level of refinement shown in this work, are useful only as a coarse reference for the comparison of the flow field general features between the two- and three-dimensional cases.

Figure 32 shows a carpet plot of the fluctuating component of the speed, Sp', at a characteristic time, over the midspan section of the three-dimensional domain for the basic flow at Re=400. The figure depicts, though with low resolution at the element boundaries, the generation of instabilities around the leading edge and their convection and enhancement within the wake.

5.3.2. Perturbed Flow. Figure 33 shows the carpet plots of Sp' for both the basic flow at a characteristic time and the perturbed flows at the moment when the superposed perturbation vanishes. Both cases correspond to results from the three-dimensional simulation at the midspan for Re=400. The results are plotted at the same scale to show the large enhancement experienced by the flow

instabilities when a perturbation with ε=0.02 and frequency of ω_d=26.4 is superposed on the inlet boundary of the flow domain.

At this moment, no additional three-dimensional simulations have been completed. We believe that the next step should be the three-dimensional mesh refinement study before any conclusion on the validation of the two-dimensional basic and perturbed flows are drawn.

CHAPTER 6

CONCLUDING REMARKS AND FUTURE WORK

Direct Numerical Simulations of airfoil cascade flows are performed for unperturbed and perturbed conditions in the Reynolds number (Re) range of 231-1000. The analysis of the generation and evolution of primary transitional Tollmien-Schlichting (T-S) waves, named the receptivity and stability study of the boundary layer, is addressed from two different though complementary approaches; one is based on the direct computation of the boundary layer flow field dynamics; and the other is based on the evaluation of the Fluctuating Kinetic Energy (FKE) transport throughout the entire flow domain. Our work extents from the study of the unsteady separated boundary layer within basic flows to the study of non-separated and separated boundary layers within perturbed flows.

The conclusions from each of the approaches above mentioned are presented in the following two subsections.

6.1. Flow Field Dynamics

The basic flow bifurcates from steady to self-sustained fluctuating at a critical Re between 375 and 400. The source of the fluctuations is found in the temporally- and spatially-evolving instabilities generated with a characteristic long wavelength at the airfoil leading edge. These instabilities are largely promoted under adverse pressure gradient within the suction-side boundary layer.

On the airfoil suction-side, the boundary layer separates downstream of the minimum pressure point for Re>400. The boundary layer separation triggers the long to short wavelength modulation of the oncoming wave that ends in the generation of a primary transitional instability or T-S wave. The process of wavelength modulation starts downstream of the minimum pressure point and

ends at the separation point in excellent agreement with previous experimental and theoretical works.

The pressure gradient plays an important role in the evolution of both the leading edge long-wavelength instability and the T-S wave. The adverse pressure gradient turns the amplitude growth of the leading edge instability from slow and linear to fast and exponential. This trend is interrupted by the wavelength modulation process with a gradual decrease in the instability amplitude until the modulation is terminated at the separation point. Thereafter, an even steeper growth of the just-generated T-S wave amplitude occurs, but promptly bounded and attenuated by a stabilizing viscous action of the rapidly thickening boundary layer. The streamwise evolution of the instability wave is accompanied with diffusion via momentum exchange, transmitting the fluctuating modes throughout the entire domain. Regions close to the wavelength modulation region, although outside the boundary layer, are largely affected by the transitional fluctuations and, therefore, provide an ideal location for punctual measurements of the boundary layer receptivity.

The possibility of inducing T-S waves within subcritical boundary layer flows is demonstrated by perturbing otherwise steady flows with time-harmonic disturbances approximately matching the natural frequency of fluctuation found in the supercritical flow. The disturbance at the contact with the airfoil turns into a Stokes wave which sweeps the flow with an infinite wavelength and triggers T-S waves within the boundary layer. The generated T-S waves exhibit the same frequency as the forcing disturbance and depict the typically short wavelength.

For supercritical flows, resonant effects on the amplitude of existent transitional waves arise when the forcing frequency matches the frequency of fluctuation of these waves, also named the natural frequency of the flow. The receptivity is quantified locally by computing the amplitude enhancement of the speed fluctuating component as a function of the disturbance amplitude, frequency and Re. In all perturbed flow simulations with disturbance frequency

far from the flow natural frequency, the induced Stokes wave just superposes on the basic flow without apparent interaction.

The flow field obtained numerically at Re=1000 exhibits some features of the flow observed in experiments at much higher Re. For example, the computed results reproduce the leading edge overspeed region, location of the minimum pressure point, pressure gradient and smooth acceleration on the airfoil pressure side as well as the location of the region where natural transition begins. However, there are differences in the prediction of separation and severeness of the pressure load on the airfoil suction side. The results indicate the potential benefits DNS may provide as a complementary tool in the investigation of the generation and evolution of T-S waves under the effect of free stream disturbances in high Re engineering flows.

6.2. FKE Transport

The mechanisms of energy exchange and transformation between the mean flow and the fluctuations in the Fluctuating Kinetic Energy (FKE) equation are computed for basic and perturbed flows. Particular attention is given to the analysis of the FKE budgets within the airfoil suction-side boundary layer to explain the receptivity phenomenon and the stability characteristics.

For unsteady basic flows at Re=1000, the initiation of the instability wavelength modulation process, marked by the minimum pressure point, is accompanied by the production of FKE predominantly around the mean velocity inflection point. Above and underneath the inflection point, the production decays gradually towards the boundary layer edges. The production of FKE mainly accounts for the energy demanded to convect the instability against an adverse fluctuating pressure gradient while the wavelength contraction is taking place. Above the inflection point, the fluctuating pressure gradient favors the convection of instabilities out of the boundary layer. The evolution of T-S waves within the separated bubble is characterized by a transverse asymmetric production of FKE; positive within the lower half of the boundary layer and negative within the upper half. The positive production reaches its maximum

around the inflection point. Within the upper half of the boundary layer, the T-S wave convection is intensified by the action of the fluctuating pressure field.

For perturbed flows, the time-harmonic disturbance superposed to the originally basic flow has a well defined global incidence on the energy transport characteristics. Within the favorable pressure gradient region, the superposed disturbance generates a sublayer, within the lower half of the boundary layer thickness, very close to the wall. Within the sublayer, the unsteady pressure field favors the convection of both the generated Stokes wave and the leading edge-associated long wavelength instability. The sustaining role of the unsteady pressure within the sublayer is proportional to the disturbance frequency. Above the sublayer, the unsteady pressure contributes FKE with less but uniform intensity to support mainly the instability convection. The uniform distribution above the sublayer does not depict dependency on the disturbance frequency. Further downstream, under adverse pressure gradient, the role of the sublayer becomes less important. In the study of the effects of the forced disturbance on the boundary layer receptivity and stability, we explain separately the perturbed flow behavior for otherwise steady flow regimes (Re=231) and for self-fluctuating flow regimes (Re=1000).

For Re=231, under adverse pressure gradient region, the boundary layer is essentially indifferent to the perturbations within its lower half. However, within the upper half, T-S waves are generated for the case with perturbation matching the natural frequency. The T-S wave generation, i.e., the boundary layer receptivity phenomenon, is characterized by the retarding action of an adverse unsteady pressure field assisting the wavelength modulation of the Stokes wave. Once the T-S wave is generated, its convection is strongly promoted by a favorable unsteady pressure field close to the wake.

For Re=1000, the receptivity that gives rise to the naturally-generated T-S waves is unaffected by the disturbances. However, the stability of the boundary layer, i.e., the evolution of existent T-S waves, is singularly affected. For the flow perturbed with a disturbance matching the natural frequency, the resonance

found in the flow field visualization is also illustrated by the FKE budget. In such a case, it is noticed an enhancement in the production of FKE within the boundary layer lower half and a large amount of FKE supplied by the unsteady pressure field to assist the T-S wave convection within the upper half.

6.3. Future Work

Results from the preliminary three-dimensional validation of the two-dimensional results have shown the need of a mesh refinement study. We recommend the extension of the three-dimensional simulations in accordance to the following path: (a) perform DNS study for flows at Re=400 with finer meshes until results demonstrate negligible variations respect to the mesh resolution. The flow field obtained from the refined mesh at the midspan will provide a reliable source of information to validate the two-dimensional simulations at the same Re; (b) perform DNS study for selected cases at Re=1000 to validate the more complex and well-defined T-S waves observed in the two-dimensional simulations and their interaction with the essentially two-dimensional forced perturbation. The three-dimensional study at Re=1000 will require, as usual, a mesh refinement study before conclusions on the validity of the two-dimensional simulations at the same Re are drawn.

We consider that a useful extension of this work could be the local measurement of the local receptivity and resonance effects using the terms of the FKE equation in addition to the time-averaged amplitude of the instability (shown in Fig. 19). The FKE terms would provide a naturally time-averaged measure of the receptivity and stability effects and are calculated throughout the entire discretized mesh with a minimum extra effort. We think that this could be an excellent oportunity to perform a study of the sensitivity to small variations of the perturbation frequency around the natural frequency. The sensitivity study will help to clarify the origin of the dip observed in the amplitude of the fluctuations, seen in Fig. 19, for Re=400 and Re=1000 when the superposed perturbation has a frequency slightly larger than the natural frequency and amplitude of $0.02U_\infty$.

The calculation of the forces acting on the airfoil surface, the friction coefficient and the heat transfer characteristics are of major concern in the engineering field and could be obtained as an extension from the present work.

We also suggest the extension of our investigation by including more complex forms of free stream disturbances.

REFERENCES

Amon, C.H., 1993, "Spectral Element-Fourier Method for Transitional Flows in Complex Geometries," *AIAA Journal*, Vol. 31, No. 1, pp. 42-48.

Amon, C.H. and Patera, A.T., 1989, "Numerical Calculation of Stable Three-Dimensional Tertiary States in Grooved-Channel Flow," *Physics of Fluids A*, Vol. 1 (12), pp. 2005-2011.

Bailey, D.A., 1980, "Study of Mean- and Turbulent-Velocity Fields in a Large-Scale Turbine-Vane Passage," *Journal of Engineering for Power*, Vol. 102, pp. 88-95, 1980.

Baskharone, E.A. and McArthur, D.R., 1990, "A Comprehensive Analysis of the Viscous Incompressible Flow in Quasi-Three-Dimensional Airfoil Cascades," *International Journal for Numerical Methods in Fluids*, Vol. 11, pp. 227-245.

Betchov, R. and Criminale, Jr., W.O., 1967, "Stability of Parallel Flows," Academic Press, USA.

Breuer, K.S., 1989, "The Evolution of a Localized Disturbance in a Laminar Boundary Layer," *Laminar-Turbulent Transition, IUTAM Symposium*, D. Arnal, and R. Michel, eds., Springer-Verlag, Berlin, pp. 189-198.

Buter, T.A. and Reed, H.L., 1991, "Leading-Edge Receptivity to a Vortical Free-Stream Disturbance: A Numerical Analysis," Instability, Transition, and Turbulence, M.Y. Hussaini, A. Kumar, and C.L. Streett, eds., Springer-Verlag, New York, pp. 452-469.

Canuto, C., Hussaini, M.Y., Quarteroni, A. and Zang, T.A., "Spectral Methods in Fluid Dynamics," Springer-Verlag, USA.

Chiu, W.K. and Norton, M.P., 1990, "The Receptivity of Laminar Boundary Layer Flow to Leading Edge Vibrations," *Journal of Sound and Vibration*, Vol. 141, pp. 143-164.

Crouch, J.D., 1991, "Nonlocalized Receptivity to Vortical Free-Stream Disturbances," Instability, Transition, and Turbulence, M.Y. Hussaini, A. Kumar, and C.L. Streett, eds., Springer-Verlag, New York, pp. 470-480.

Danabasoglu, G.D. and Biringen, S., 1991, "A Spectral Multi-Domain Code for the Navier-Stokes Equations," Instability, Transition, and Turbulence, M.Y. Hussaini, A. Kumar, and C.L. Streett, eds., Springer-Verlag, New York, pp. 283-293.

Deane, A.E. and Mavriplis, C., 1991, "Low-Dimensional Description of the Dynamics in Separated Flow Past Thick Airfoils," *AIAA 2nd Fluid Dynamics, Plasma & Lasers Conference*, Hawaii.

Deconinck, H. and Hirsh, C., 1981, "Finite Element Methods for Transonic Blade-to Blade Calculation in Turbomachines," *Journal of Engineering for Power*, Vol. 103, pp. 665-677.

Dovgal, A.V. and Kozlov, V.V., 1989, "Hydrodynamic Instability and Receptivity of Small Scale Separation Regions," *Laminar-Turbulent Transition, IUTAM Symposium*, D. Arnal, and R. Michel, eds., Springer-Verlag, Berlin, pp. 523-531.

Dovgal, A.V., Kozlov, V.V. and Simonov, O.A., 1986, "Experiments on Hydrodynamic Instability of Boundary Layers with Separation," *Boundary-Layer Separation, IUTAM Symposium*, F. T. Smith, and S. N. Brown, eds., Springer-Verlag, Berlin, pp. 109-130.

Drazin, P.G. and Reid, W.H., 1991, "Hydrodynamic Stability," Cambridge University Press, USA.

Dring, R.P., Blair, M.F., Joslyn, H.D., Power, G.D. and Verdon, J.M., 1988, "The Effects of Inlet Turbulence and Rotor/Stator Interactions on the Aerodynamics and Heat Transfer of a Large-Scale Rotating Turbine Model, I-Final Report," NASA Contractor Report 4079.

Dring, R.P., Joslyn, H.D., Hardin, L.W. and Wagner, J.H., 1982, "Turbine Rotor-Stator Interaction," *Journal of Engineering for Power*, Vol. 104, pp. 729-742.

Dunham, J., 1972, "Predictions of Boundary Layer Transition on Turbomachinery Blades," *AGARD*, AG-164, pp. 55-71.

Fasel, H., 1976, "Investigation of the Stability of Boundary Layers by a Finite-Difference Model of the Navier-Stokes Equations," *Journal of Fluid Mechanics*, Vol. 78, part 2, pp. 355-383.

Fasel, H., 1989, "Numerical Simulation of Instability and Transition in Boundary Layer Flows," *Laminar-Turbulent Transition, IUTAM Symposium*, D. Arnal, and R. Michel, eds., Springer-Verlag, Berlin, pp. 587-598.

Fasel, H. and Konzelmann, U., 1990, “Non-Parallel Stability of a Flat Plate Boundary Layer Using the Complete Navier-Stokes Equations,” *Journal of Fluid Mechanics*, Vol. 221, pp. 311-347.

Fischer, P., 1989, "Spectral Element Solution of the Navier-Stokes Equations on High Performance Distributed-Memory Parallel Processors," PhD. Thesis, Massachusetts Institute of Technology.

Fortin, A., Fortin, M. and Gervais, J.J., 1987, "A Numerical Simulation of the Transition to Turbulence in a Two-Dimensional Flow," *Journal of Computational Physics*, Vol. 70, pp. 295-310.

Gaster, M., 1969, “The Structure and Behavior of Laminar Separation Bubbles,” *ARC R&M 3595*.

Gatski, T.B. and Grosch, C.E., 1985, “Numerical Experiments on Boundary Layer Receptivity,” Stability of Time Dependent and Spatially Varying Flows, D.L. Dwoyer and M.Y. Hussaini, eds., Springer-Verlag , New York, pp. 82-96.

Gear, C.W., 1971, "*Numerical Initial Value Problems in Ordinary Differential Equations,*" Prentice-Hall Inc., Englewood Cliffs, New Jersey.

Gedney, C.J., 1983, "The Cancellation of a Sound-Excited Tollmien-Schlichting Wave with Plate Vibration," *Physics of Fluids*, Vol. 26, pp. 1158-1160.

Goel, P. and Amano R.S., 1986, “Turbulence Energy and Diffusion Transport in a Separating and Reattaching Flow,” *AIAA* 86-1724.

Goldstein, M.E., 1985a, "Scattering of Acoustic Waves into Tollmien-Schlichting Waves by Small Streamwise Variations in Surface Geometry," *Journal of Fluid Mechanics*, Vol. 154, pp. 509-529.

Goldstein, M.E., 1985b, "The Generation of Tollmien-Schlichting Waves by Long Wavelength Free-Stream Disturbances," Stability of Time Dependent and Spatially Varying Flows, D.L. Dwoyer and M.Y. Hussaini, eds., Springer-Verlag, New York, pp. 58-81.

Goldstein, M.E. and Hultgren, L.S., 1987, "A Note on the Generation of Tollmien-Schlichting Waves by a Sudden Surface-Curvature Change," *Journal of Fluid Mechanics*, Vol. 181, pp. 519-525.

Goldstein, M.E. and Hultgren, L.S., 1989, "Boundary-Layer Receptivity to Long-Wave Free-Stream Disturbances," *Annual Review of Fluid Mechanics*, Vol. 21, pp. 137-166.

Gottlieb, D. and Orszag, S.A., 1977, “Numerical Analysis of Spectral Methods. Theory and Applications,” Vol. 26, CBMS-NSF Monograph SIAM, Philadelphia.

Grek, H.R., Kozlov, V.V. and Ramazanov, M.P., 1990, "Receptivity and Stability of the Boundary Layer at a High Turbulence Level," *Laminar-Turbulent Transition, IUTAM Symposium*, D. Arnal, and R. Michel, eds., Springer-Verlag, Berlin, pp. 511-519.

Gunzburger, M.D., “Finite Element Methods for Viscous Incompressible Flows,” Academic Press, Inc., USA.

Hammerton, P.W. and Kerschen, E.J., 1991, "Effect of Nose Bluntness on Leading-Edge Receptivity," Instability, Transition, and Turbulence, M.Y. Hussaini, A. Kumar, and C.L. Streett, eds., Springer-Verlag, New York, pp. 441-451.

Heinrich, R.A., Choudhari, M. and Kerschen, E.J., 1988, "A Comparison of Boundary Layer Receptivity Mechanisms," *AIAA*, paper 88-3758-CP.

Herbert, T., 1988, “Secondary Instability of Boundary Layers,” *Ann. Rev. Fluid Mechanics*, Vol. 20, pp. 487-526.

Hinze, J.O., 1987, "Turbulence," McGraw-Hill Publishing Company, 2nd ed., New York.

Hirota, M., Yokosawa, H. and Fujita, H., 1992, “Turbulence Kinetic Energy in Turbulent Flows through Square Ducts with Rib-Roughened Walls,” *Int. J. Heat Transf. Fluid Flow*, Vol. 13, No. 1, pp. 22-29.

Humphrey, J.A.C. and Whitelaw, J.H., 1980, “Turbulent Flow in a Duct with Roughness,” *Turbulent Shear Flows*, II J.S. Bradbury et al., eds., Springer-Verlag, Berlin, 174.

Kachanov, Y.S., Kozlov, V.V. and Levchenko, V.Y., 1979, "Occurrence of Tollmien-Schlichting Waves in the Boundary Layer Under the Effect of External Perturbations," *Transl. Fluid Dynamics*, Vol. 109, pp. 704-711.

Kachanov, Y.S., Kozlov, V.V. and Levchenko, V.Y., 1982, "Initiation of Turbulence in Boundary Layers," Nauka Publ. Siberian Div., Novosibirsk.

Kasagi, N., Tomita, Y. and Kuroda, A., 1992, "Direct Numerical Simulation of Passive Scalar Field in a Turbulent Channel Flow," *ASME J. Heat Transf.*, Vol. 114, pp. 598-606.

Kerschen, E.J., Choudhari, M. and Heinrich, R.A., 1990, "Generation of Boundary Layer Instability Waves by Acoustic and Vortical Free-Stream Disturbances," *Laminar and Turbulent Transition, IUTAM Symposium*, D. Arnal, R. Michel, eds., Springer-Verlag , Berlin, pp. 477-488.

Kim, J., 1988, "Investigation of Heat and Mass Transport in Turbulent Flows via Numerical Simulation," *Transport Phenomena in Turbulent Flows: Theory, Experiment and Numerical Simulation*, M. Hirata and N. Kasagi, eds., Hemisphere Publishing Corp., Washington DC, pp. 157-170.

Kloker, M., 1989, "Numerical Simulation of Two- and Three-Dimensional Instability Waves in Two-Dimensional Boundary Layers with Streamwise Pressure Gradient," *Laminar-Turbulent Transition, IUTAM Symposium*, D. Arnal, and R. Michel, eds., Springer-Verlag, Berlin, pp. 681-686.

Kloker, M., Konzelmann, U. and Fasel, H., 1993, "Outflow Boundary Conditions for Spatial Navier-Stokes Simulations of Transition Boundary Layers," *AIAA Journal*, Vol. 31, No. 4, pp. 620-628.

Korczak, K.Z. and Patera, A.T., 1986, "An Isoparametric Spectral Element Method for Solution of the Navier-Stokes Equations in Complex Geometry," *Journal of Computational Physics*, Vol. 62, pp.361-382.

Kozlov, V.V. and Ryzhov, O.S., 1990, "Receptivity of Boundary Layers: Asymptotic Theory and Experiment," *Proceedings of the Royal Society of London*, Vol. 429, pp. 341-373.

Leehey, P., and Shapiro, P., 1980, "Leading Edge Effect in Laminar Boundary Layer Excitation by Sound," *Laminar-Turbulent Transition, IUTAM Symposium*, R. Eppler, and H. Fasel, eds., Springer-Verlag, Berlin, pp. 321-331.

Leslie, D.C., 1983, "Developments in the Theory of Turbulence," Oxford University Press, USA.

Lin, C.C., 1955, "The Theory of Hydrodynamic Stability," Cambridge University Press, New York.

Lin, N., Reed, H.L. and Saric, W.S., 1991, "Effect of Leading-Edge Geometry on Boundary-Layer Receptivity to Free-Stream Sound," Instability, Transition, and Turbulence, M.Y. Hussaini, A. Kumar, and C.L. Streett, eds., Springer-Verlag, New York, pp. 421-440.

Loehrke, R.I., Morkovin, M.V. and Fejer, A.A., 1975, "Review: Transition in Nonreversing Oscillating Boundary Layers," *Journal of Fluids Engineering*, pp. 534-549, December.

Lugt, H.J., 1983, "Vortex Flow in Nature and Technology," John Wiley & Sons, Inc., 1st english ed., USA.

Lyons, S.L. and Hanratty, T.J., 1991, "Direct Numerical Simulation of Passive Heat Transfer in a Turbulent Channel Flow," *Int. J. Heat Mass Transf.*, Vol. 34, pp. 1149-1161.

Madavan, N., Kelaita, P. and Gavali, S., 1990, "Supercomputer Applications in Gas Turbine Flowfield Simulation," *The International Journal of Supercomputer Applications*, Vol. 4, No.2, pp. 81-95.

Majumdar, D., 1993, "Fluid Flow and Heat Transfer Mechanisms of Self-Sustained Oscillations in Communicating Channels," Ph.D. Thesis, Carnegie Mellon University.

Majumdar, D. and Amon, C.H., 1997, "Oscillatory Momentum Transport Mechanisms in Transitional Complex Geometry Flows," *Journal of Fluids Engineering*, Vol. 119, pp. 1-7.

Mayle, R.E., 1991, "The Role of Laminar-Turbulent Transition in Gas Turbine Engines," *Journal of Turbomachinery*, Vol. 113, pp. 509-537.

Morkovin, M.V., 1969, "Critical Evaluation of Transition from Laminar to Turbulent Shear Layer with Emphasis on Hypersonically Traveling Bodies," Air Force Flight Dyn. Lab. Rep. AFFDL-TR-68-149 (Available as NTIS AD-686178).

Murdock, J.W., 1980, "The Generation of a Tollmien-Schlichting Wave by a Sound Wave," *Proceedings of the Royal Society of London*, Vol. 372, pp. 517-534.

Nayfeh, A.H., 1981, "Introduction to Perturbation Techniques," John Wiley & Sons, USA.

Nishioka, M. and Morkovin, M.V., 1986, "Boundary Layer Receptivity to Unsteady Pressure Gradients: Experiments and Overview," *Journal of Fluid Mechanics*, Vol. 171, pp. 219-261.

Orszag, S.A. and Kells, L.C., 1980, "Transition to Turbulence in Plane Poiseuille and Plane Couette Flows," *Journal of Fluid Mechanics*, Vol. 96, pp. 159-205.

Patera, A.T., 1984, "A Spectral Element Method for Fluid Dynamics: Laminar Flow in a Channel Expansion," *Journal of Computational Physics*, Vol. 54, No. 3, pp. 468-488.

Press, W.H., Teukolsky, S.A., Vetterling, W.T. and Flannery B.P., 1992, "Numerical Recipes in Fortran," Cambridge University Press, 2nd ed., USA.

Pulliam, T.H. and Vastano, J.A., 1993, "Transition to Chaos in an Open Unforced 2D Flow," *Journal of Computational Physics*, Vol. 105, pp. 133-149.

Rai, M.M., 1989, "Three-dimensional Navier-Stokes Simulations of Turbine Rotor-stator Interaction. Part I, Methodology; Part II, results. AIAA J. Prop. and Power. Vol. 5, No. 3, pp. 307-319.

Renaud, E.W., 1991, "Secondary Flow, Total Pressure Loss and the Effect of Circumferential Distortions in Axial Turbine Cascades," Ph.D. Thesis, Massachusetts Institute of Technology.

Reynolds, A.J., 1974, "Turbulent Flows in Engineering," John Wiley & Sons, USA.

Roberts, W.B., 1975, "The Effect of Reynolds Number and Laminar Separation on Axial Cascade Performance," *Journal of Engineering for Power*, April, pp. 261-273.

Rojas, L.R. and Amon, C.H., 1995, "Direct Numerical Simulations of Boundary Layer Instabilities in Subsonic Cascade Flows Triggered by Free-Stream Disturbances," *Proceedings of the Third Caribbean Congress on Fluid Dynamics and the Third Latin-American Symposium on Fluid Mechanics*, Caracas, Venezuela.

Rojas, L.R. and Amon, C.H., 1997, "Resonant Interaction Between Boundary Layer Instabilities and Free-Stream Disturbances in Cascade Flows," to be submitted to *Journal of Fluids Engineering*.

Rønquist, E., 1988, "Optimal Spectral Element Methods for the Unsteady Three-Dimensional Incompressible Navier-Stokes Equations," PhD. Thesis, Massachusetts Institute of Technology.

Schlichting, H., 1979, "Boundary-Layer Theory," McGraw-Hill Publishing Company, 7th ed., New York.

Shapiro, P.J., 1977, "The Influence of Sound Upon Laminar Boundary Layer Instability," MIT Acoustics and Vibration Lab. Rep. 83458-83560-1.

Sherman, F.S., 1990, "Viscous Flow," McGraw-Hill, Inc., 1st ed., USA.

Simon, F.F. and Ashpis, D.E., 1996, "Progress in Modeling of Laminar to Turbulent Transition on Turbine Vanes and Blades," International Conference on Turbulent Heat Transfer sponsored by the Engineering Foundation, NASA Technical Memorandum 107180.

Tam, C.K., 1981, "The Excitation of Tollmien-Schlichting Waves in Low Subsonic Boundary Layers by Free-Stream Sound Waves," *Journal of Fluid Mechanics*, Vol. 109, pp. 483-501.

Tan, C.S., 1989, "A Multi-Domain Spectral Computation of Three-Dimensional Laminar Horseshoe Vortex Flow Using Incompressible Navier-Stokes Equations," *Journal of Computational Physics*, Vol. 85, pp. 130-158.

Temam, R., 1977, "Navier-Stokes Equations," North-Holland, Amsterdam.

Temekes, H. and Lumley, J.L., 1972, "A First Course in Turbulence," MIT Press, Cambridge.

Thomas, A.S., 1983, "The Control of Boundary Layer Transition Using a Wave-Superposition Principle," *Journal of Fluid Mechanics*, Vol. 137, pp. 233-250.

Townsend, A.A., 1956, "The Structure of Turbulent Shear Flow," Cambridge.

Townsend, A.A., 1970, " Entrainment and the Structure of Turbulent Flow," *Journal of Fluid Mechanics*, Vol. 41, pp. 13-46.

Van Fossen, G.J., Simoneau, R.J. and Ching, C.Y., 1995, "Influence of Turbulence Parameters, Reynolds Number, and Body Shape on Stagnation-Region Heat Transfer," *Journal of Heat Transfer*, Vol. 117, pp. 597-603.

Walker, G.J. and Gostelow, J.P., 1990, "Effects of Adverse Pressure Gradients on the Nature and Length of Boundary Layer Transition," *Journal of Turbomachinery*, Vol. 112, pp. 196-205.

Walker, G.J., 1993, "The Role of Laminar-Turbulent Transition in Gas Turbine Engines: A Discussion," *Journal of Turbomachinery*, Vol. 115, pp. 207-217.

Wang, T. and Simon, T.W., 1987, "Heat Transfer and Fluid Mechanics Measurements in Transitional Boundary Layers on Convex-Curved Surfaces," *Journal of Turbomachinery*, Vol. 109, pp. 443-452.

Wlezien, R. W., "Measurement of Boundary Layer Receptivity: Challenges and Frontiers," *ASME: FED Transitional and Turbulent Compressible Flows*, Vol. 224, pp. 1-8, 1995.

TABLE I Performance of the numerical code running on different platforms, based on extension of converged cases. All the simulations are performed on the 5x5(x5) unless otherwise indicated.

Simulation				CPU Performance	
Dim	**Re**	**Others**	**Memory(MB)**	**Type**	**hrs/time-step**
2-D	600	basic flow	25	DEC-5000 (32MB Ram)	0.29
2-D	1000	ε=0.02; ω_d=1099.5	25	Alpha 200-4/166 (96 MB Ram) SPECfp95*=3.64	0.24
2-D	800	basic flow	25	Alpha 200-4/233 (96 MB Ram) SPECfp95*=4.32	0.06
2-D	1000	ε=0.02; ω_d=26.4	25	"	0.12
3-D	400	ε=0.02; ω_d=26.4	80	"	0.83
3-D	400	ε=0.02; ω_d=1099.5	80	"	0.68
2-D	400	basic flow	44(max.)	CRAY C90 PSC.1-proc. (8GB Ram)	0.0012
3-D	400	basic flow**	472(max.)	"	0.0038

* SPECfp95 is the floating point performance ratio using a SPARCstation 10/40 (40 Mhz SuperSPARC with no L2 cache) as the reference CPU.

** Running on 7x7x7 mesh

TABLE II Fitted expressions of the non-dimensional boundary layer thickness δ/c as a function of the non-dimensional arclength s/c and the arclength Reynolds number Re_s over the airfoil suction side for basic flows ($Re_s = U_\infty.s/\nu$)

Re	**δ/c**
231	$3.614(s/c)\,Re_s^{-0.5172}$
400	$3.042(s/c)\,Re_s^{-0.4706}$
1000	$2.017(s/c)\,Re_s^{-0.3935}$

TABLE III Dimensional values of the natural frequency ($\omega^*_{2D\text{-}1000}$) and the free-stream velocity (U_∞) for Re=1000, using air at room temperature as working fluid (ρ=0.0735 lbm/ft^3; μ=1.241x10^{-5} lbm/ft-s @ T=80 °F).

c [ft]	U_∞[ft/s]	$\omega^*_{2D\text{-}1000}/(2\pi)$ [Hz]
0.1	1.688	79.40
0.2	0.844	19.85
0.3	0.563	8.82
0.4	0.422	4.96
0.5	0.338	3.18
0.6	0.281	2.21
0.7	0.241	1.62

TABLE IV Non-dimensional frequency of the least stable mode, estimated using linear stability analysis of the Orr-Sommerfeld equation for parallel plates. The left and right extremes of the range correspond to the calculation using the equivalent distance between the two contiguous airfoils at the entrance and at the exit, respectively.

Re	**$\omega_{LS}=\omega_{LS}^*.c/U_\infty$**
231	1.1-6.1
400	1.0-5.6
1000	0.9-5.0

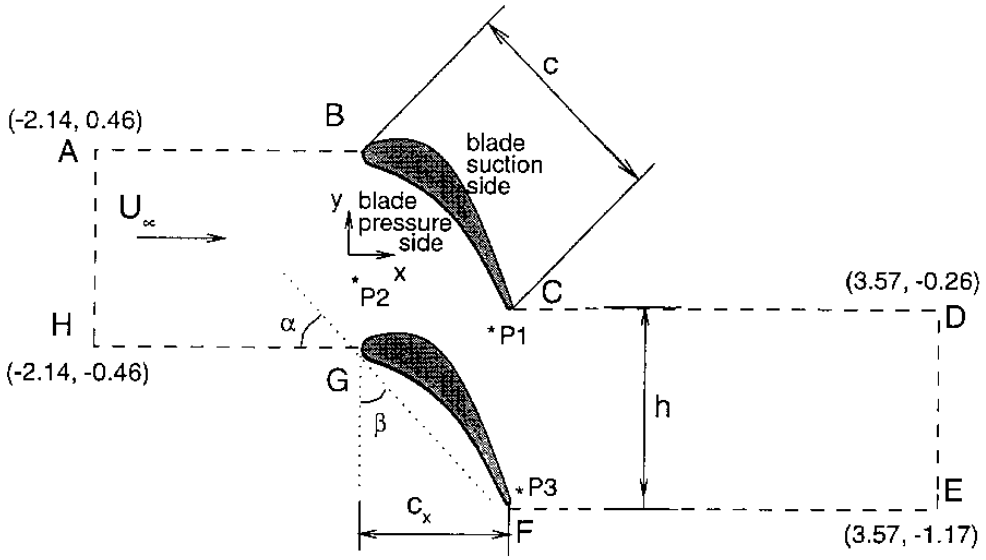

FIGURE 1. Two-dimensional computational domain depicting relative dimensions and history points (P1, P2 and P3) locations. Low-solidity (h/c=0.914), experimental axial gas turbine first stator.

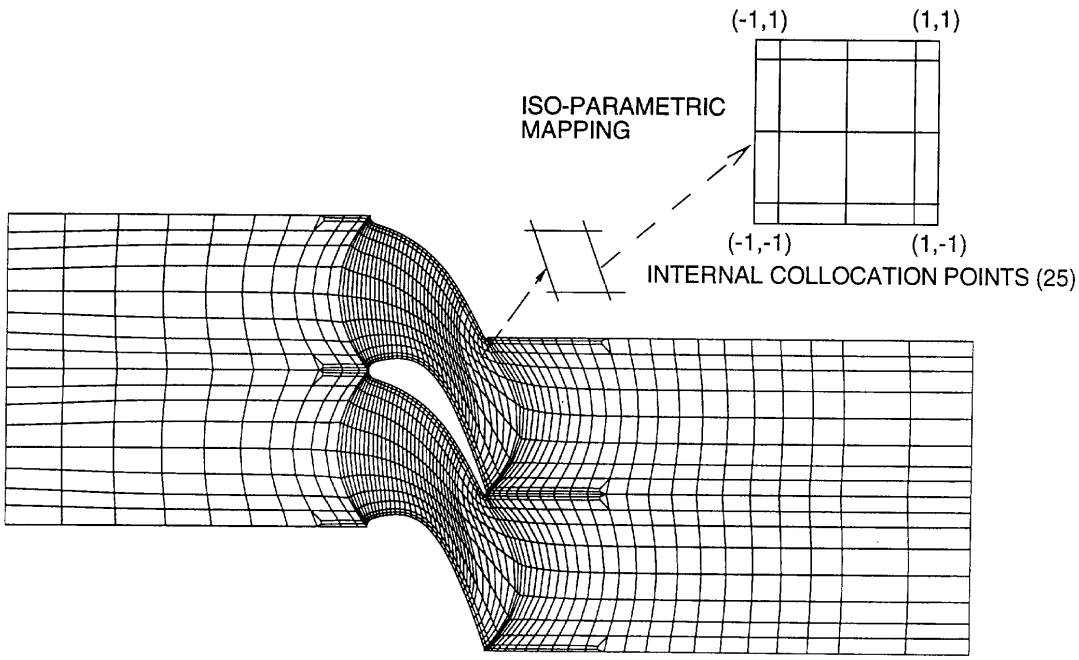

FIGURE 2. Typical spectral two-dimensional mesh discretization including collocation points. 784 macro-elements and 25 collocation points per macro-element.

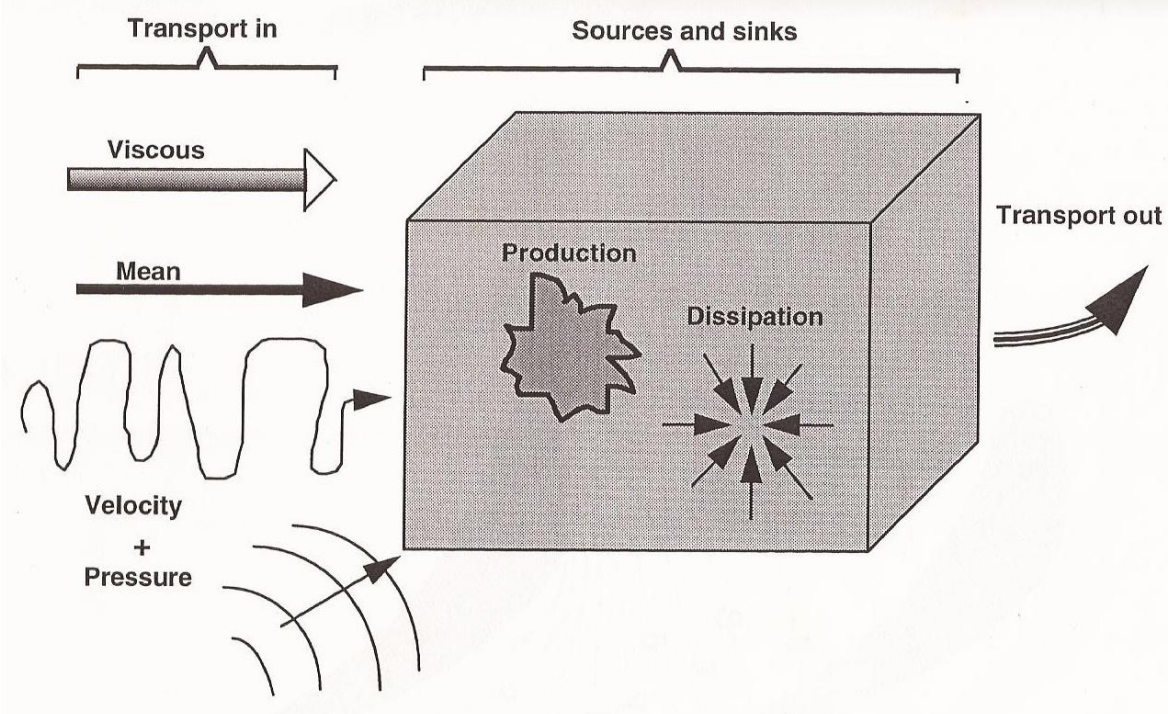

FIGURE 3. Balance of Fluctuating Kinetic Energy in an elementary control volume. Includes the transport, production and dissipation terms.

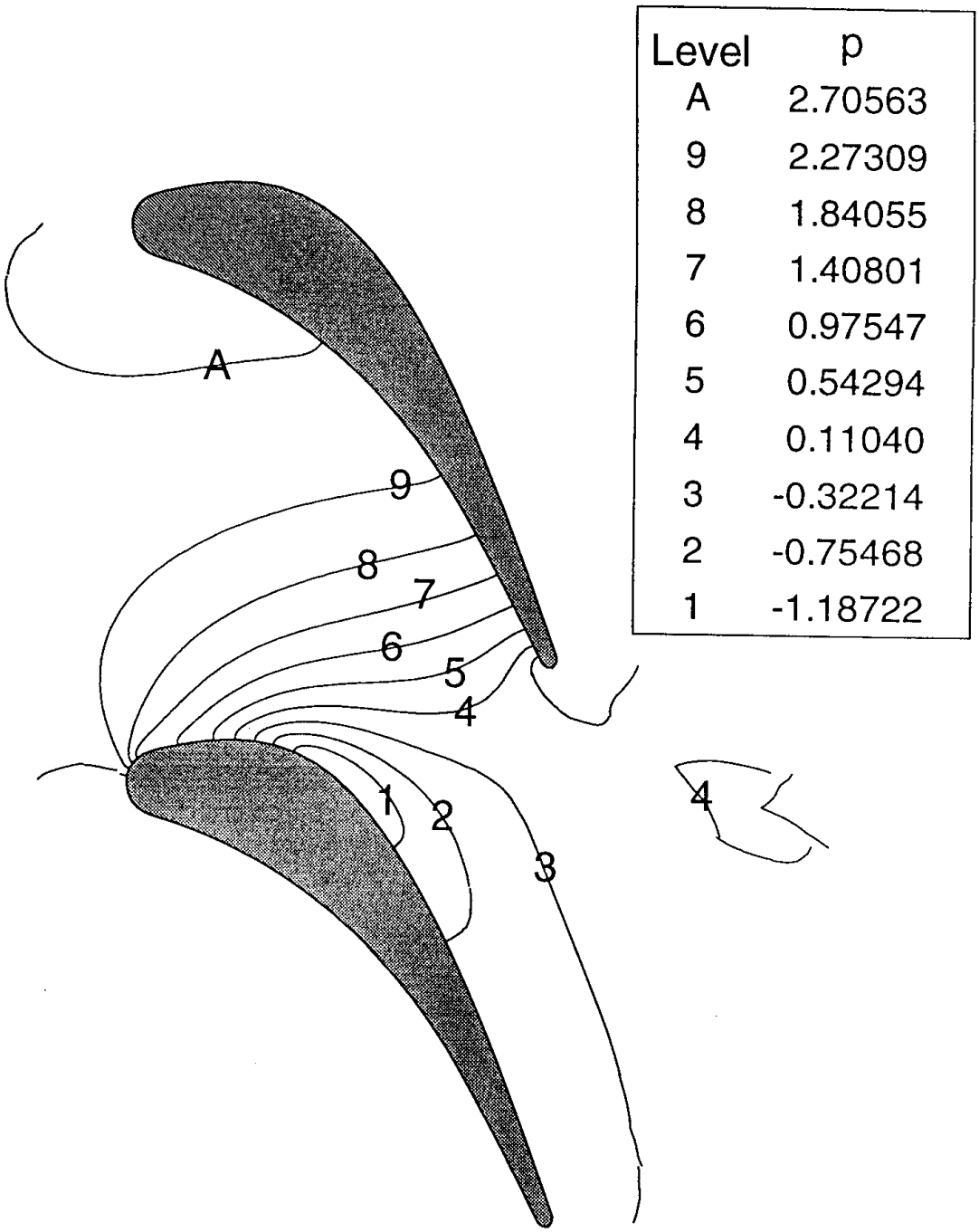

FIGURE 4. Mean pressure contour plot for the basic flow at Re=1000.

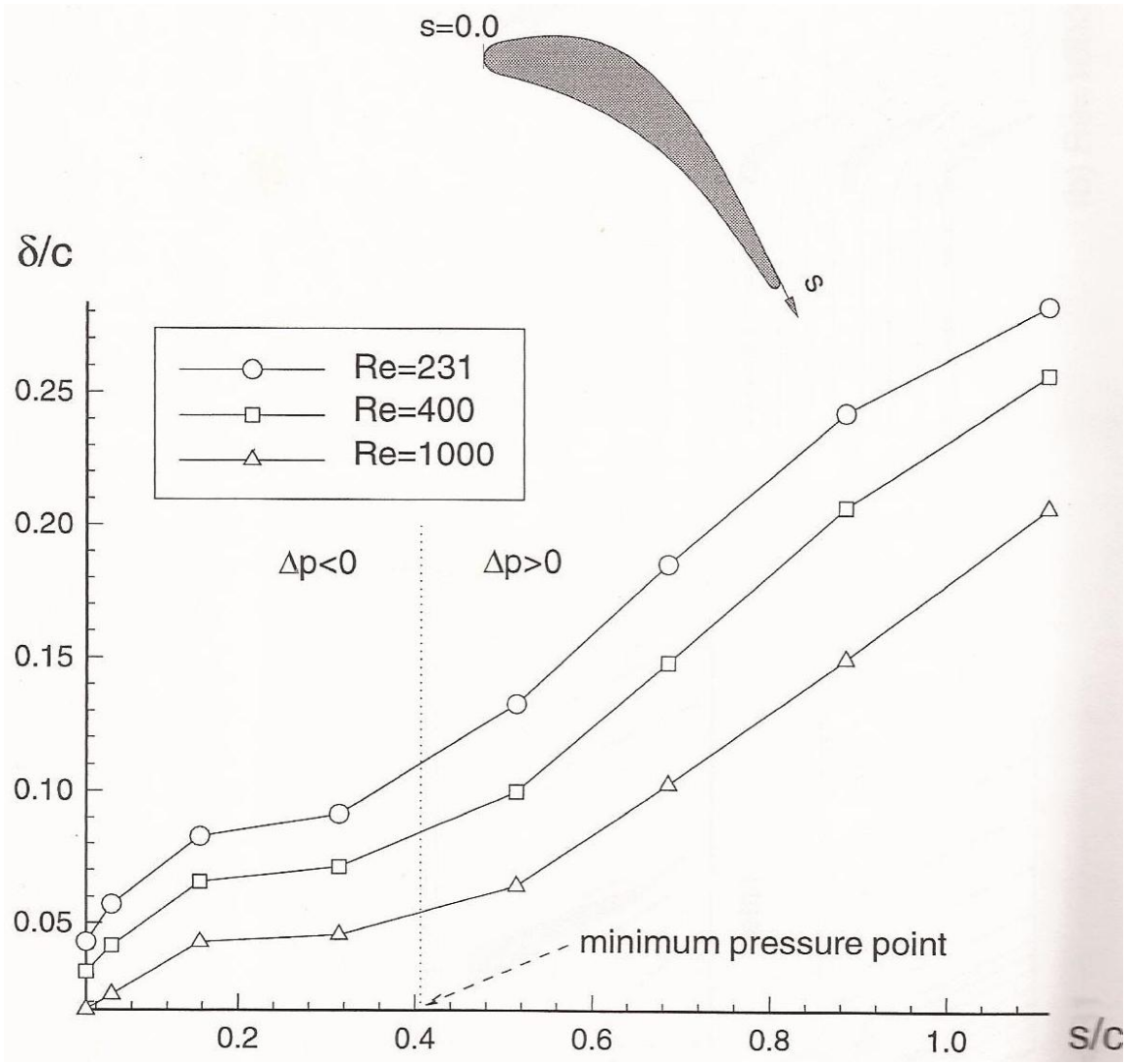

FIGURE 5. Boundary layer thickness δ non-dimensionalized by the blade chord c as a function of Re and the airfoil suction-side arclength.

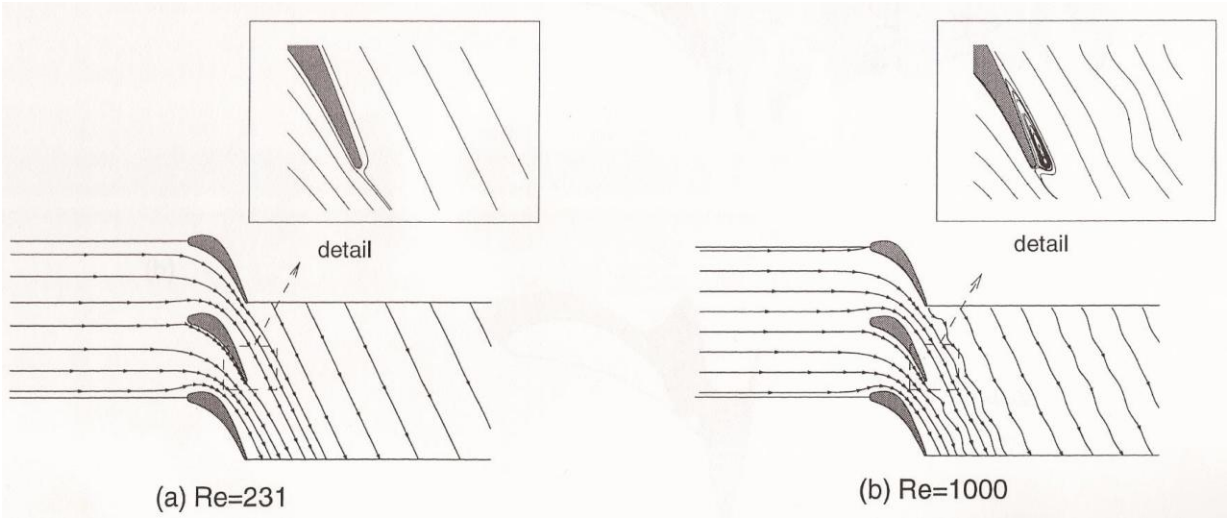

FIGURE 6. Streamtraces for the basic flows at Re=231 and Re=1000.

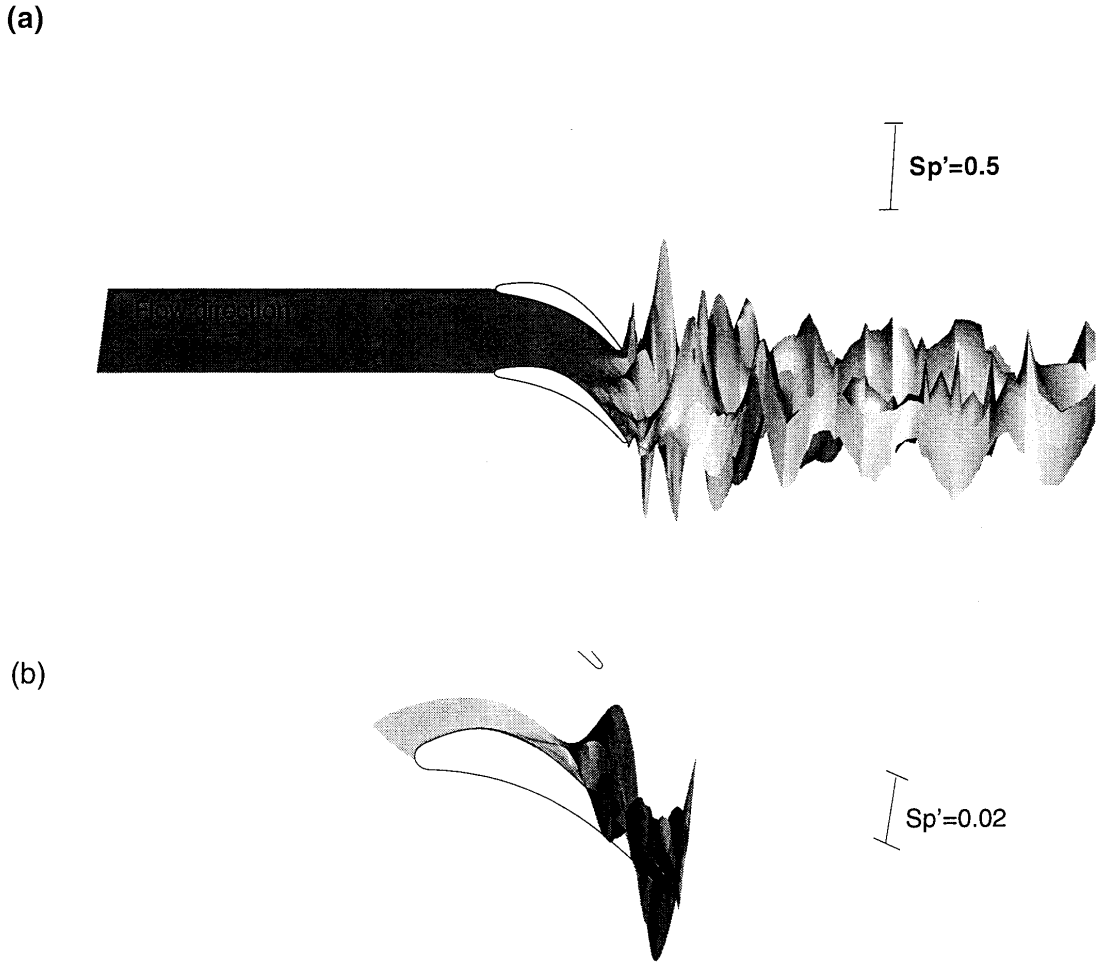

FIGURE 7. Carpet plot of Sp' throughout the entire domain at a characteristic time for basic flow at Re=1000.

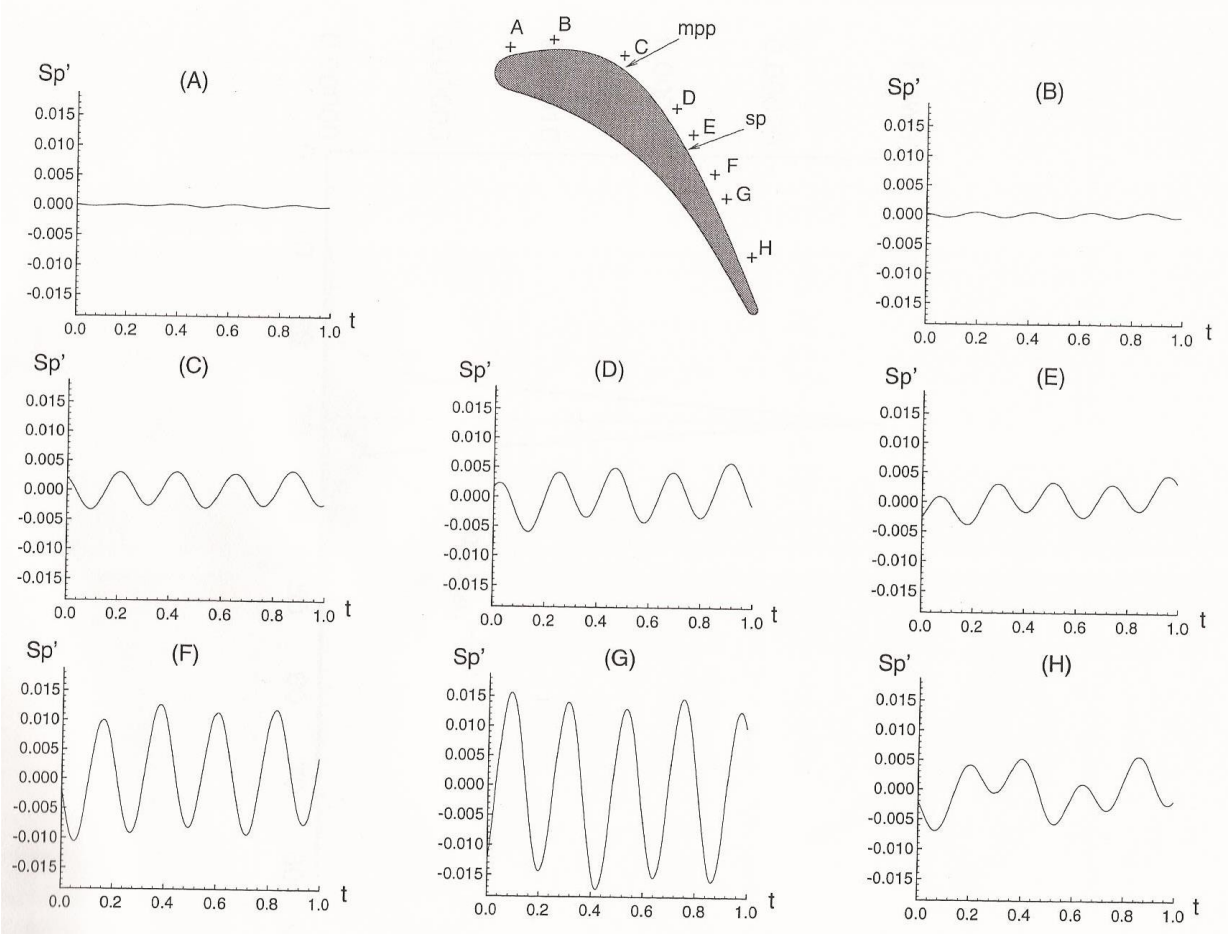

FIGURE 8. Sp' vs. time at eight locations close to the suction-side wall ($d_n/c=0.0115$) along the streamwise direction. Basic flow at Re=1000.

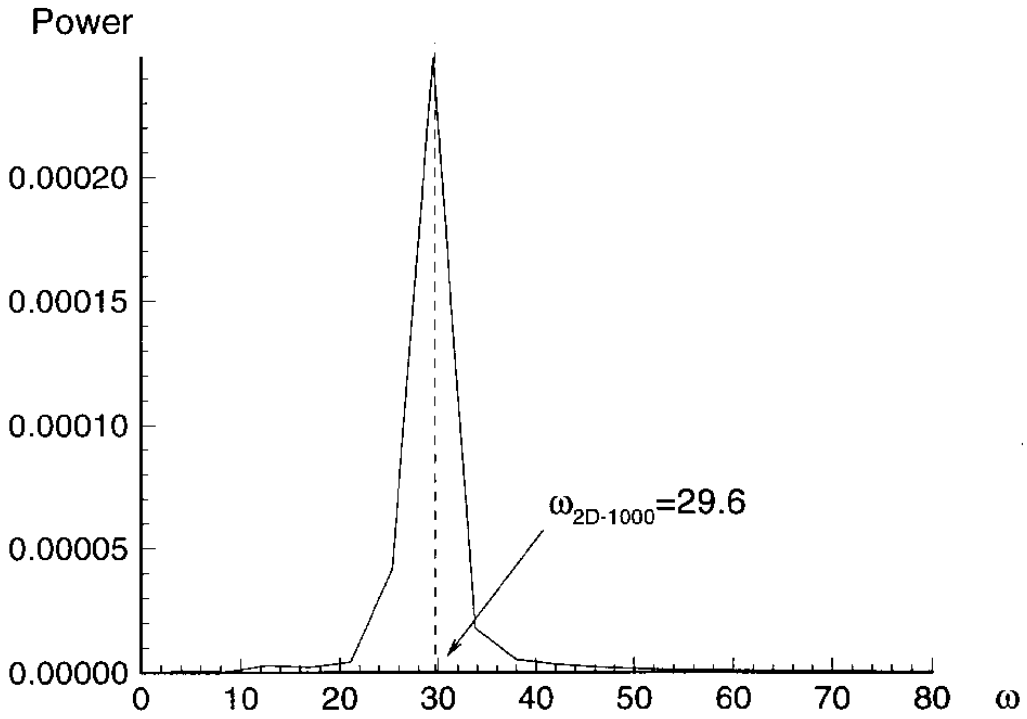

FIGURE 9. Fourier power spectrum of the x-velocity at point P1. Basic flow at Re=1000.

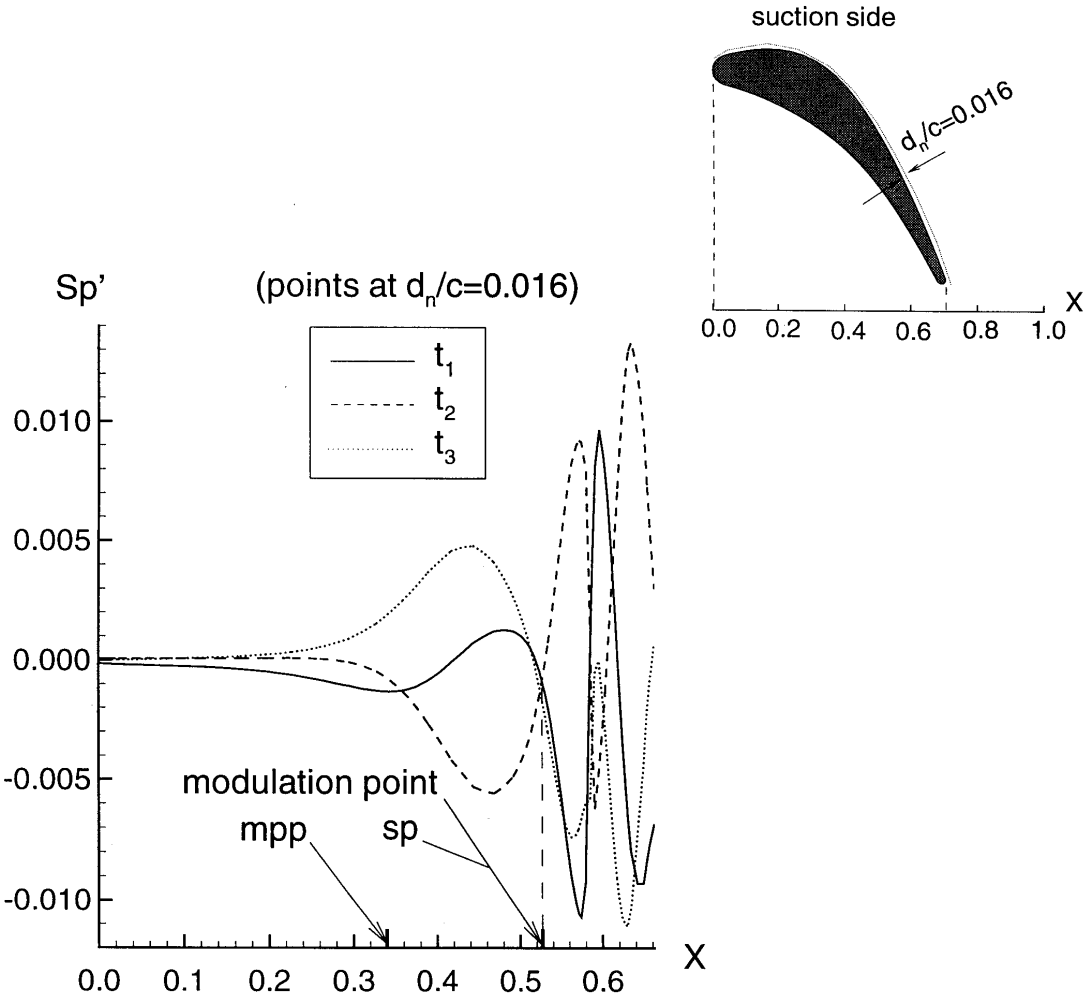

FIGURE 10. Wavelength modulation observed in Sp' vs. time plot along line close to the suction-side wall ($d_n/c=0.016$) at three different times within one period of the fluctuation. Basic flow at Re=1000.

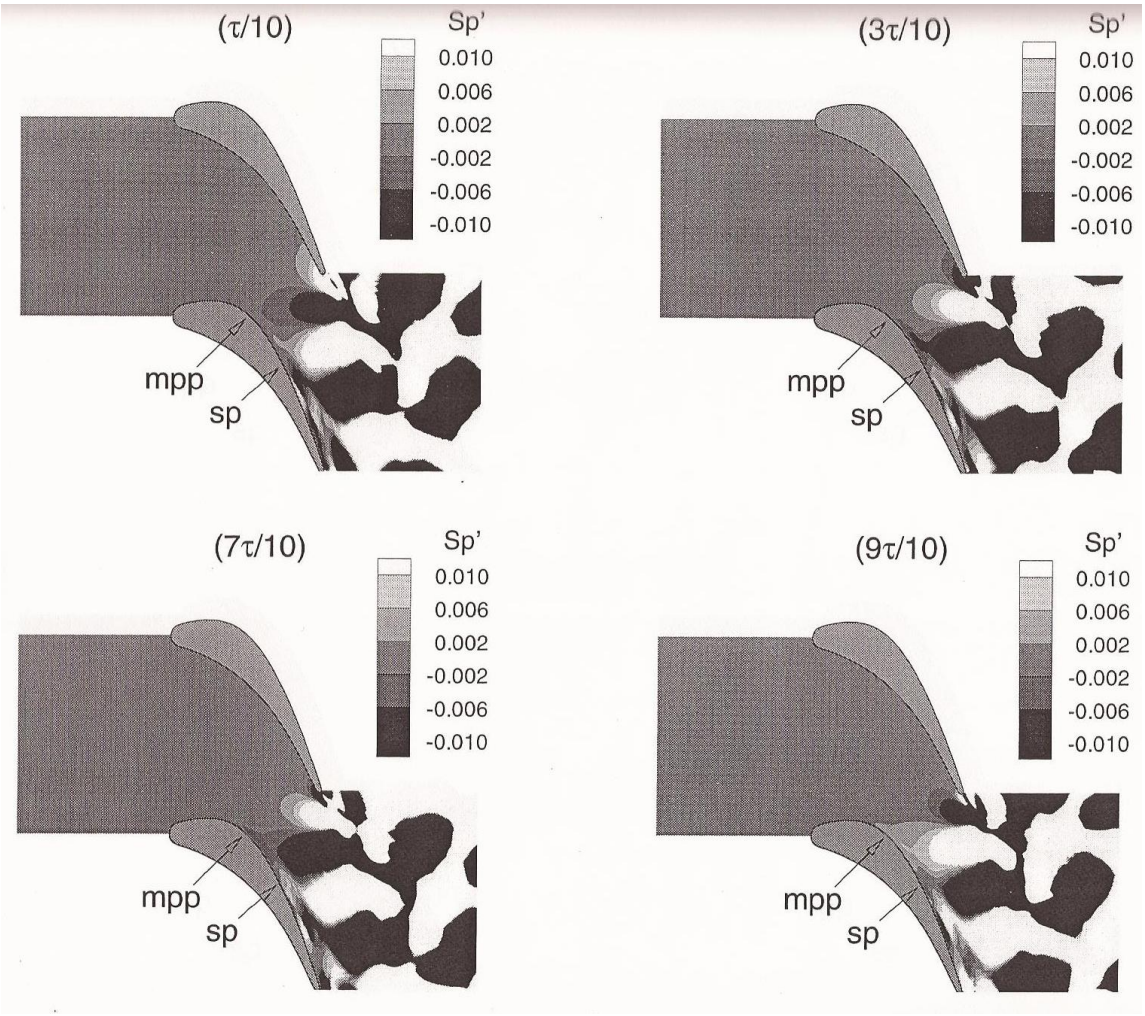

FIGURE 11. Contour plot of Sp' throughout the entire domain at four equally-spaced times within one period of the fluctuation. Basic flow at Re=1000.

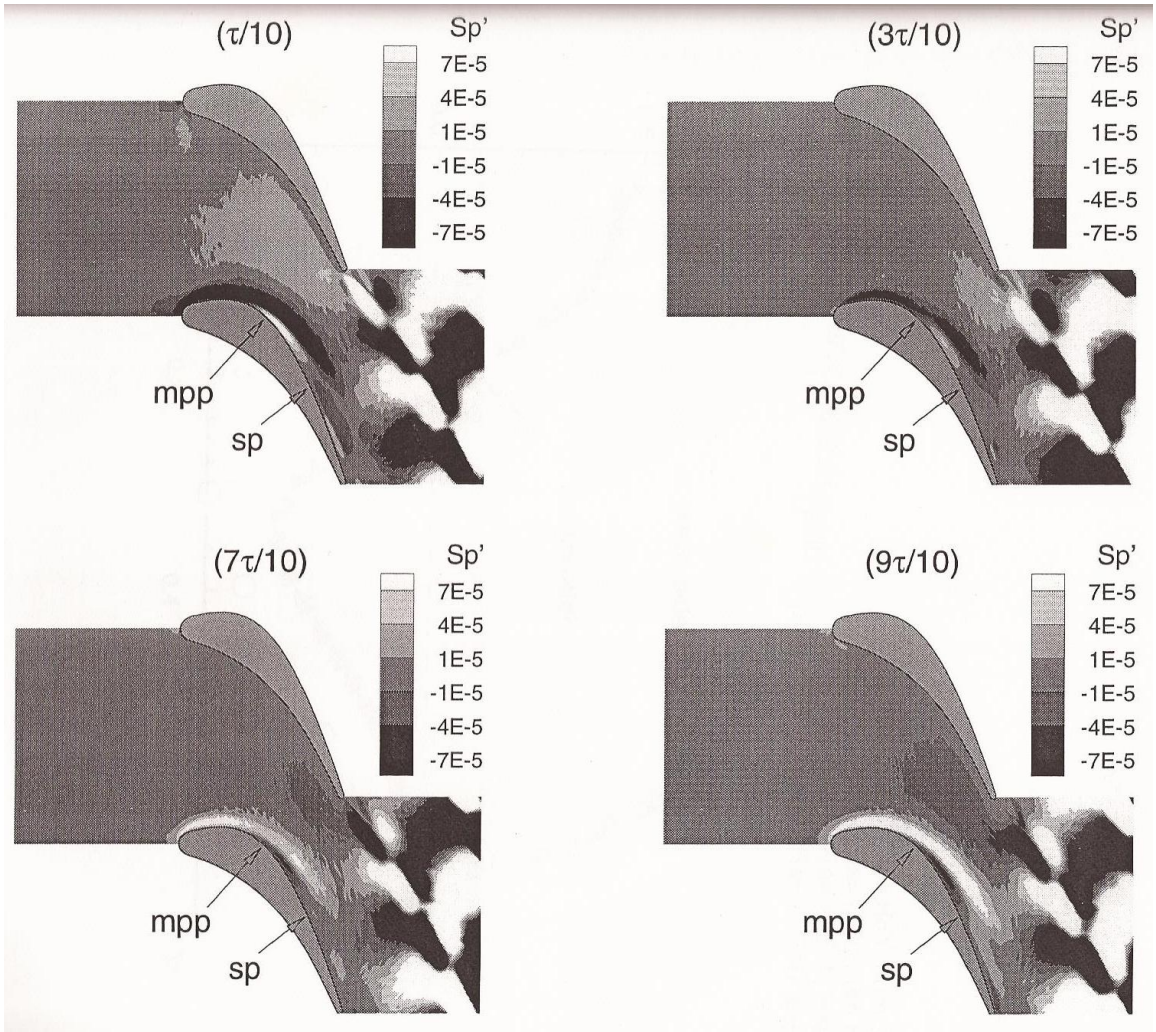

FIGURE 12. Contour plot of Sp' throughout the entire domain at four equally-spaced times within one period of the fluctuation. Basic flow at Re=600.

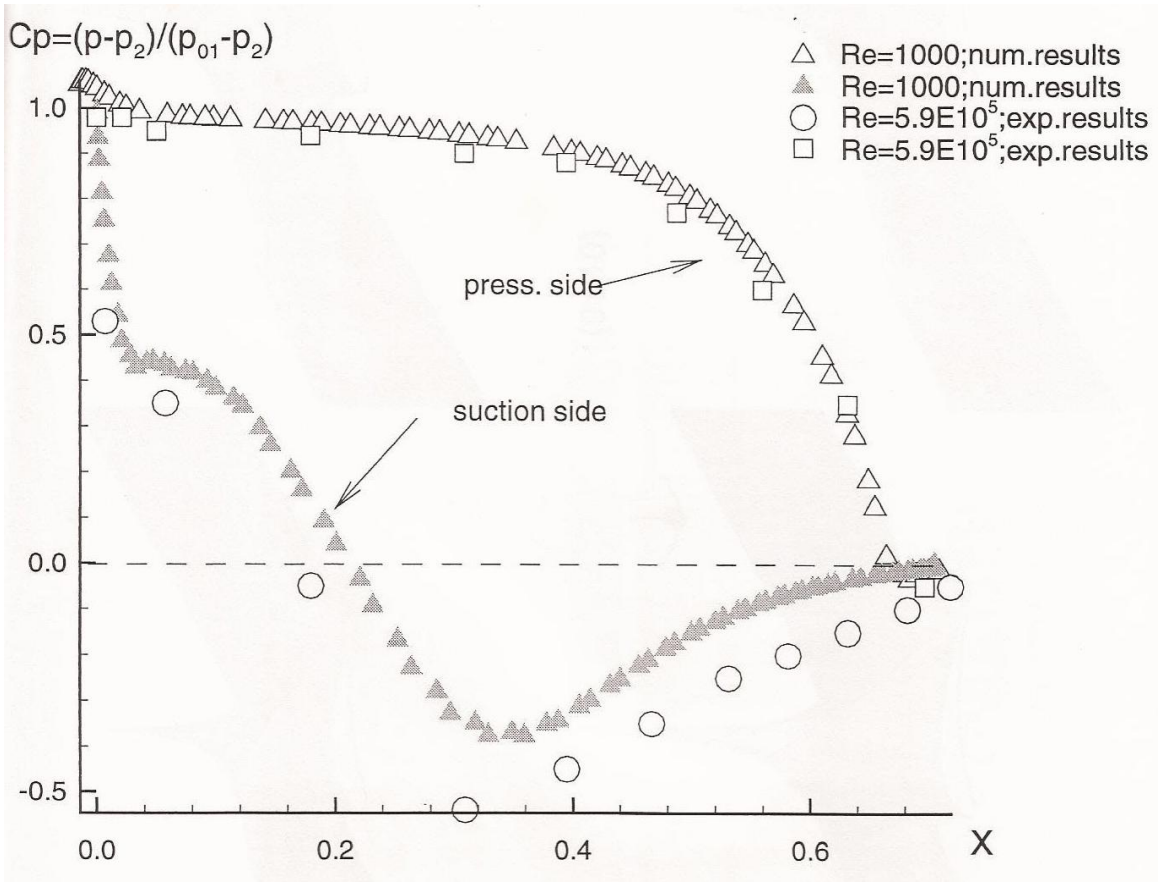

FIGURE 13. Comparison between the mean flow pressure coefficient C_p obtained numerically at Re=1000 and the one obtained experimentally by Dring et al. (1987) at Re=5.9x10^5.

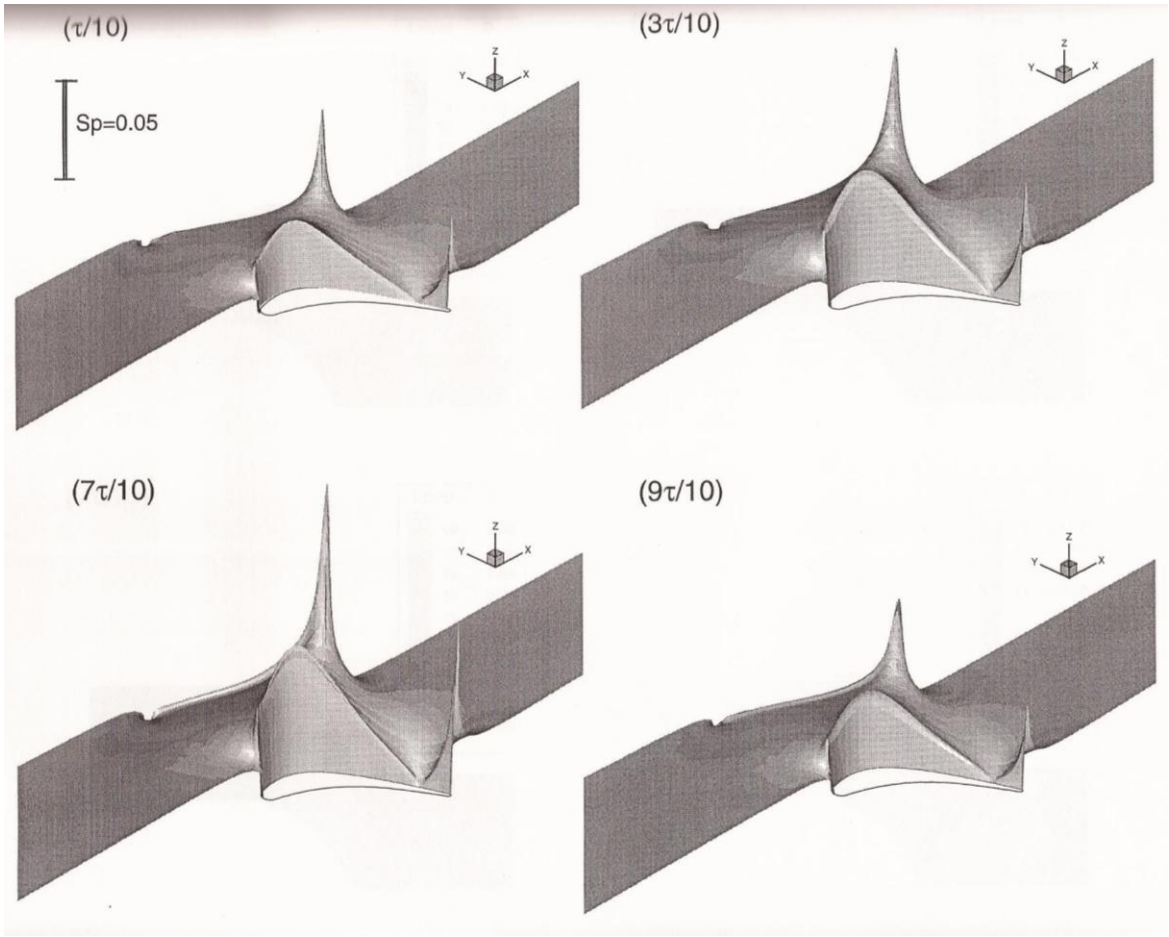

FIGURE 14a. Stokes wave generated by the superposed perturbation with ω_d=26.4 and ε=0.02. Carpet plot of Sp.

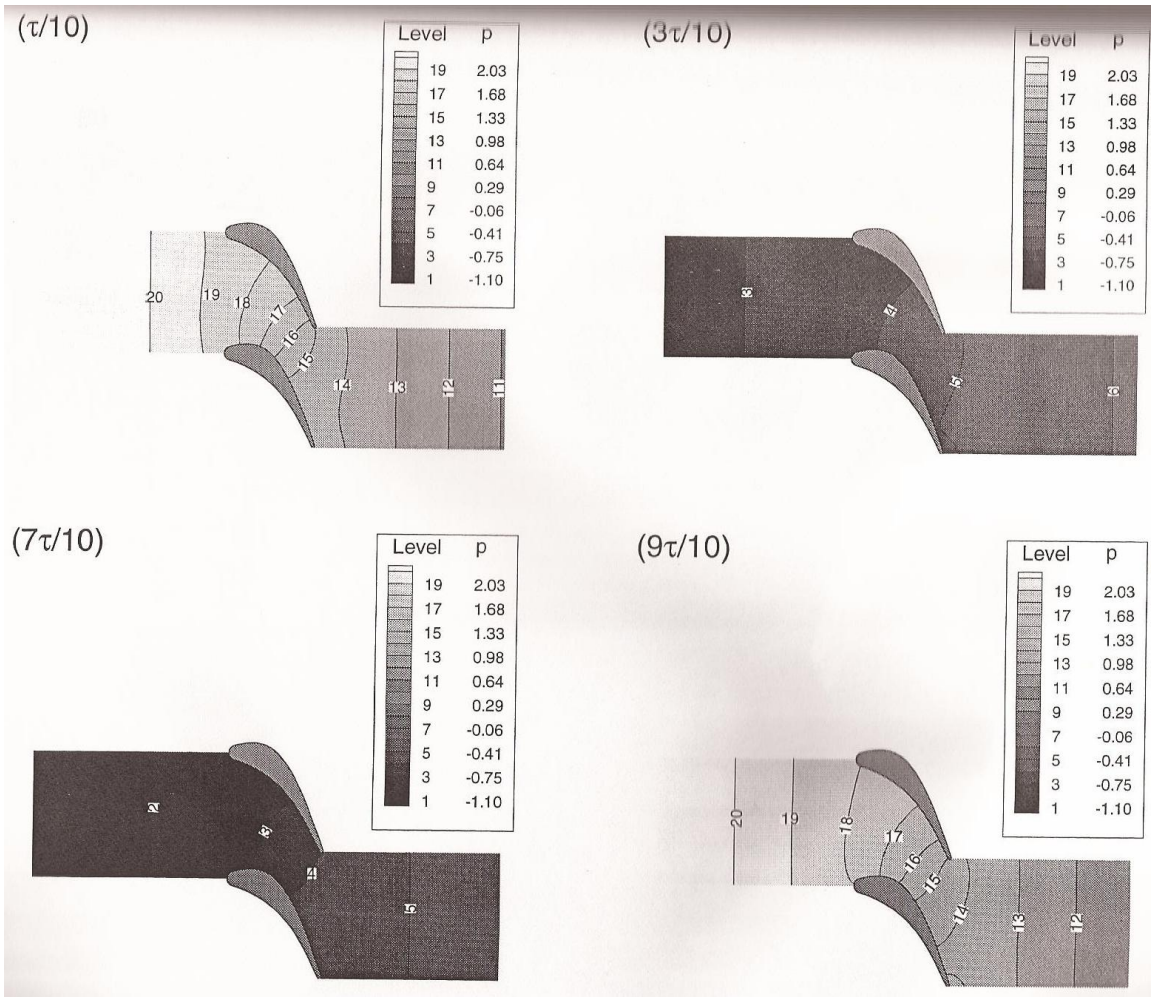

FIGURE 14b. Stokes wave generated by the superposed perturbation with ω_d=26.4 and ε=0.02. Contour plots of p at four equally-spaced times within the perturbation period.

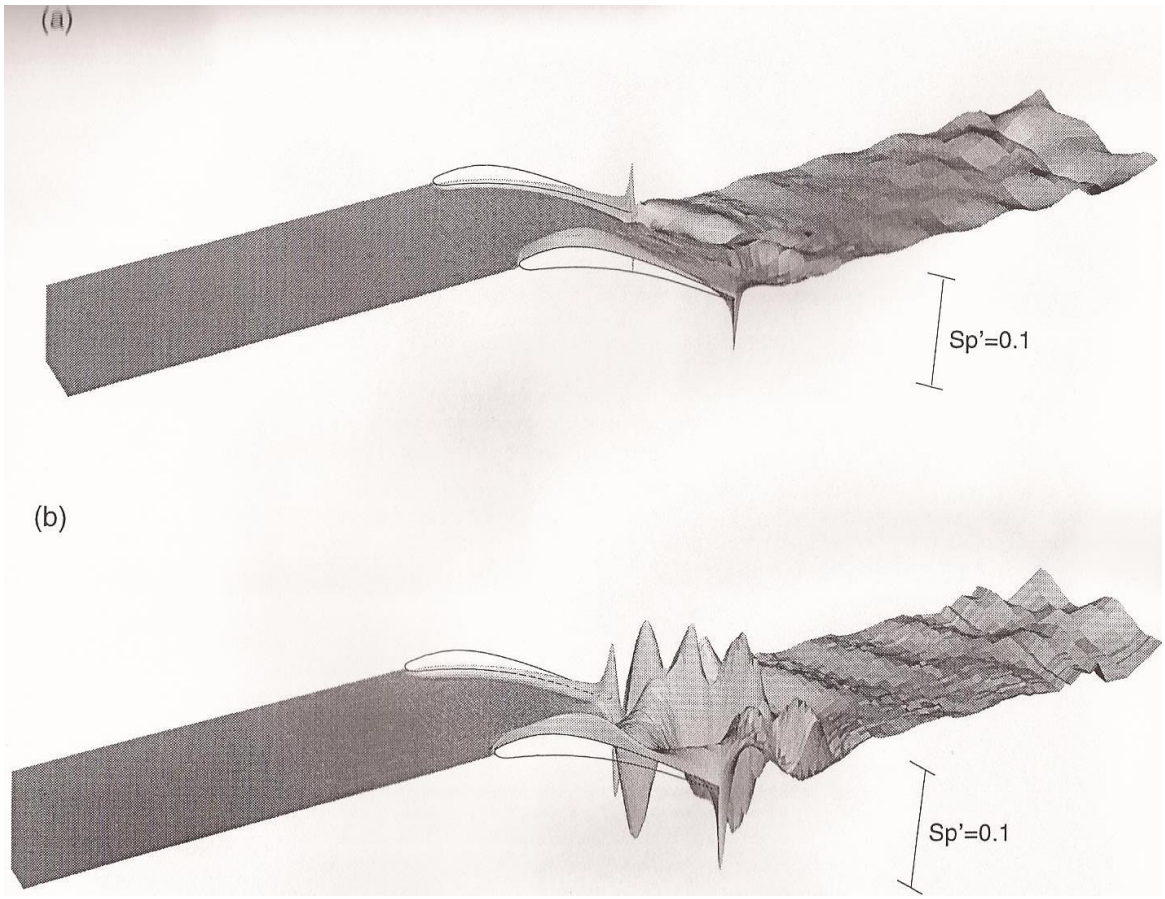

FIGURE 15. Carpet plots of Sp' at the moment when inlet perturbation vanishes for subcritical perturbed flow. Re=231 and ε=0.02. (a) ω_d=1099.5; (b) ω_d=26.4.

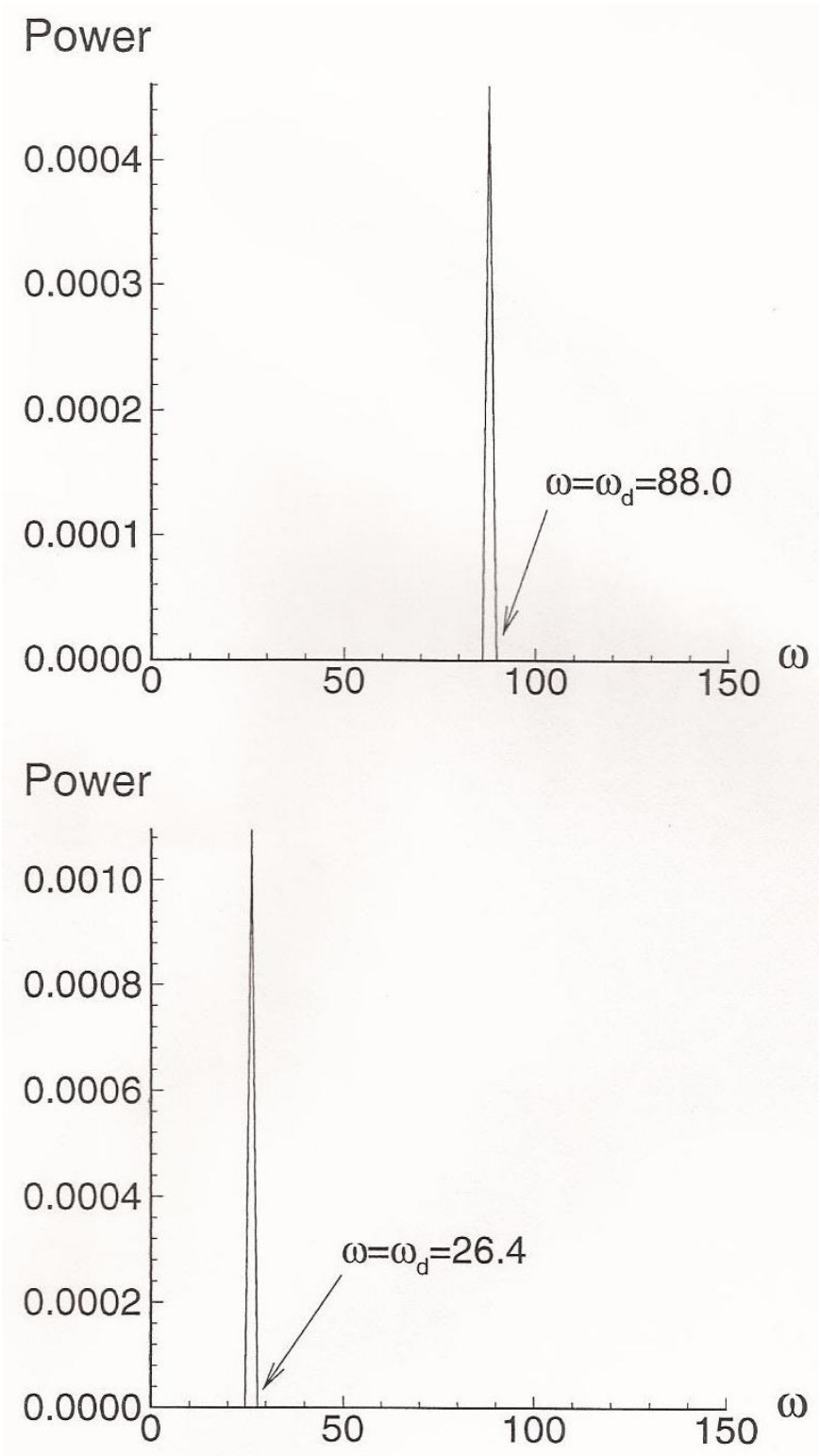

FIGURE 16a. Local measurement of the subcritical perturbed field at Re=231. Subcritical flow perturbated with ε=0.02 and, ω_d=1099.5 and ω_d=26.4. Fourier power spectrum of the x-velocity at point P1.

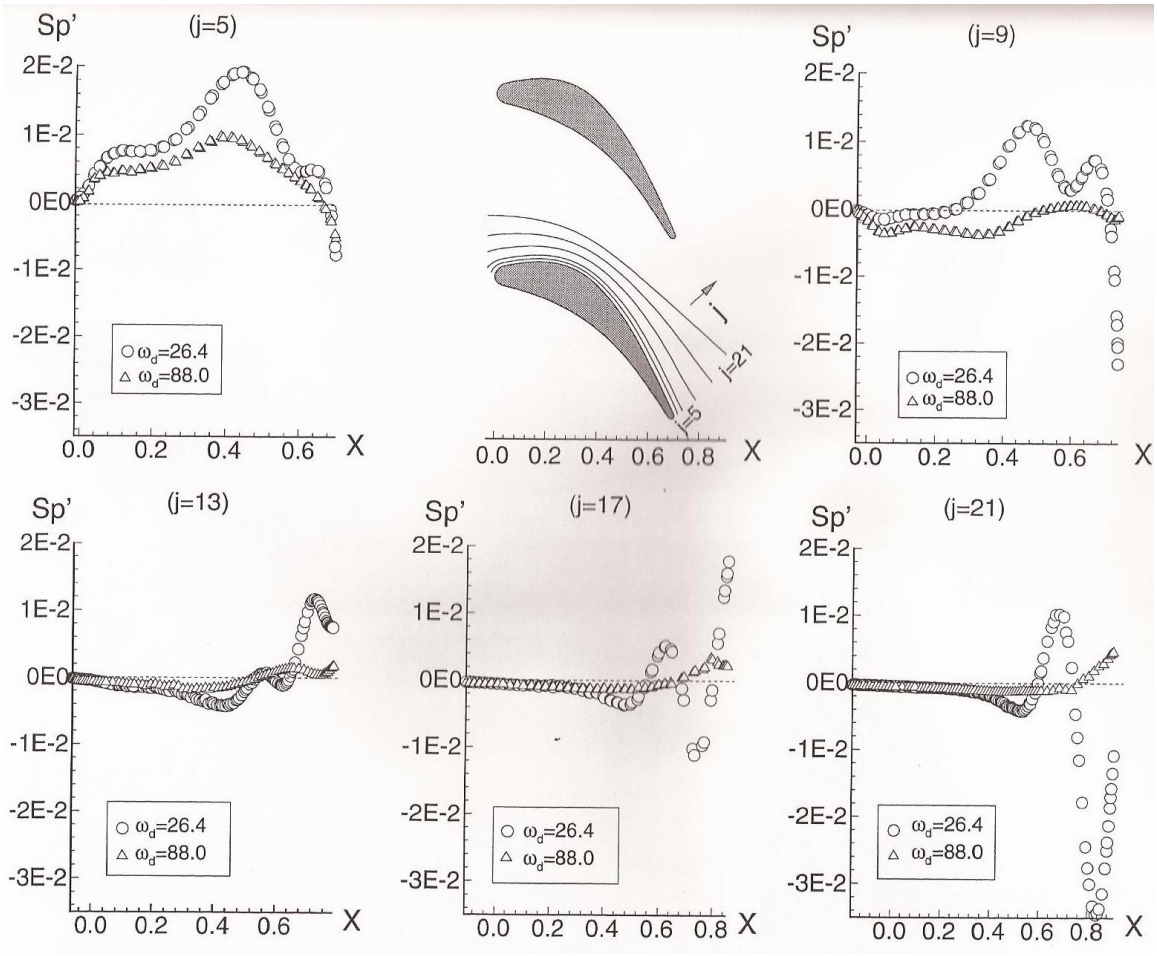

FIGURE 16b. Local measurement of the subcritical perturbed field at Re=231. Subcritical flow perturbated with ε=0.02 and, ω_d=1099.5 and ω_d=26.4. Sp' vs. along quasi-parallel lines to the suction-side wall.

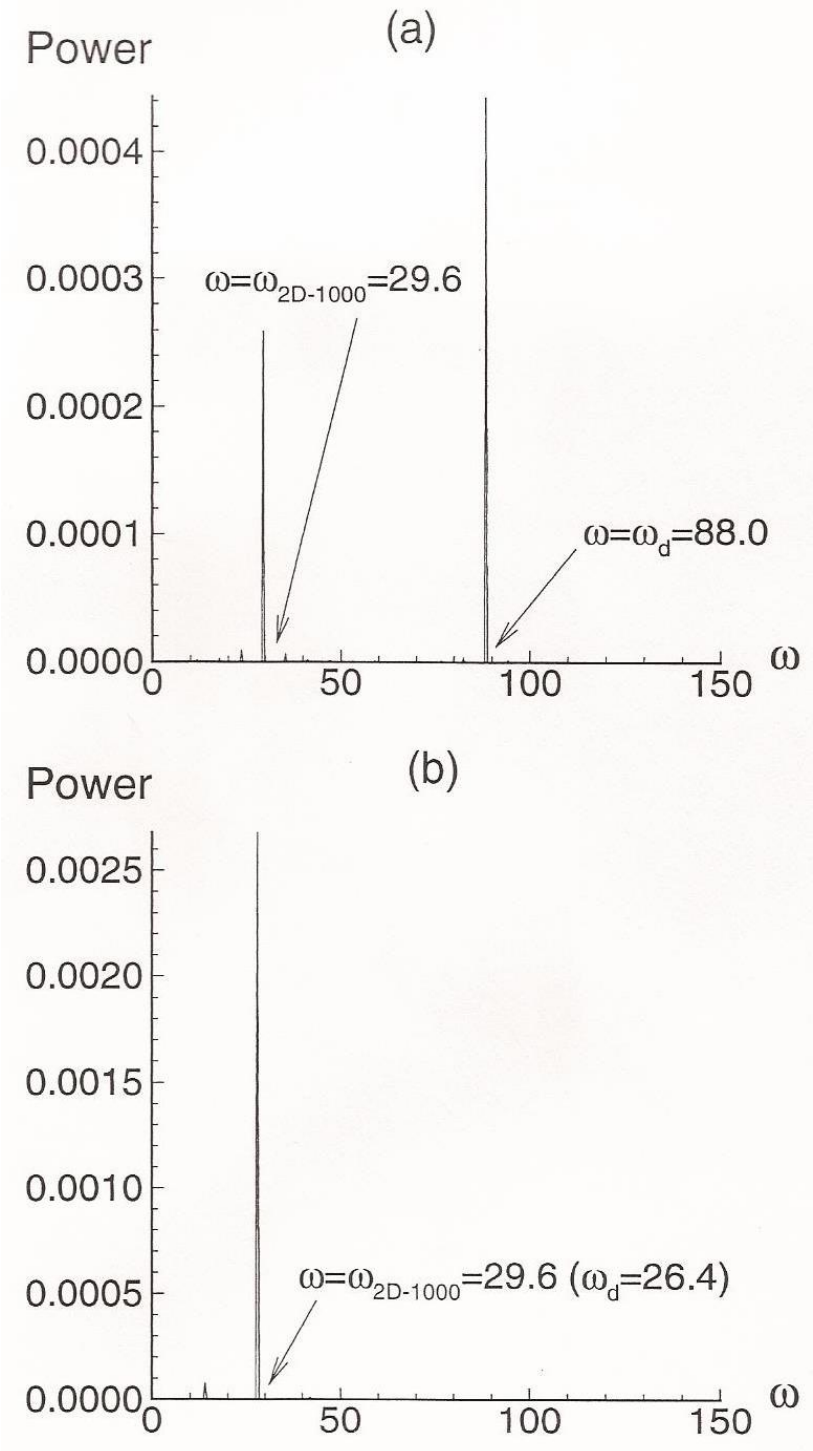

FIGURE 17. Local measurement of the supercritical perturbed field at Re=1000 perturbated with ε=0.02. Fourier power spectrum of x-velocity at point P1. (a) ω_d=1099.5; (b) ω_d=26.4.

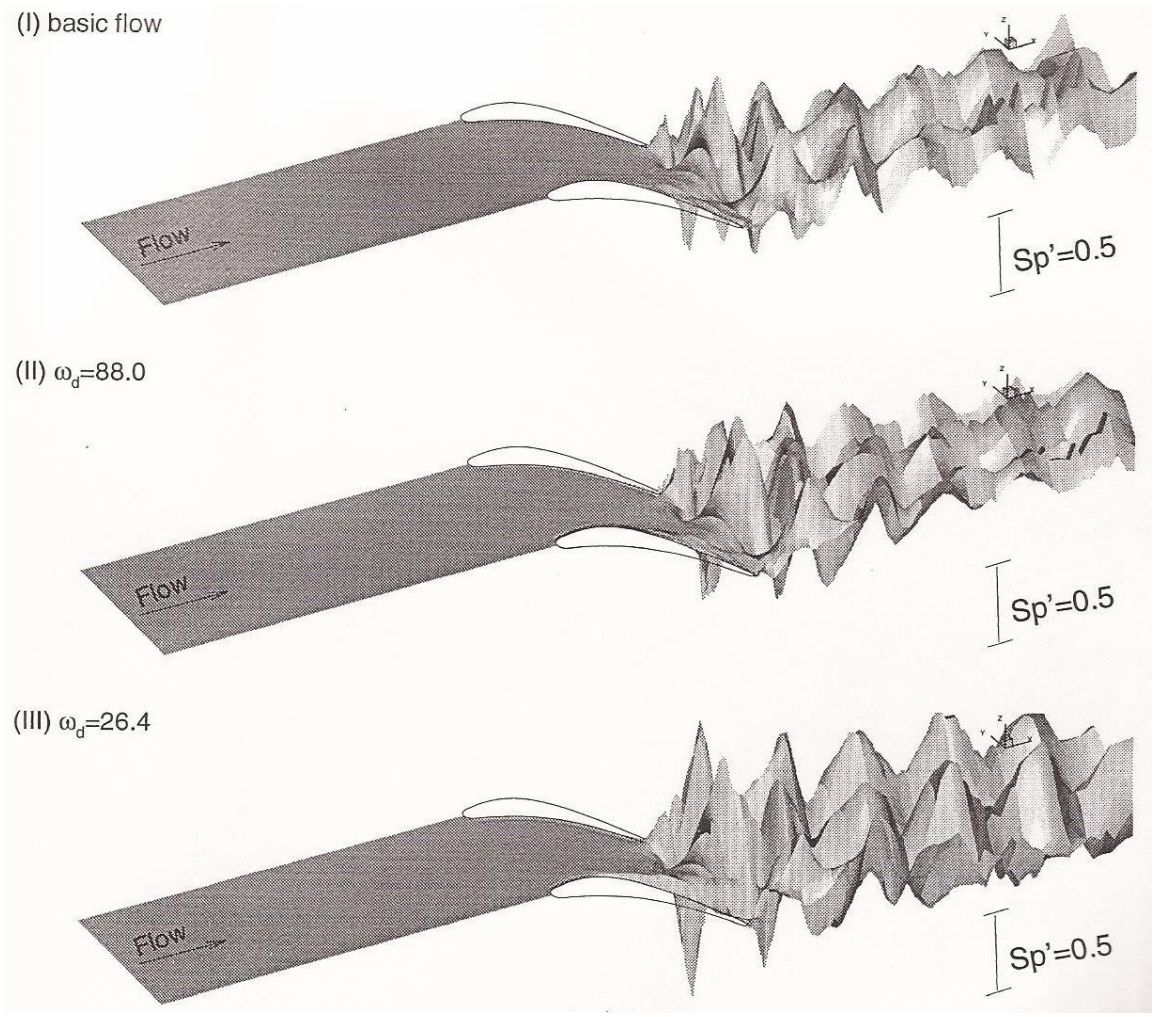

FIGURE 18a. Carpet plot of Sp' at the moment when inlet perturbation vanishes for supercritical perturbed flow. Re=1000 and ε=0.02. ω_d=1099.5.

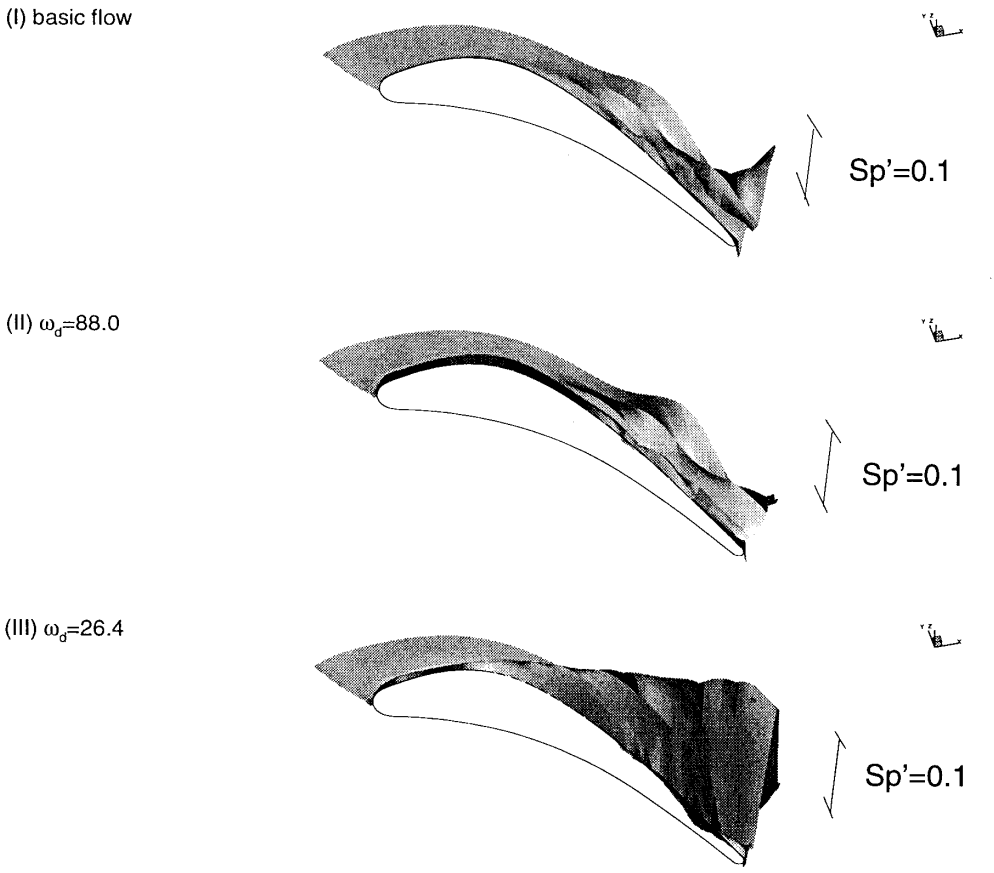

FIGURE 18b. Carpet plot of Sp' at the moment when inlet perturbation vanishes for supercritical perturbed flow. Re=1000 and ε=0.02. ω_d=26.4.

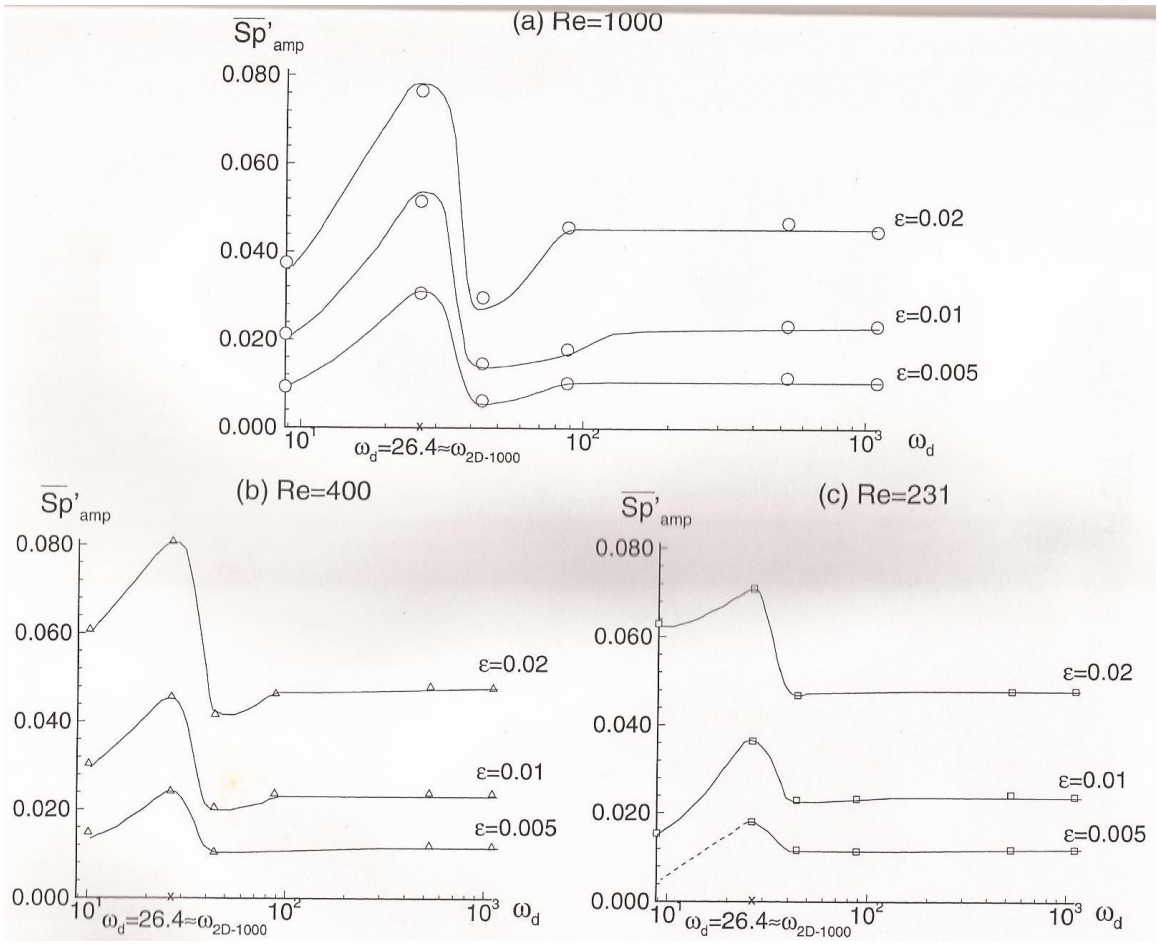

FIGURE 19. Local receptivity measurement at point P1. Sp'_{amp} vs. ω_d, ε and Re. ($231 \leq Re \leq 1000$; $0.005 \leq \varepsilon \leq 0.02$; $8.8 \leq \omega \leq 1100$).

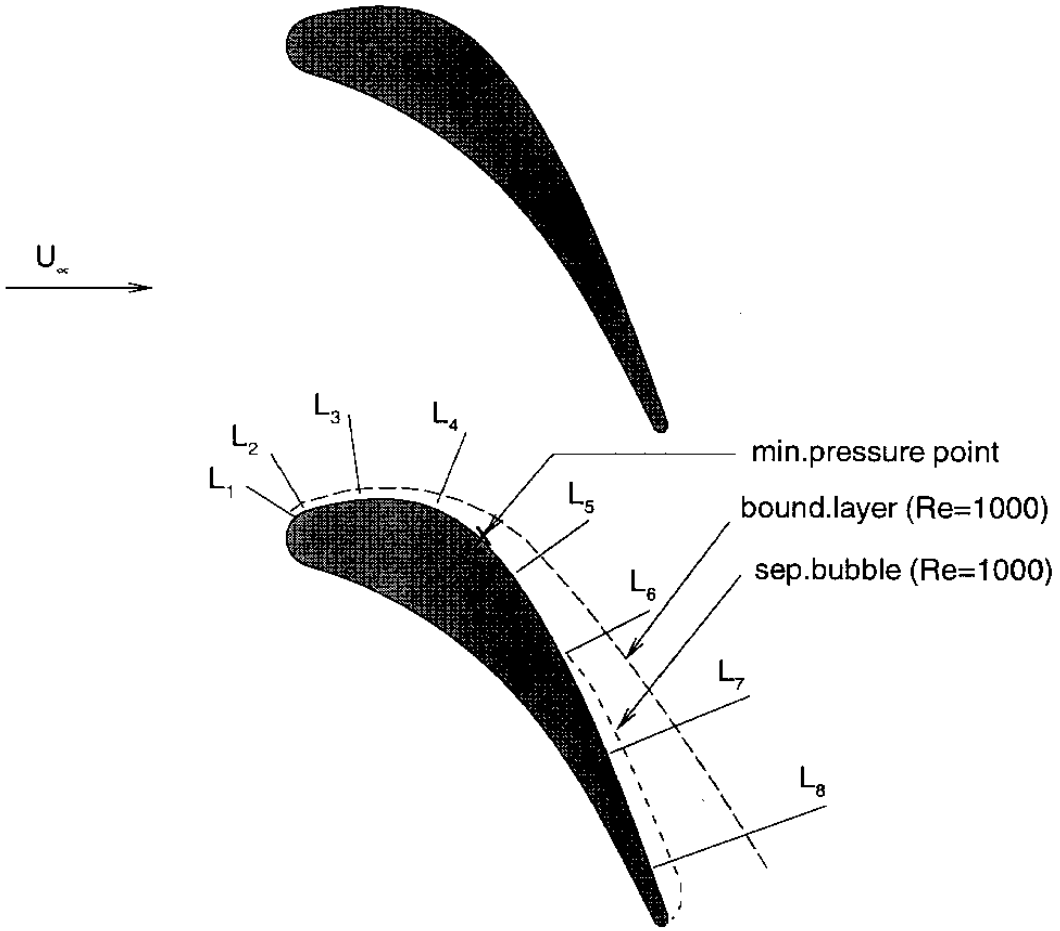

FIGURE 20. Airfoil suction-side perpendicular and parallel stations used to plot transverse and longitudinal distributions of parameter of interest.

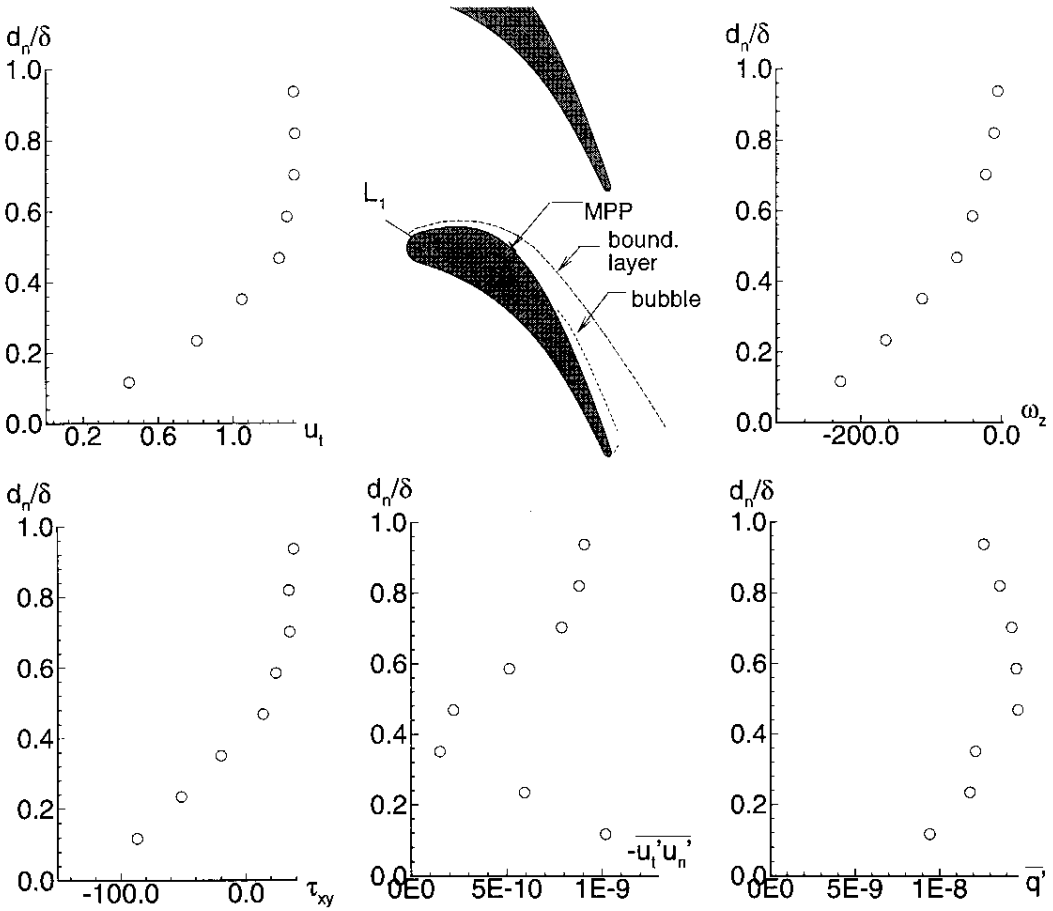

FIGURE 21a. Mean flow characteristics across the boundary layer perpendicular station L1. Basic flow at Re=1000.

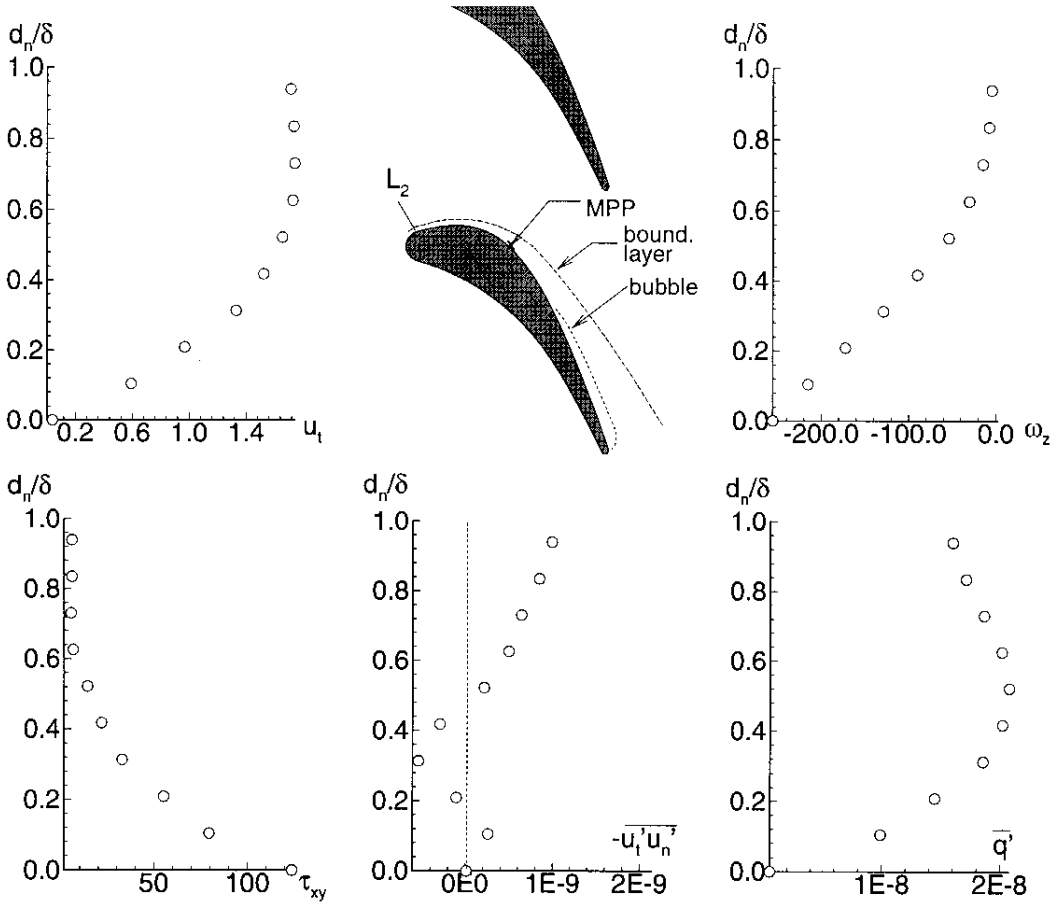

FIGURE 21b. Mean flow characteristics across the boundary layer perpendicular station L2. Basic flow at Re=1000.

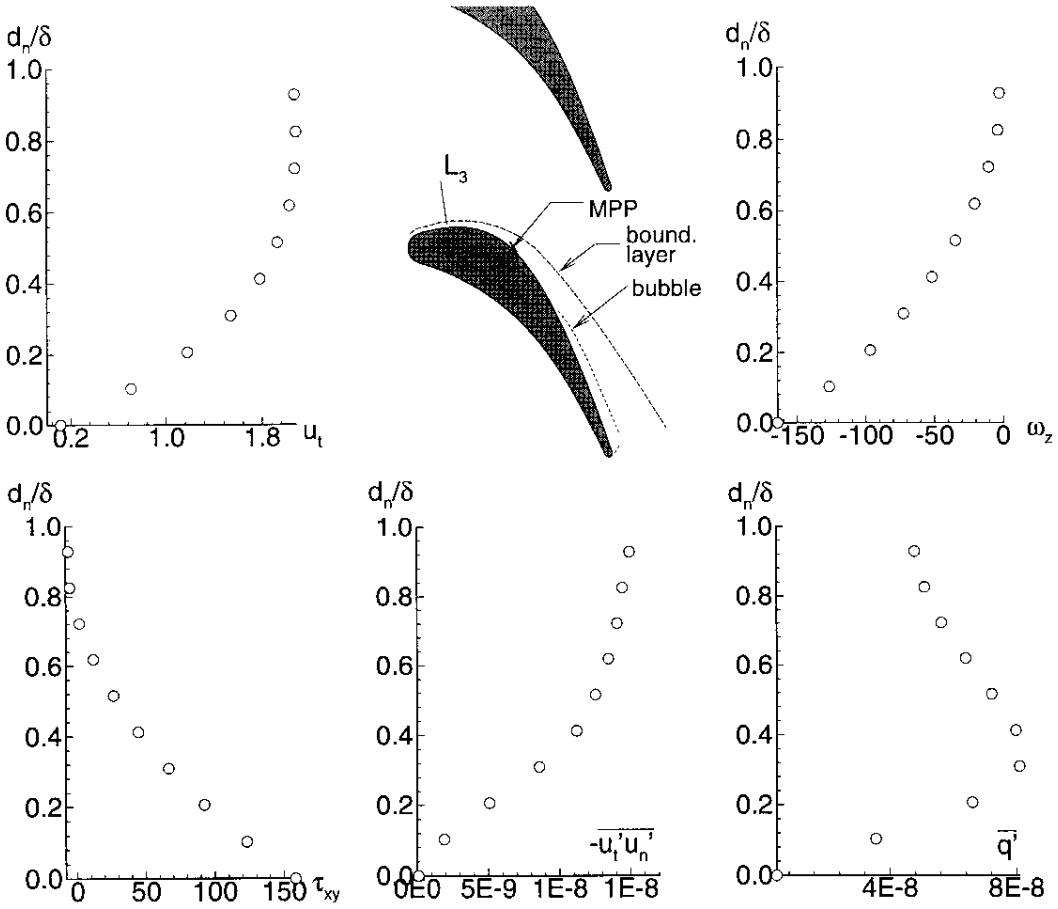

FIGURE 21c. Mean flow characteristics across the boundary layer perpendicular station L3. Basic flow at Re=1000.

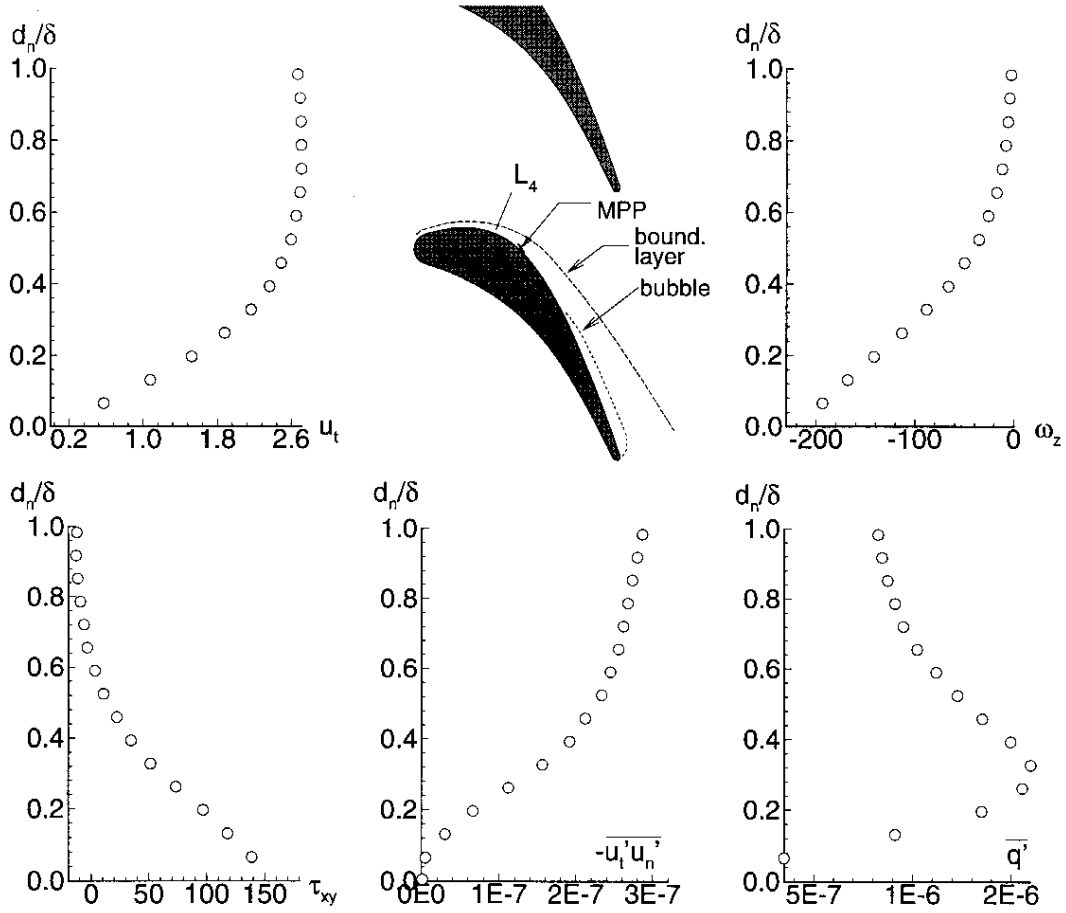

FIGURE 21d. Mean flow characteristics across the boundary layer perpendicular station L4. Basic flow at Re=1000.

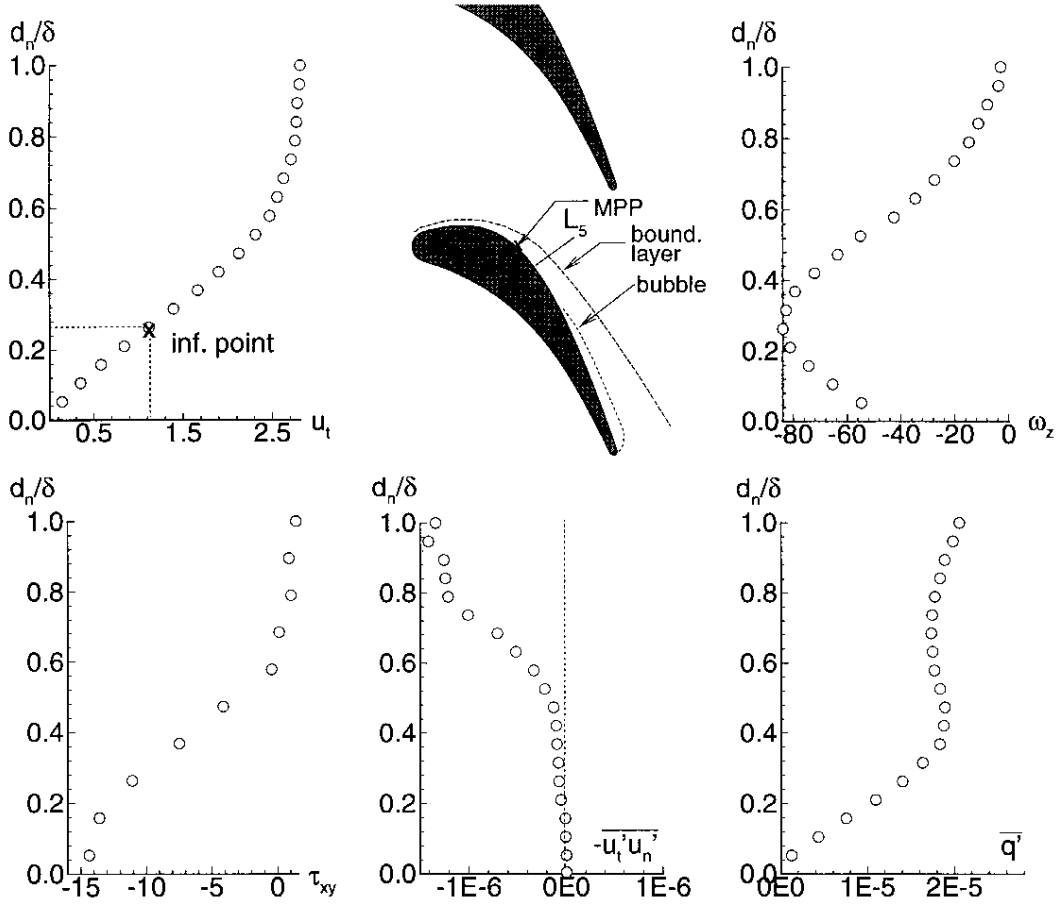

FIGURE 21e. Mean flow characteristics across the boundary layer perpendicular station L5. Basic flow at Re=1000.

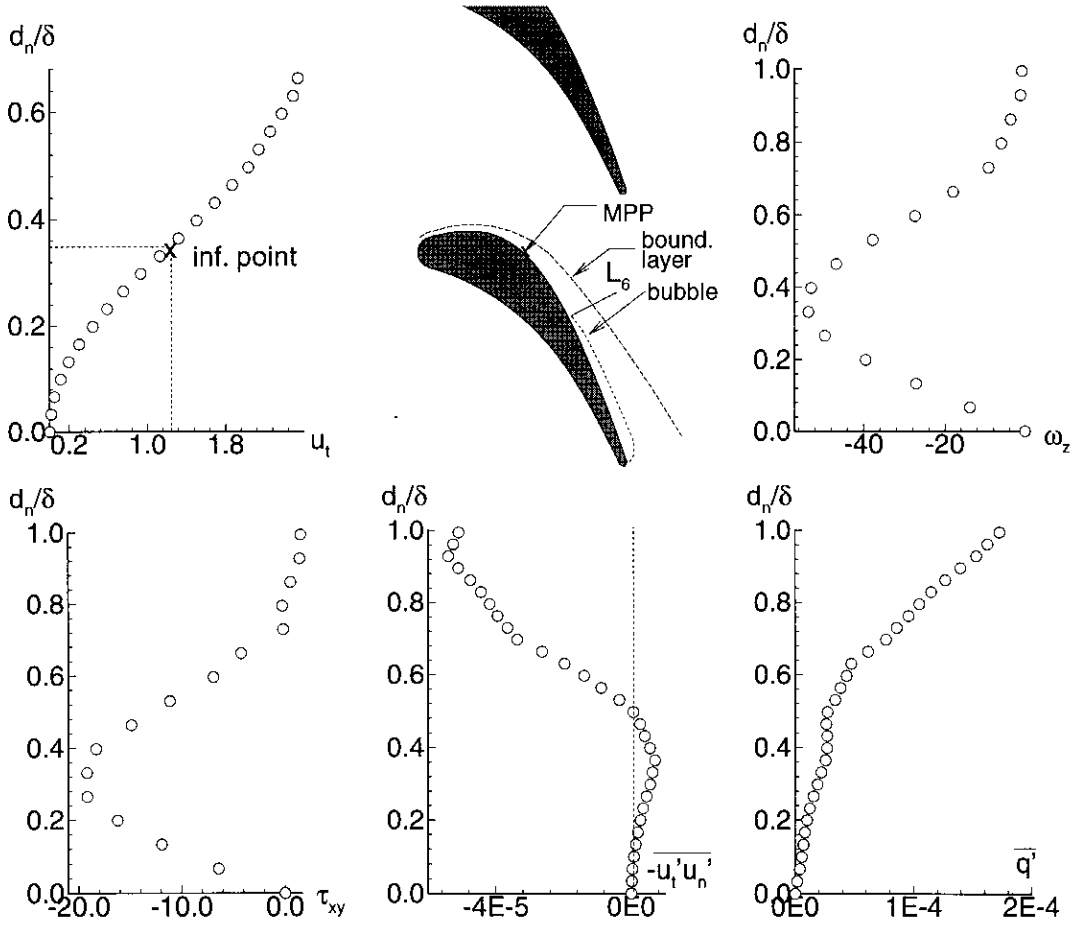

FIGURE 21f. Mean flow characteristics across the boundary layer perpendicular station L6. Basic flow at Re=1000.

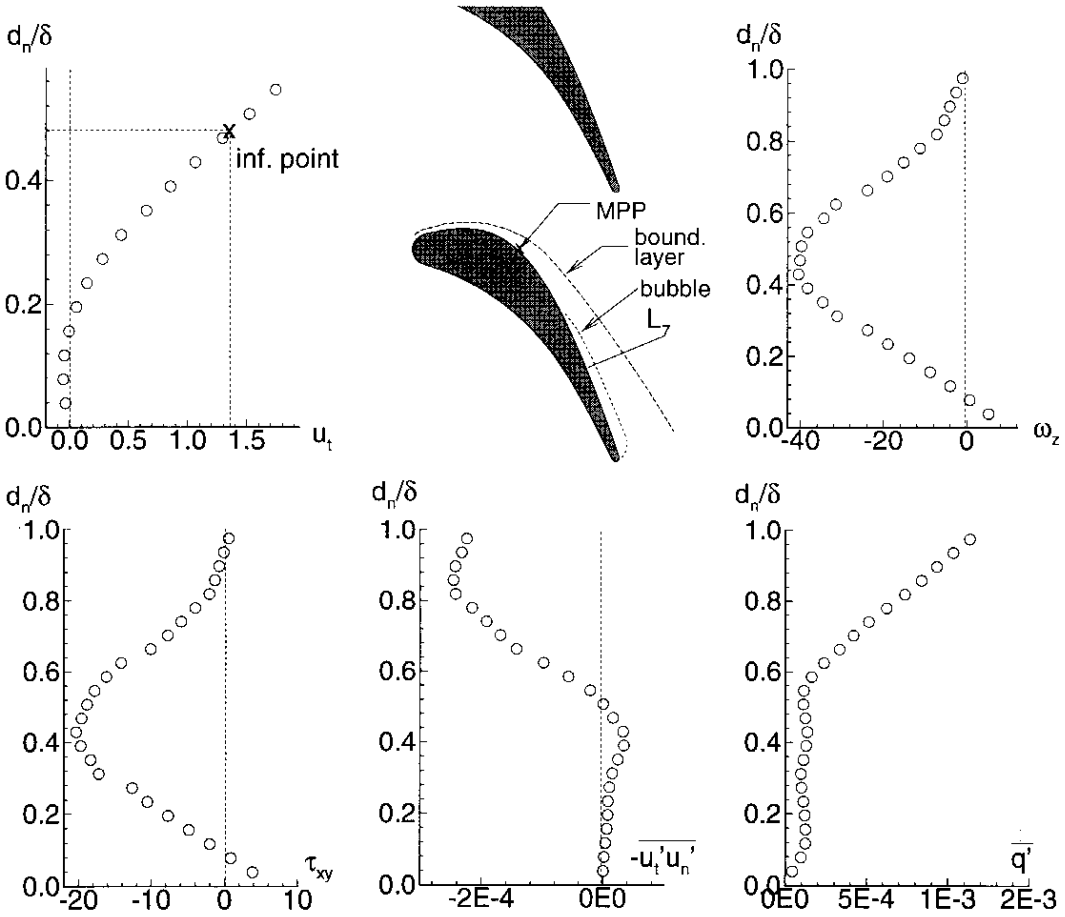

FIGURE 21g. Mean flow characteristics across the boundary layer perpendicular station L7. Basic flow at Re=1000.

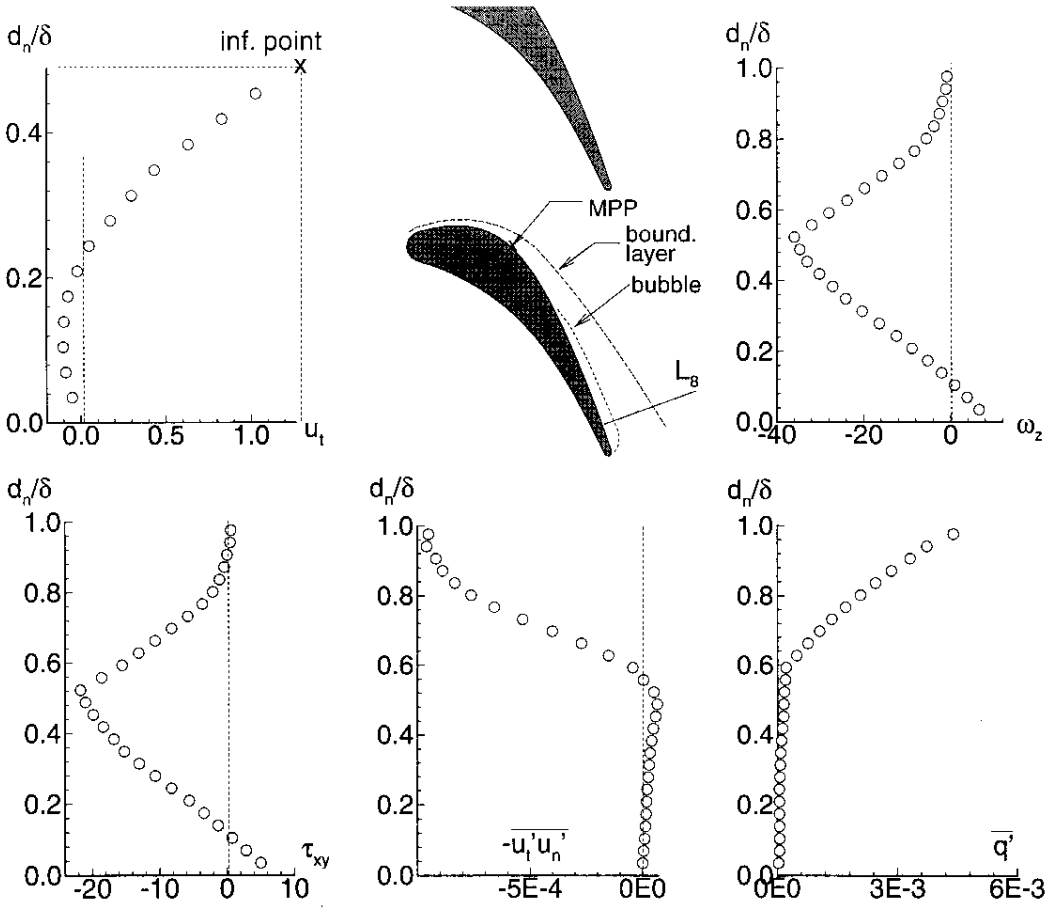

FIGURE 21h. Mean flow characteristics across the boundary layer perpendicular station L8. Basic flow at Re=1000.

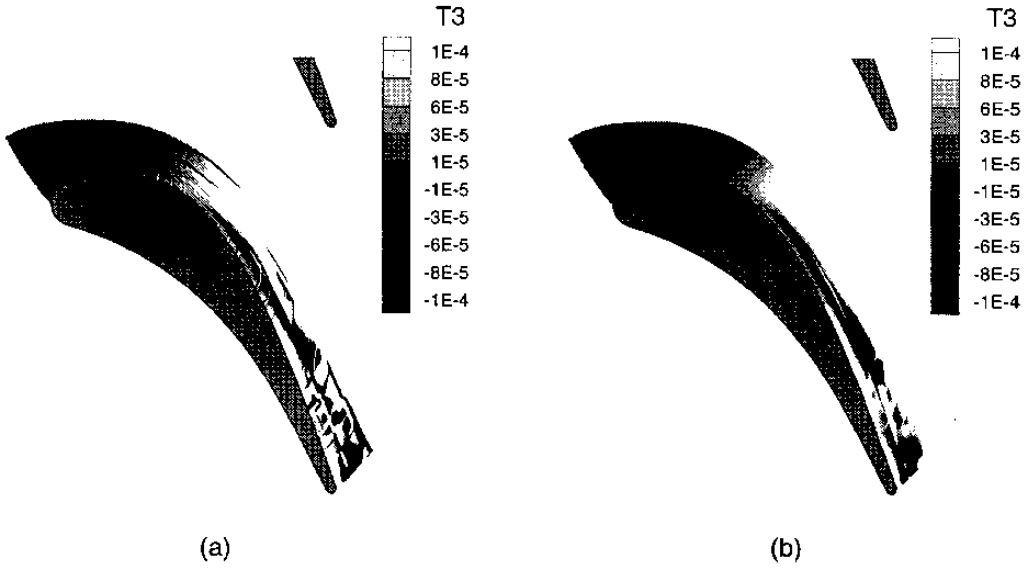

FIGURE 22. Carpet plot of T1* within the airfoil-to-airfoil passage. T1* resulting from the balance of the FKE equation. Basic flow at Re=1000.

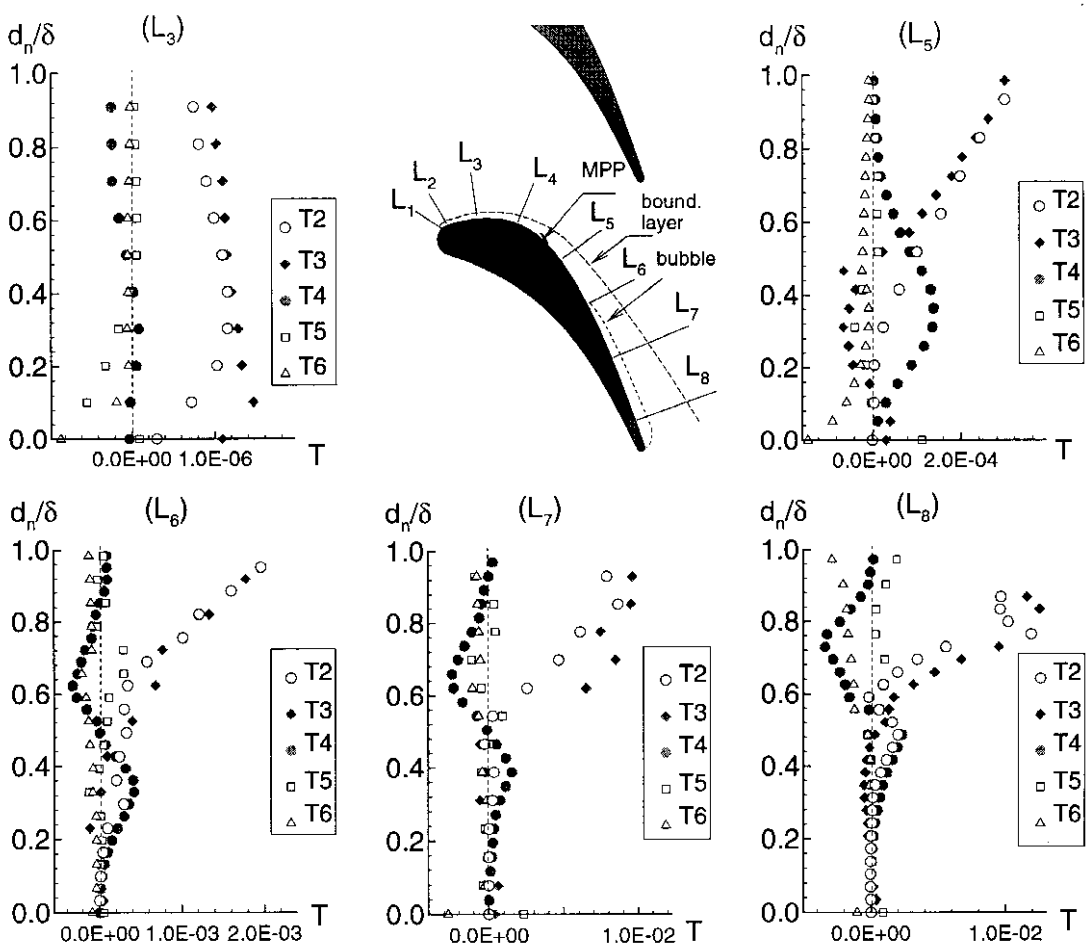

FIGURE 23. FKE budget across the boundary layer perpendicular stations. Basic flow at Re=1000.

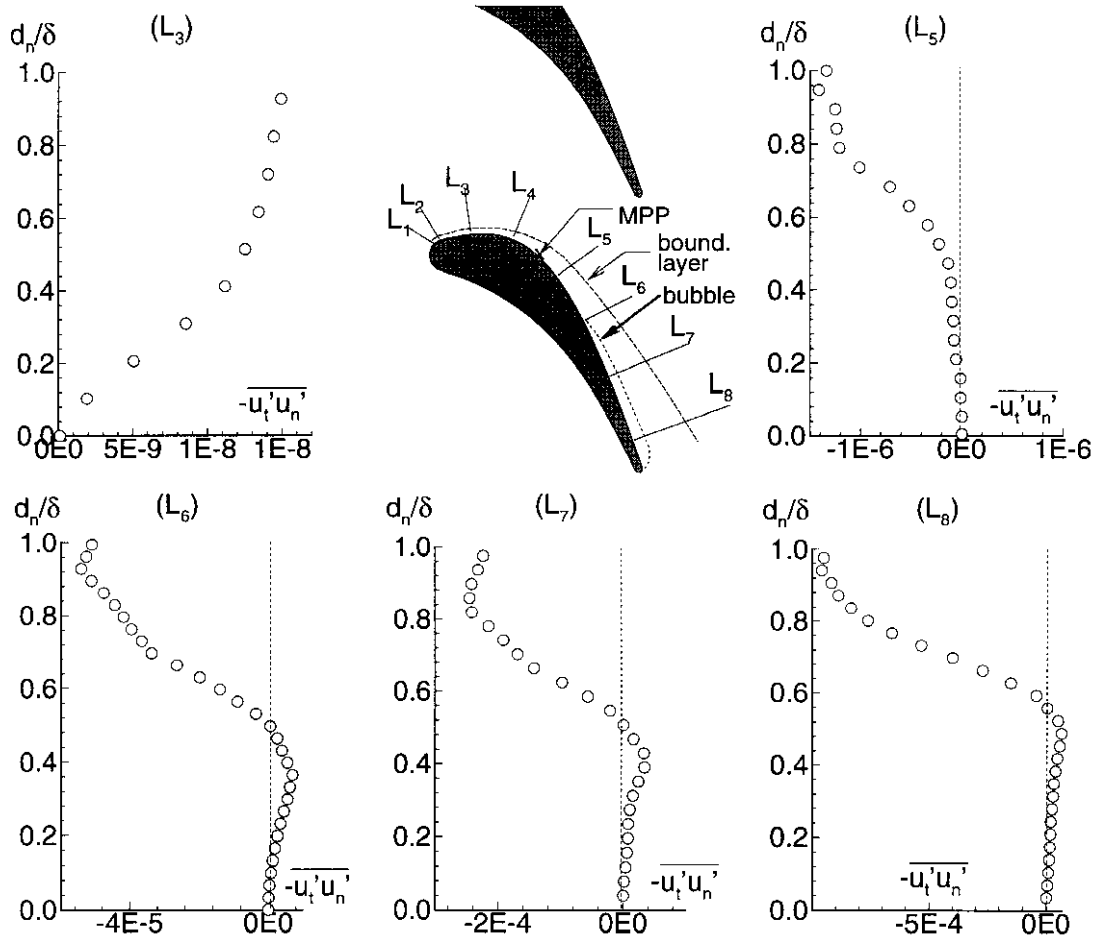

FIGURE 24. Reynolds shear stress $-\overline{u'v'}/U_\infty^2$ distribution across the boundary layer perpendicular stations. Basic flow at Re=1000.

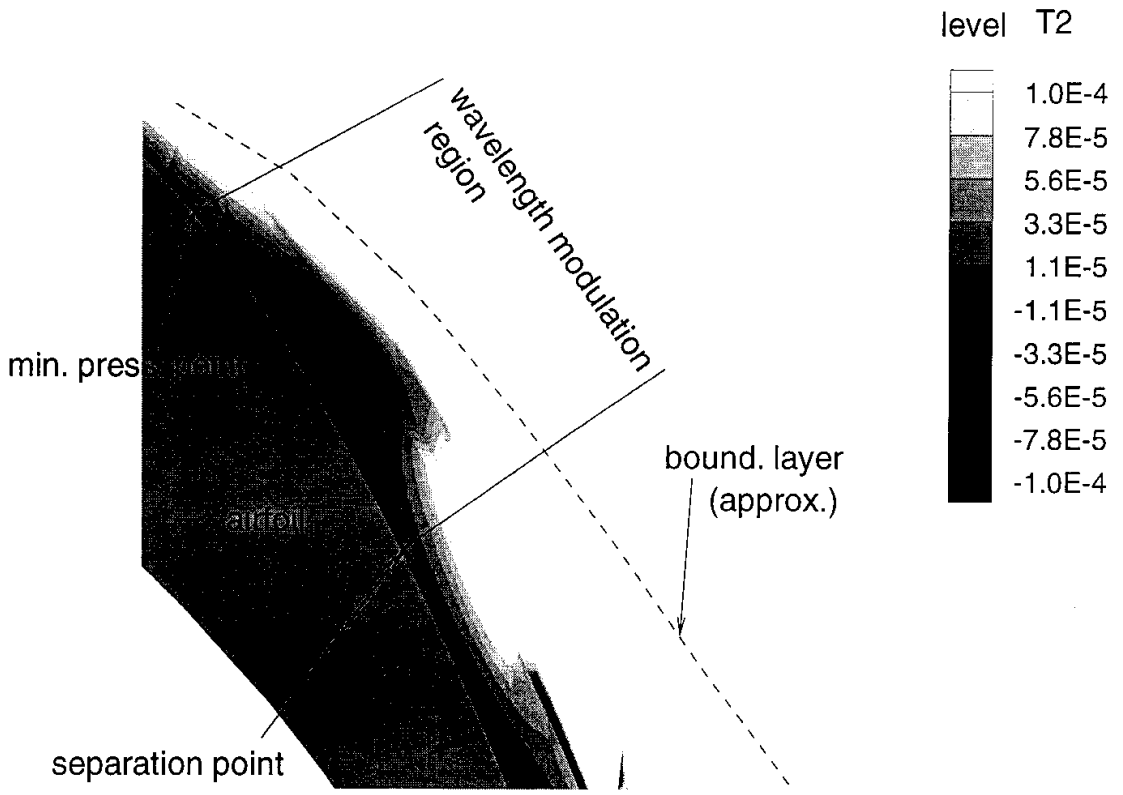

FIGURE 25a. Carpet plots of FKE term T2 within strip enclosing the region where T-S waves generate. Basic flow at Re=1000.

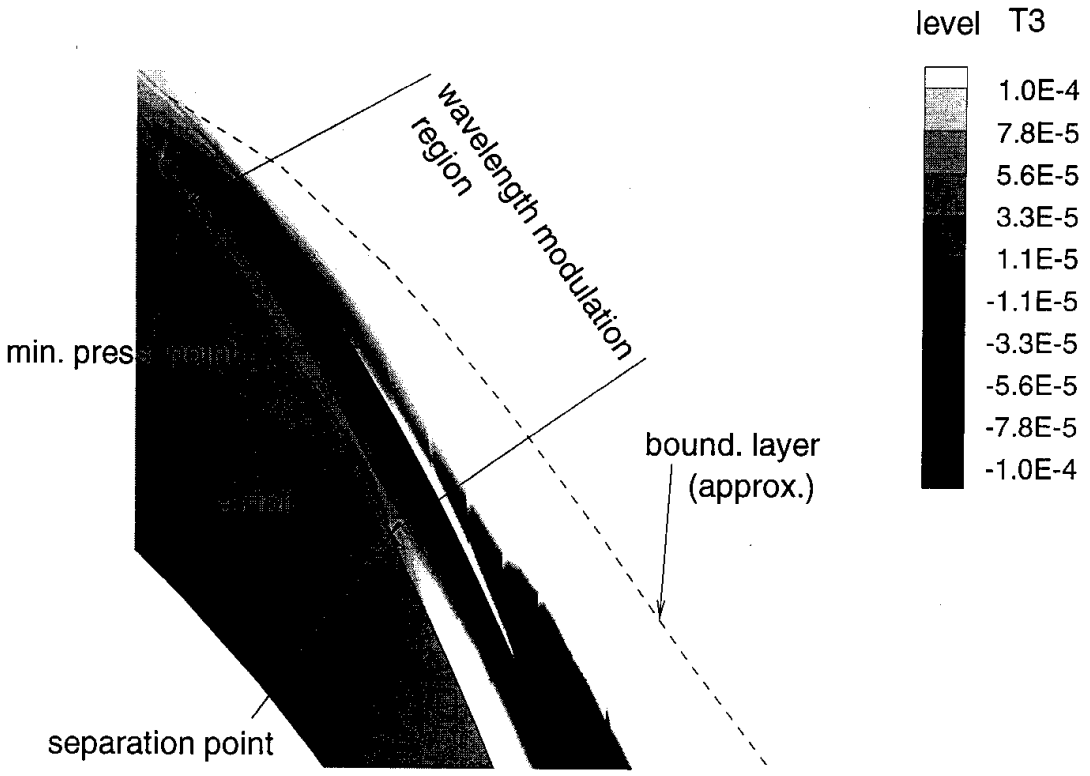

FIGURE 25b. Carpet plots of FKE term T3 within strip enclosing the region where T-S waves generate. Basic flow at Re=1000.

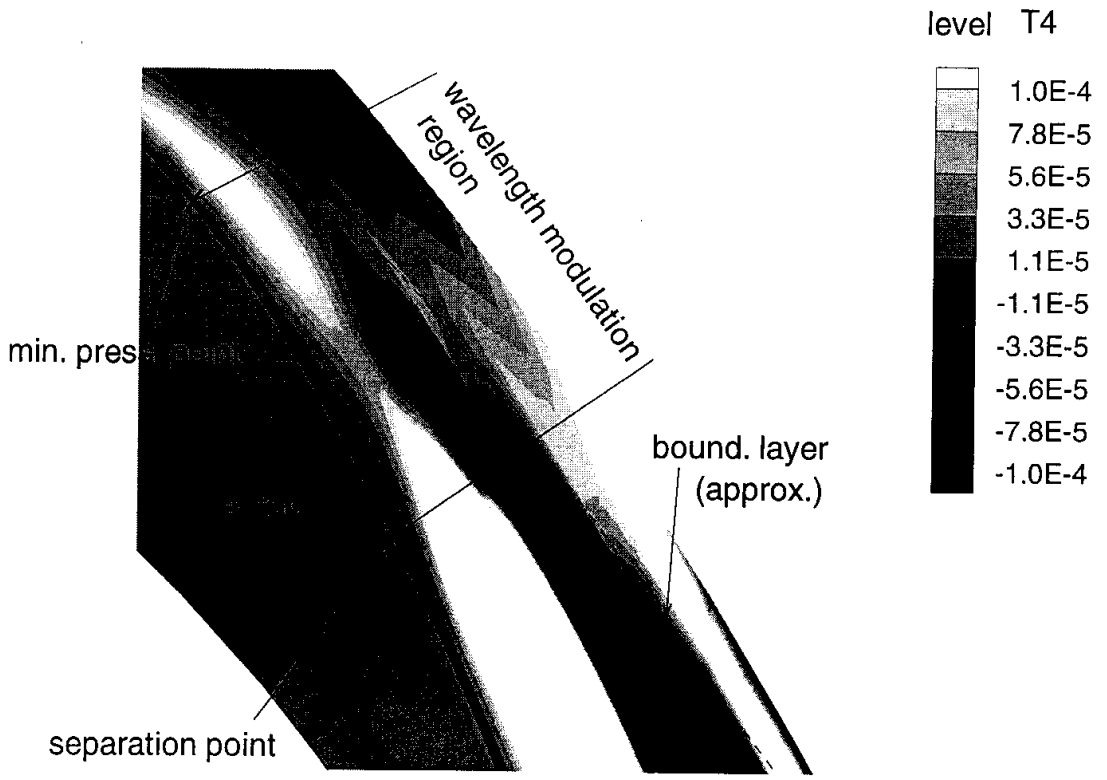

FIGURE 25c. Carpet plots of FKE term T4 within strip enclosing the region where T-S waves generate. Basic flow at Re=1000.

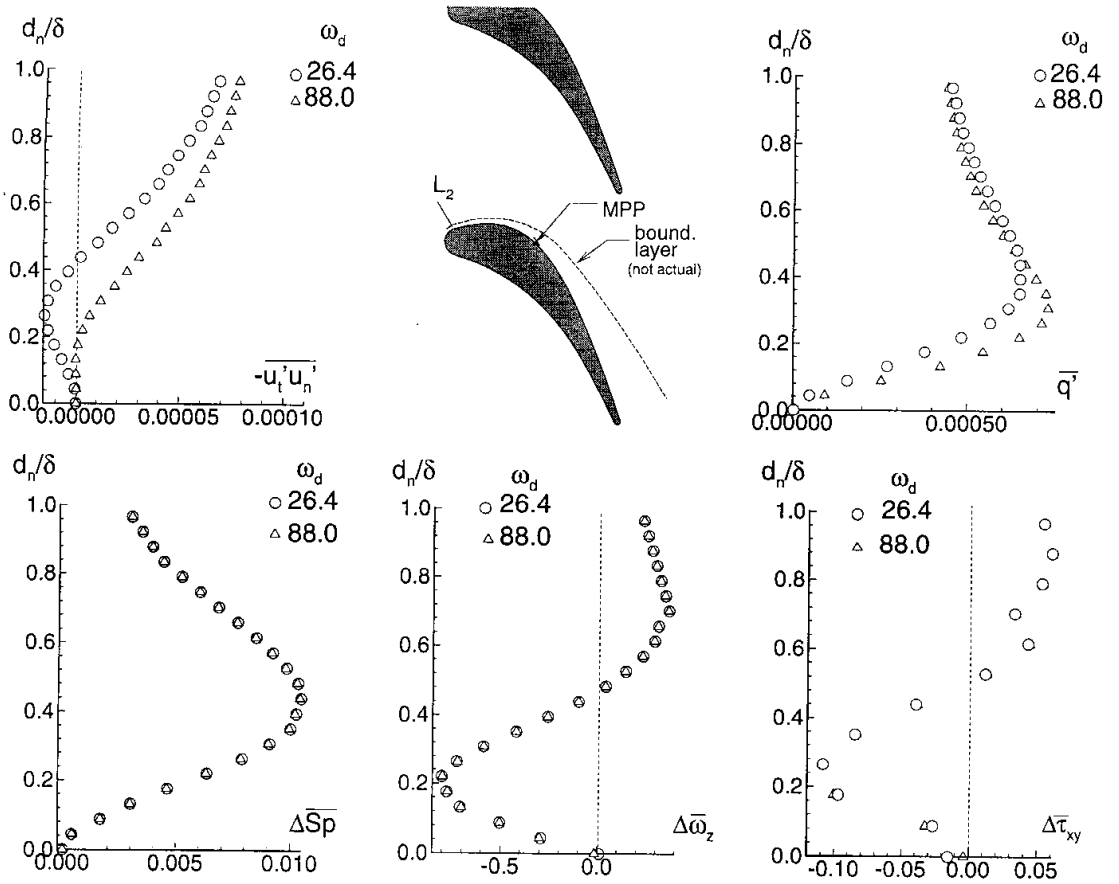

FIGURE 26a. Changes in the mean flow, measured across the boundary layer perpendicular station L2. Subcritical perturbed flow at Re=231 and ε=0.02. (a) ω_d=26.4; (b) ω_d=88.0.

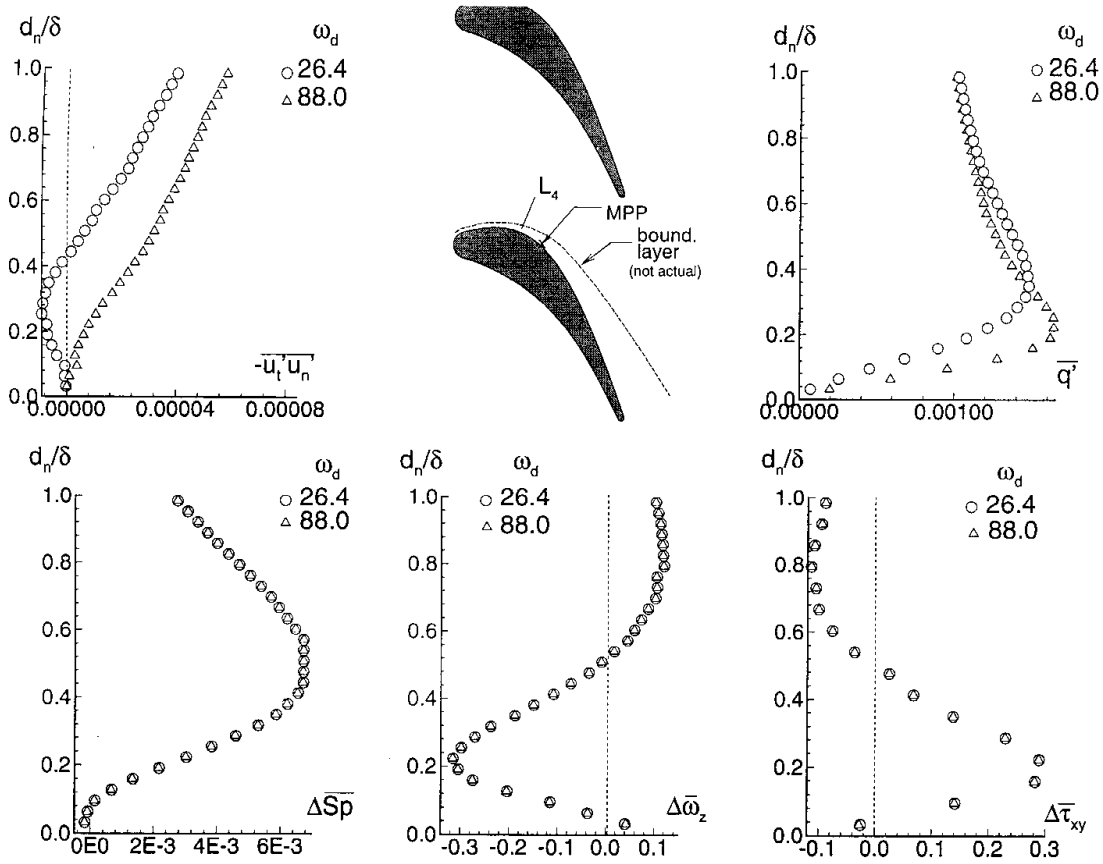

FIGURE 26b. Changes in the mean flow, measured across the boundary layer perpendicular station L4. Subcritical perturbed flow at Re=231 and ε=0.02. (a) ω_d=26.4; (b) ω_d=88.0.

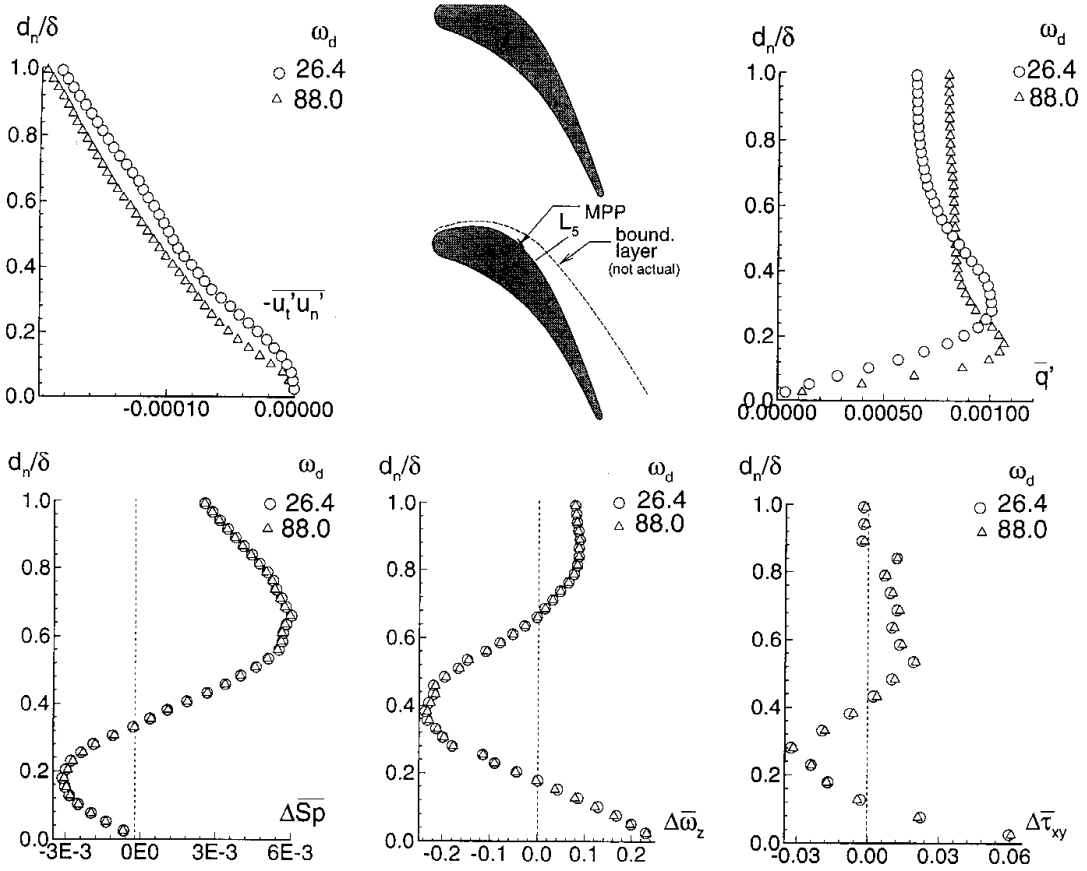

FIGURE 26c. Changes in the mean flow, measured across the boundary layer perpendicular station L5. Subcritical perturbed flow at Re=231 and ε=0.02. (a) ω_d=26.4; (b) ω_d=88.0.

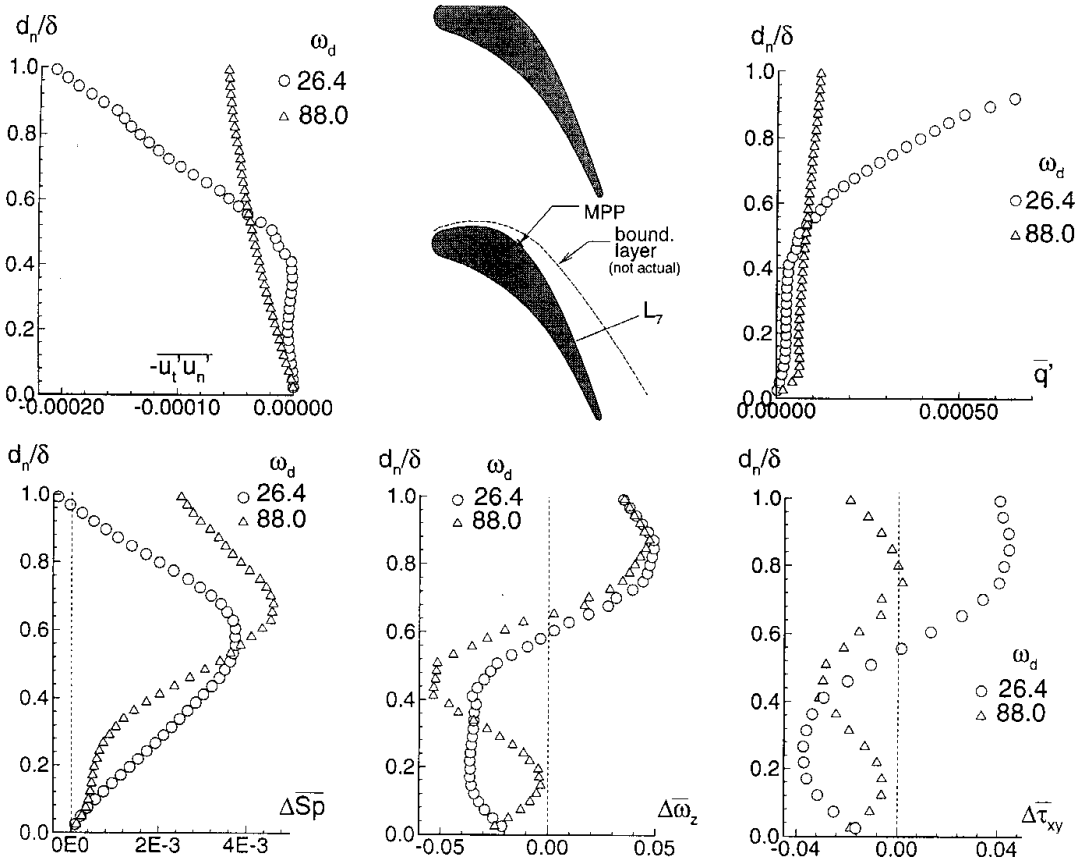

FIGURE 26d. Changes in the mean flow, measured across the boundary layer perpendicular station L7. Subcritical perturbed flow at Re=231 and ε=0.02. (a) ω_d=26.4; (b) ω_d=88.0.

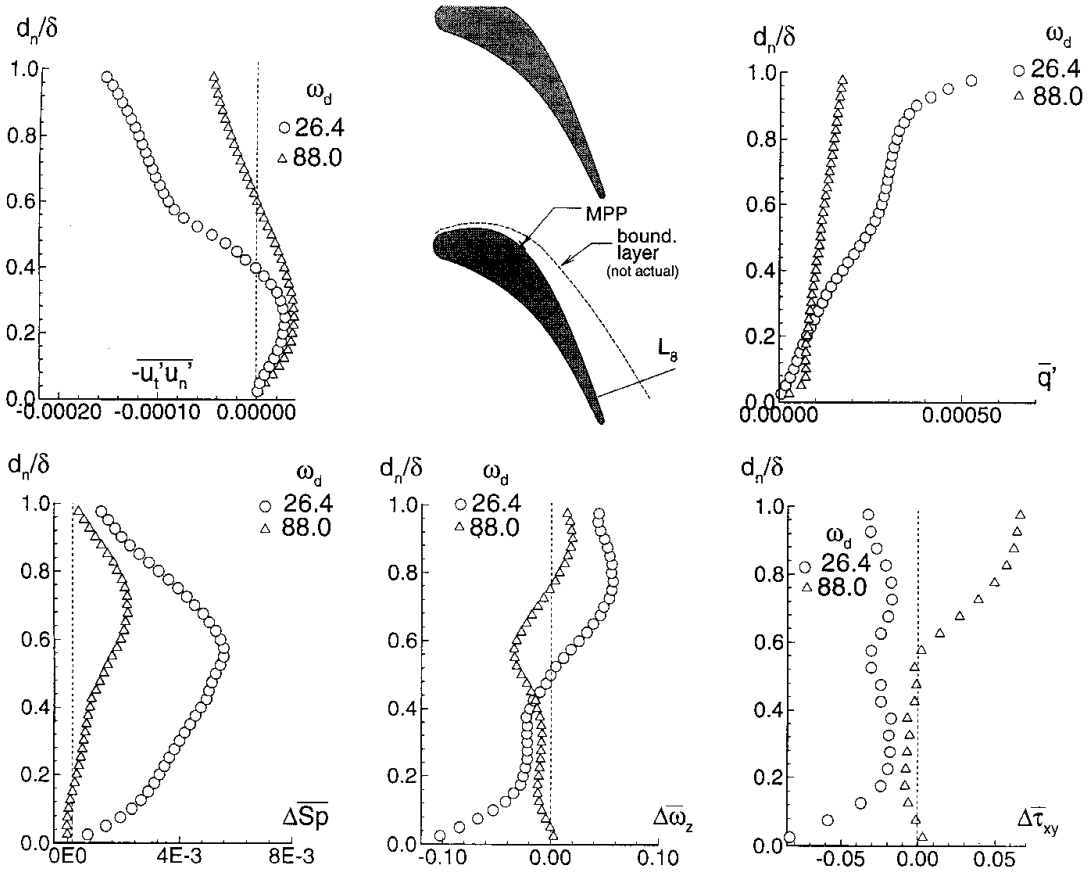

FIGURE 26e. Changes in the mean flow, measured across the boundary layer perpendicular station L8. Subcritical perturbed flow at Re=231 and ε=0.02. (a) ω_d=26.4; (b) ω_d=88.0.

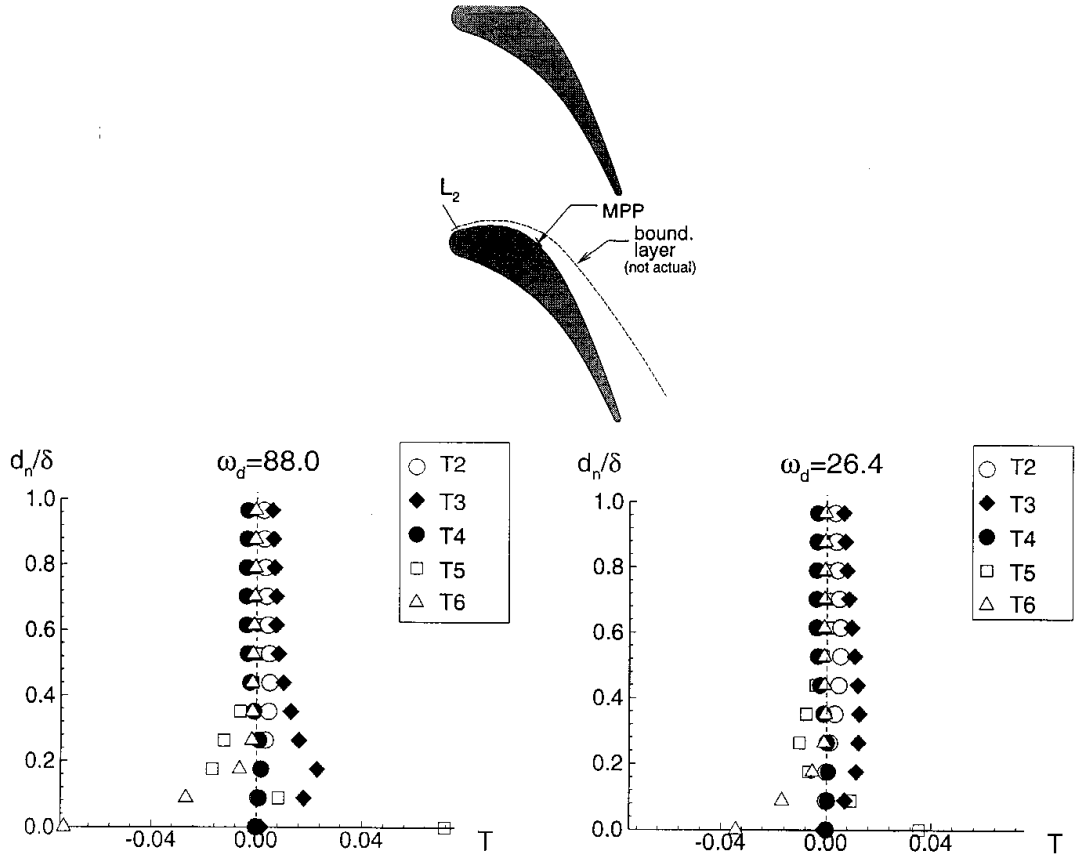

FIGURE 27a. Changes in the FKE terms, measured across the boundary layer perpendicular station L2. Subcritical perturbed flow at Re=231 and ε=0.02. (a) ω_d=26.4; (b) ω_d=88.0.

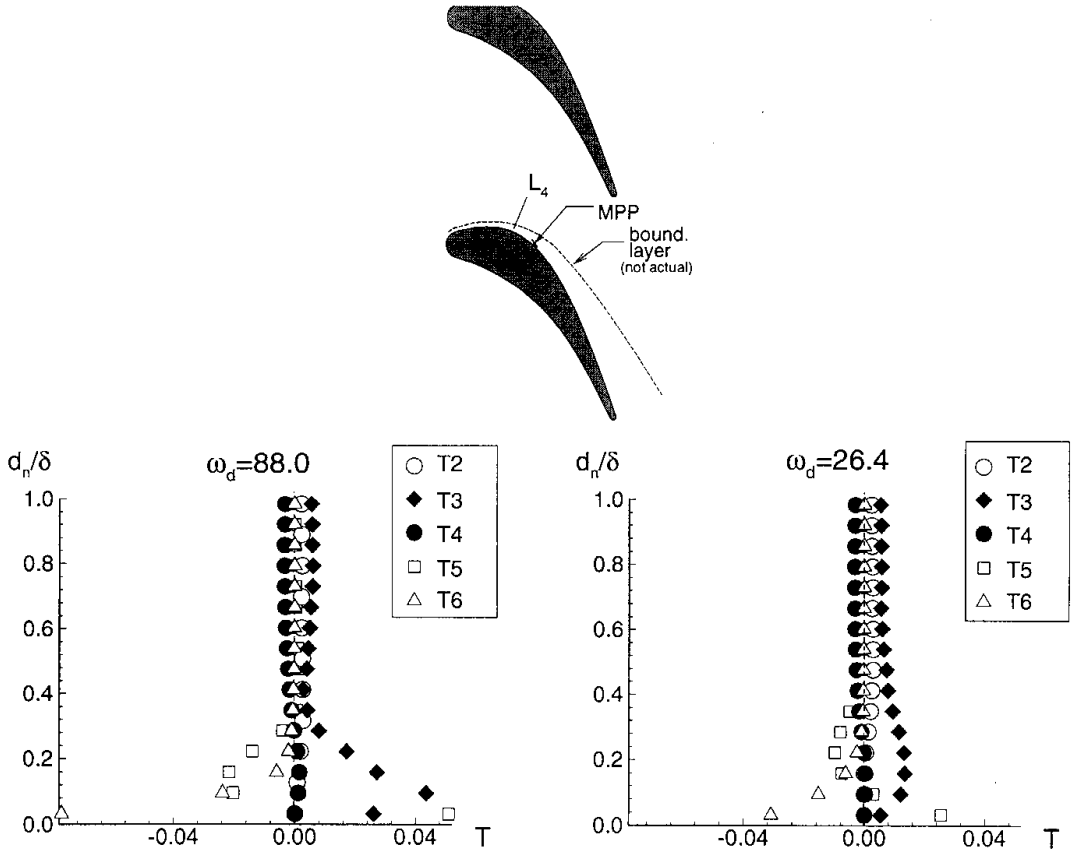

FIGURE 27b. Changes in the FKE terms, measured across the boundary layer perpendicular station L4. Subcritical perturbed flow at Re=231 and ε=0.02. (a) ω_d=26.4; (b) ω_d=88.0.

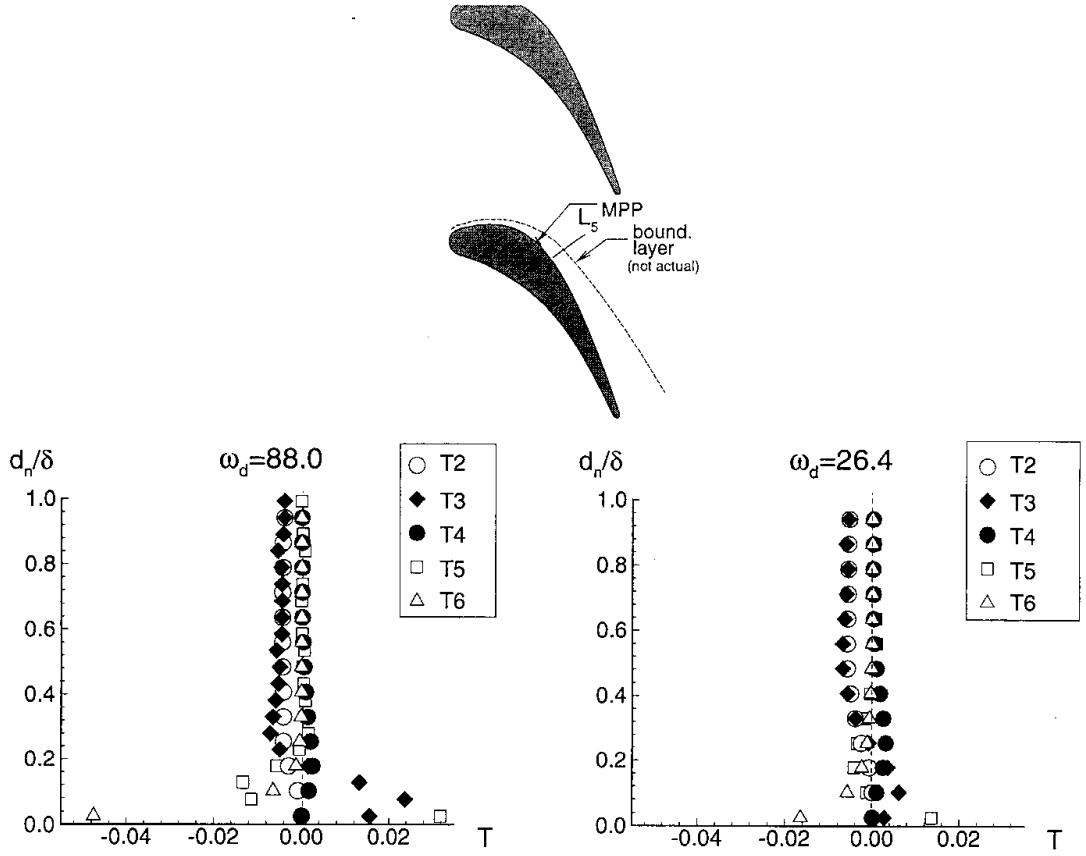

FIGURE 27c. Changes in the FKE terms, measured across the boundary layer perpendicular station L5. Subcritical perturbed flow at Re=231 and ε=0.02. (a) ω_d=26.4; (b) ω_d=88.0.

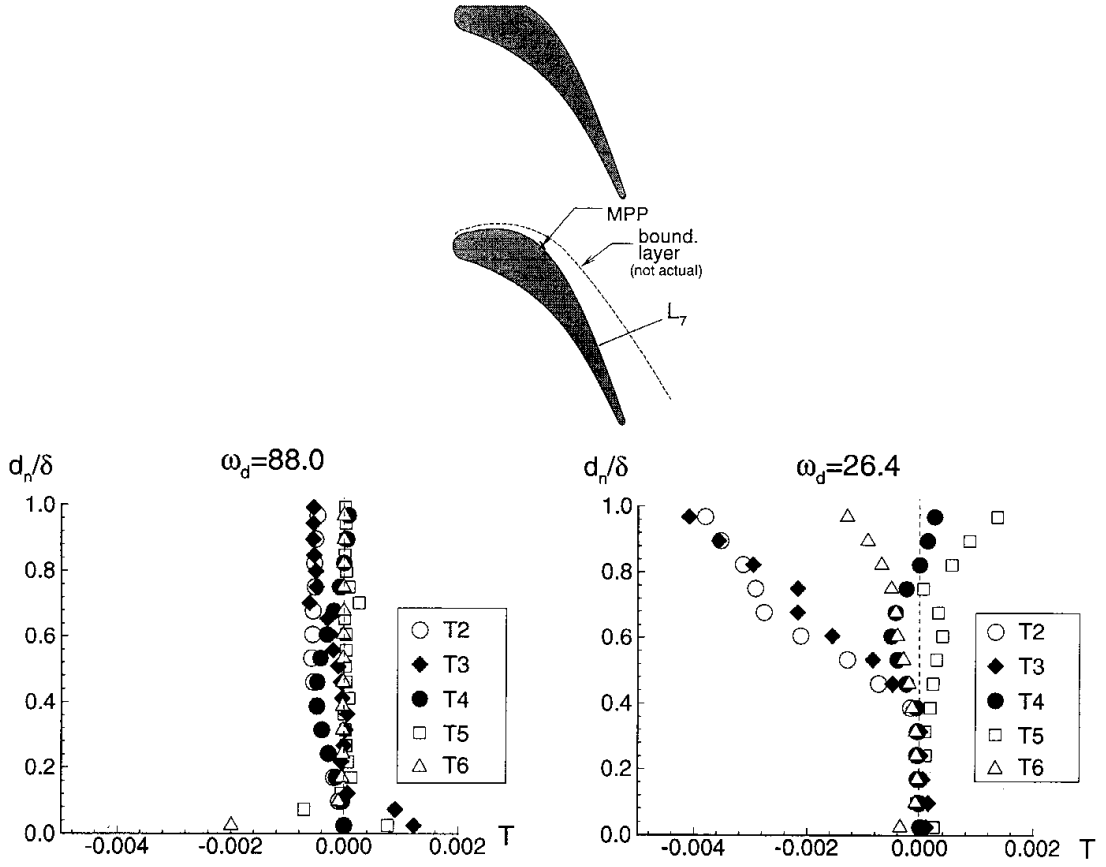

FIGURE 27d. Changes in the FKE terms, measured across the boundary layer perpendicular station L7. Subcritical perturbed flow at Re=231 and ε=0.02. (a) ω_d=26.4; (b) ω_d=88.0.

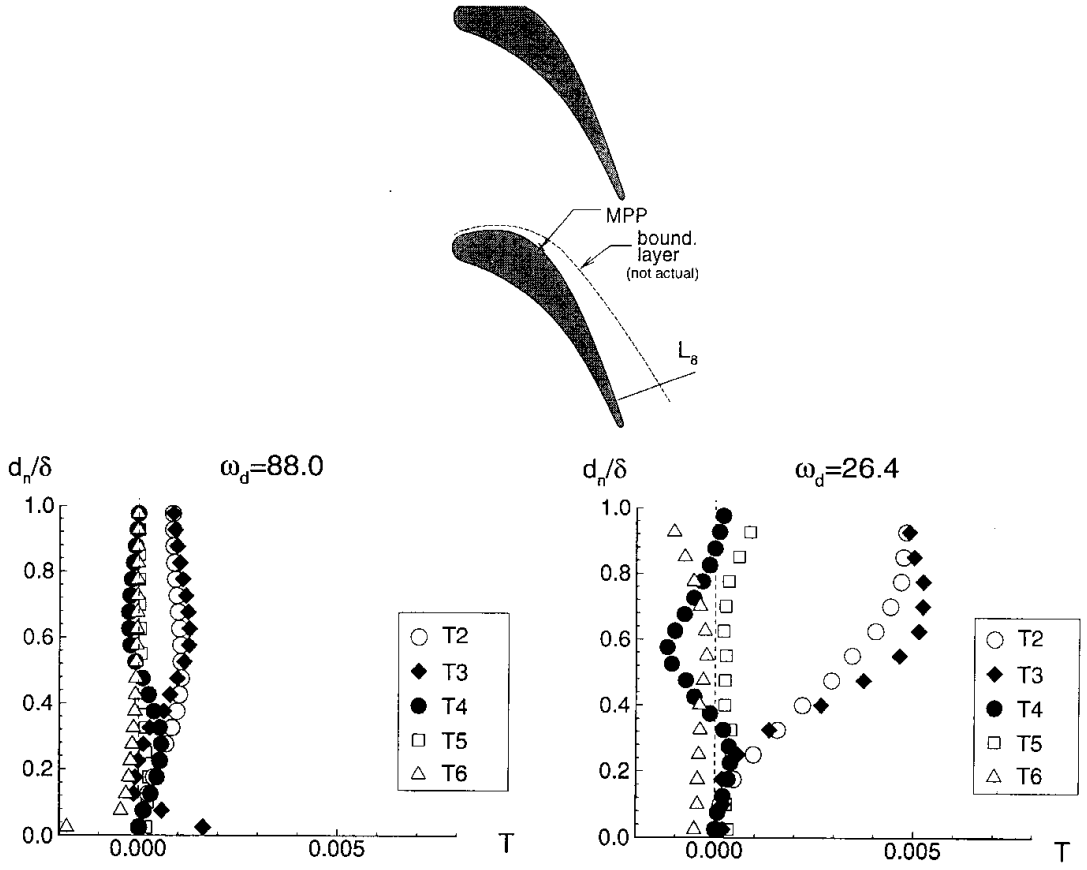

FIGURE 27e. Changes in the FKE terms, measured across the boundary layer perpendicular station L8. Subcritical perturbed flow at Re=231 and ε=0.02. (a) ω_d=26.4; (b) ω_d=88.0.

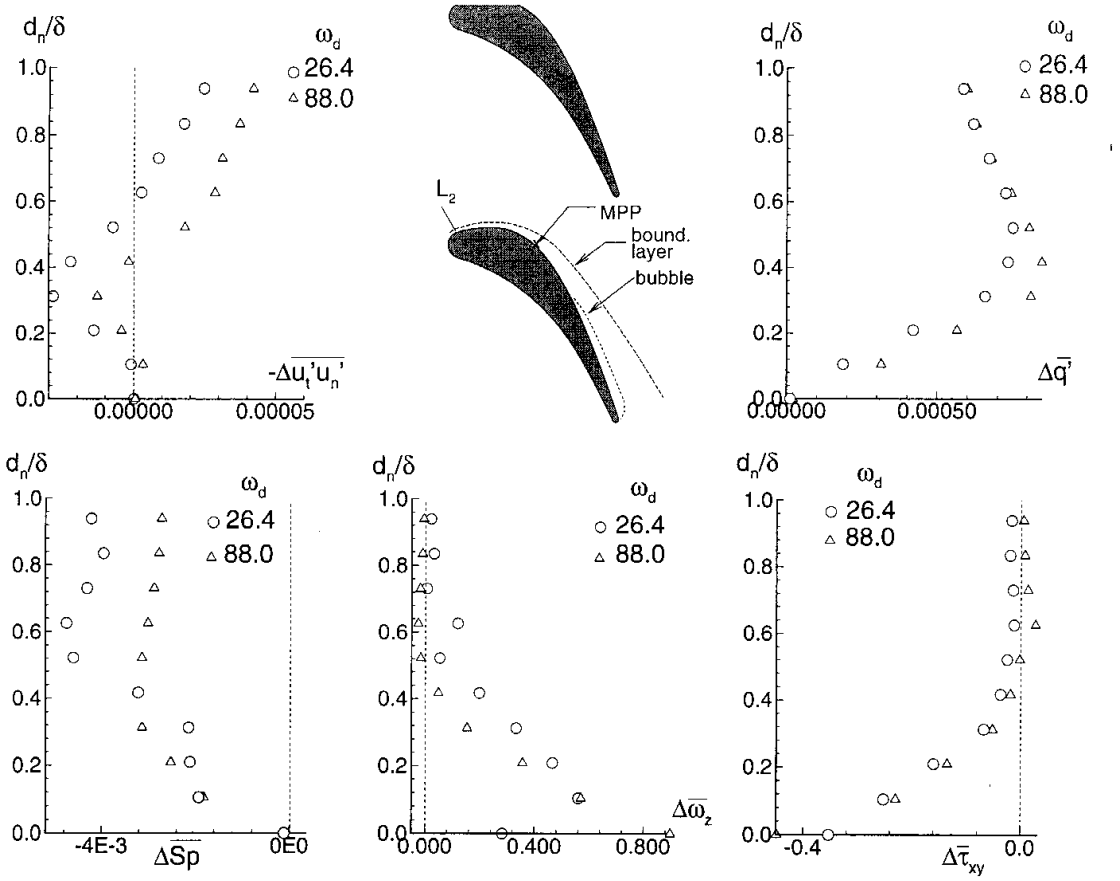

FIGURE 28a. Changes in the mean flow, measured across the boundary layer perpendicular station L2. Supercritical perturbed flow at Re=1000 and ε=0.02. (a) ω_d=26.4; (b) ω_d=88.0.

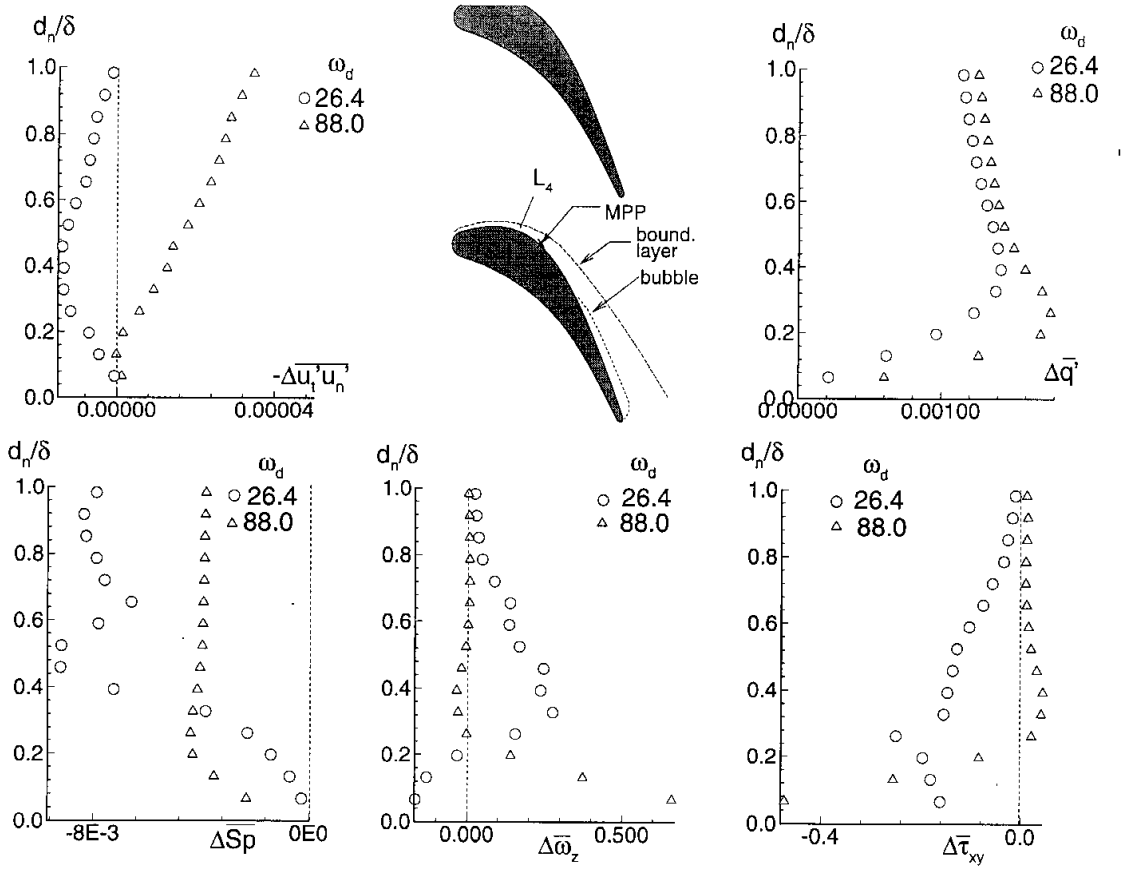

FIGURE 28b. Changes in the mean flow, measured across the boundary layer perpendicular station L4. Supercritical perturbed flow at Re=1000 and ε=0.02. (a) ω_d=26.4; (b) ω_d=88.0.

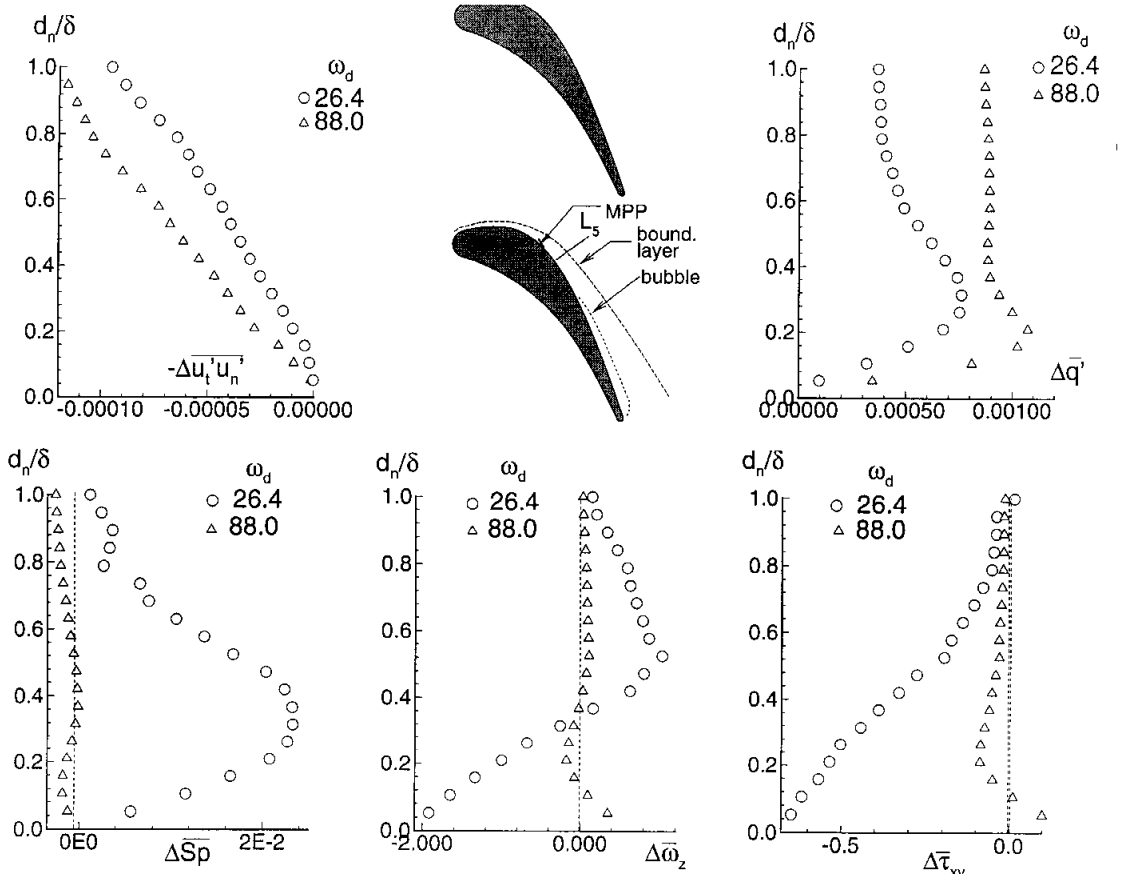

FIGURE 28c. Changes in the mean flow, measured across the boundary layer perpendicular station L5. Supercritical perturbed flow at Re=1000 and ε=0.02. (a) ω_d=26.4; (b) ω_d=88.0.

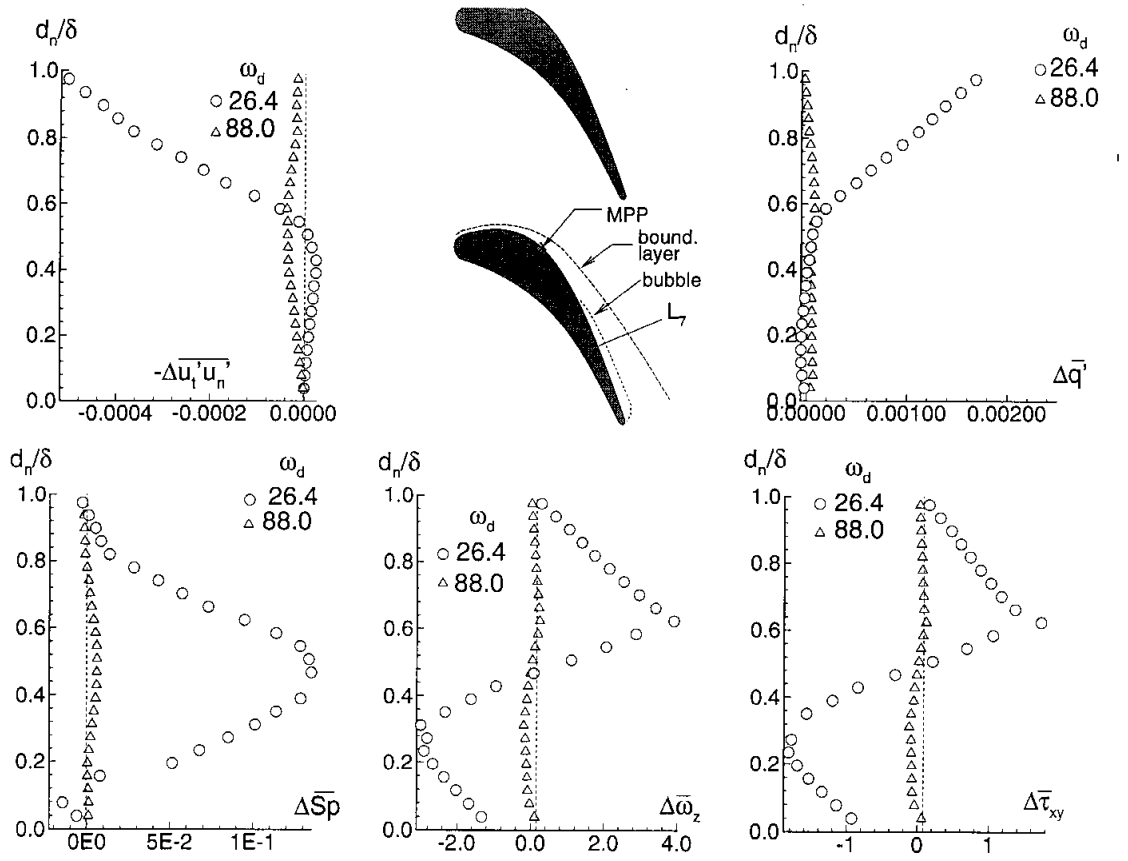

FIGURE 28d. Changes in the mean flow, measured across the boundary layer perpendicular station L7. Supercritical perturbed flow at Re=1000 and ε=0.02. (a) ω_d=26.4; (b) ω_d=88.0.

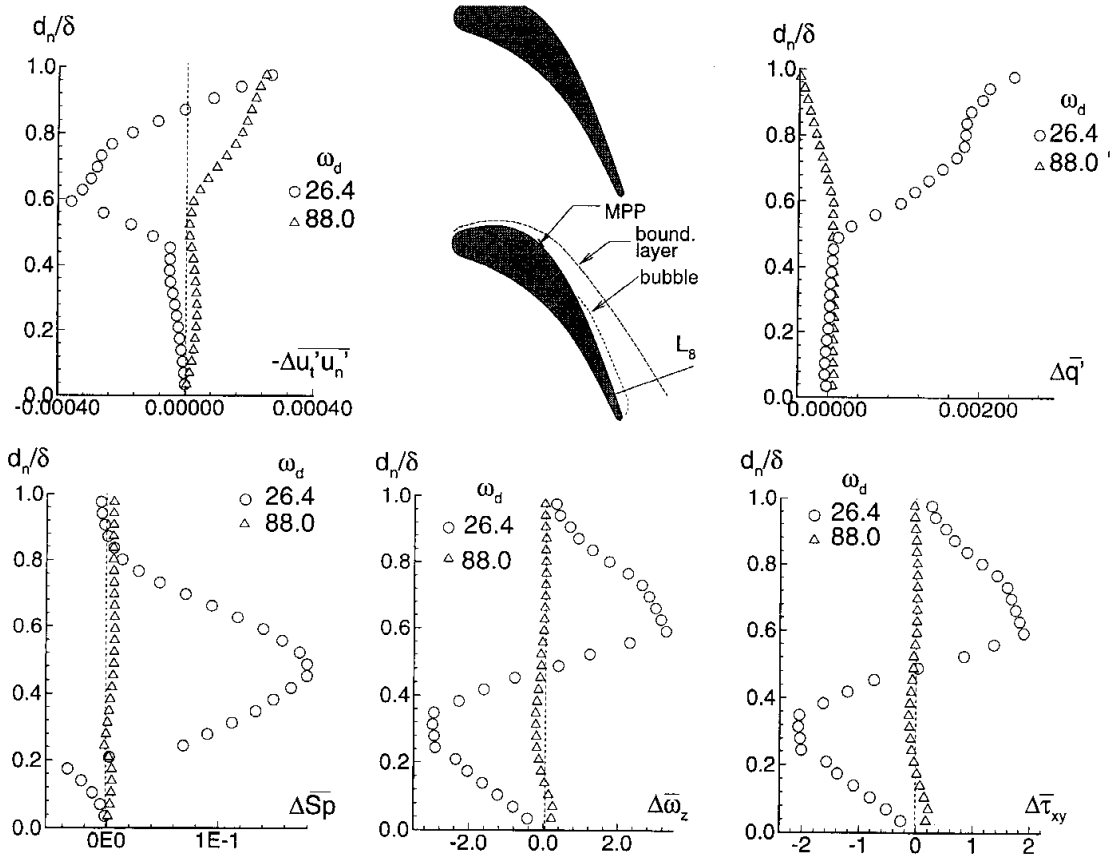

FIGURE 28e. Changes in the mean flow, measured across the boundary layer perpendicular station L8. Supercritical perturbed flow at Re=1000 and ε=0.02. (a) ω_d=26.4; (b) ω_d=88.0.

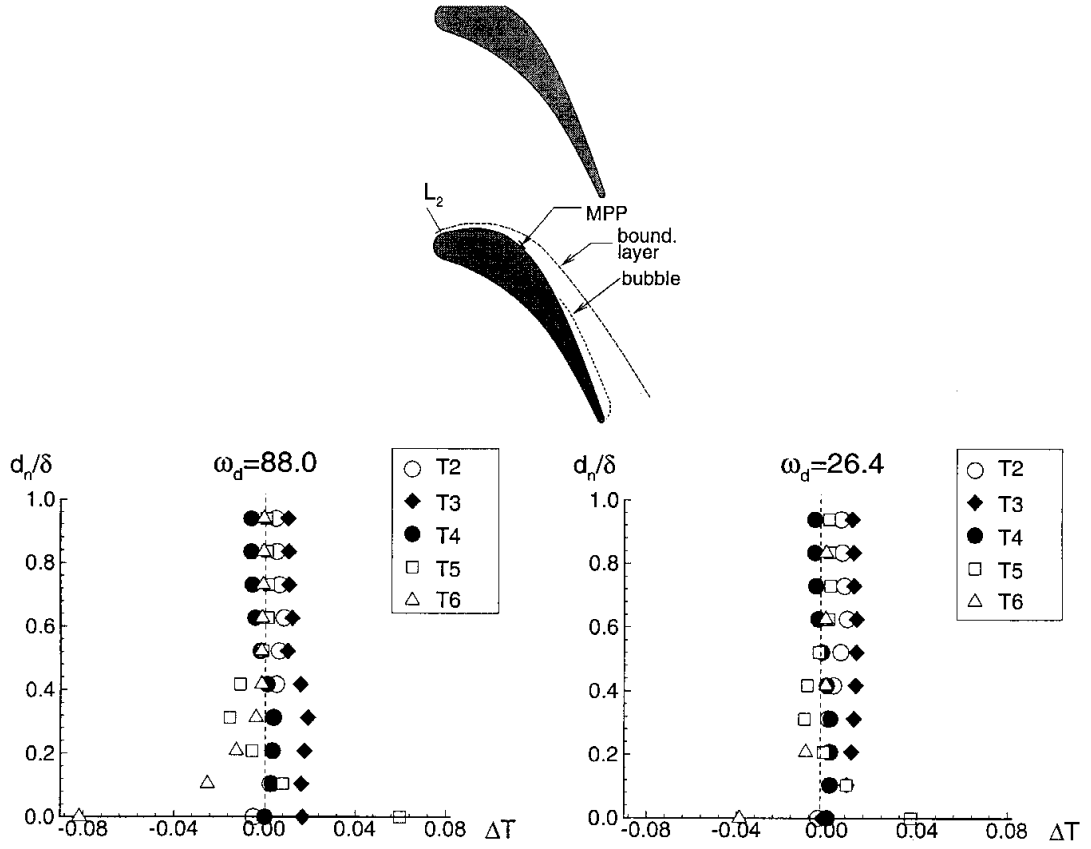

FIGURE 29a. Changes in the FKE terms, measured across the boundary layer perpendicular station L2. Supercritical perturbed flow at Re=1000, ε=0.02, with ω_d=88.0 and ω_d=26.4.

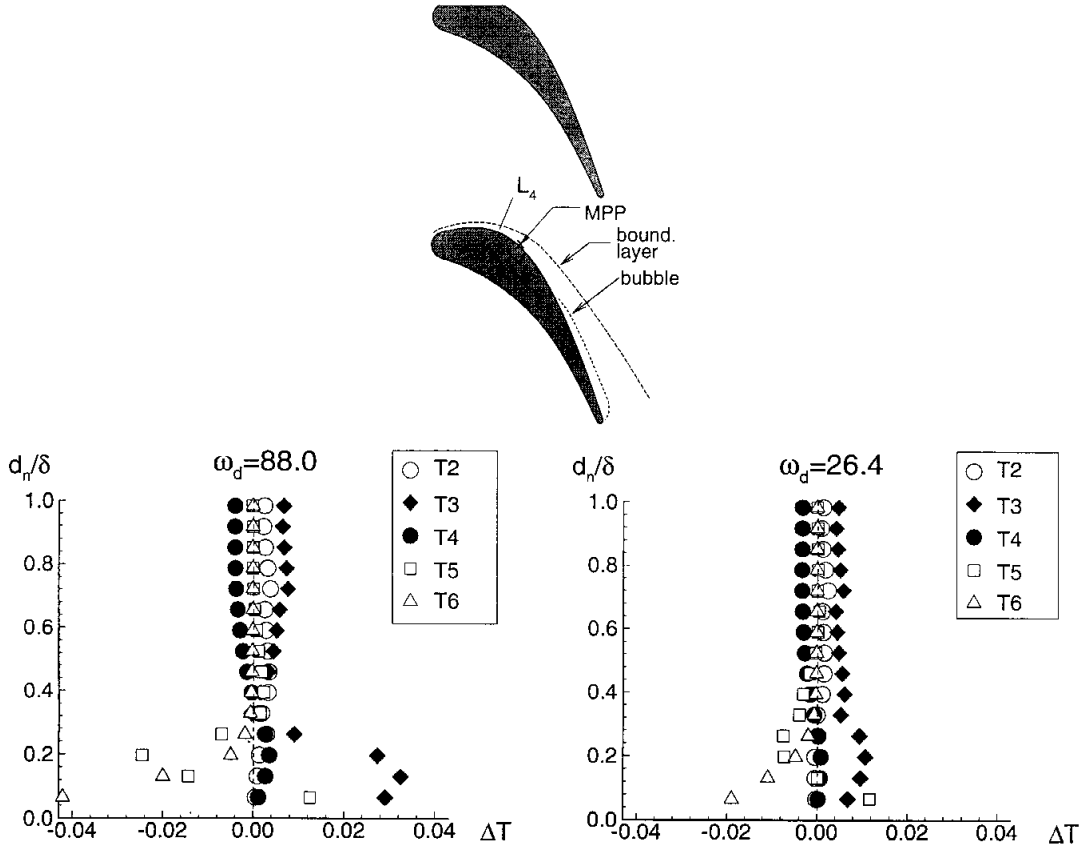

FIGURE 29b. Changes in the FKE terms, measured across the boundary layer perpendicular station L4. Supercritical perturbed flow at Re=1000, ε=0.02, with ω_d=88.0 and ω_d=26.4.

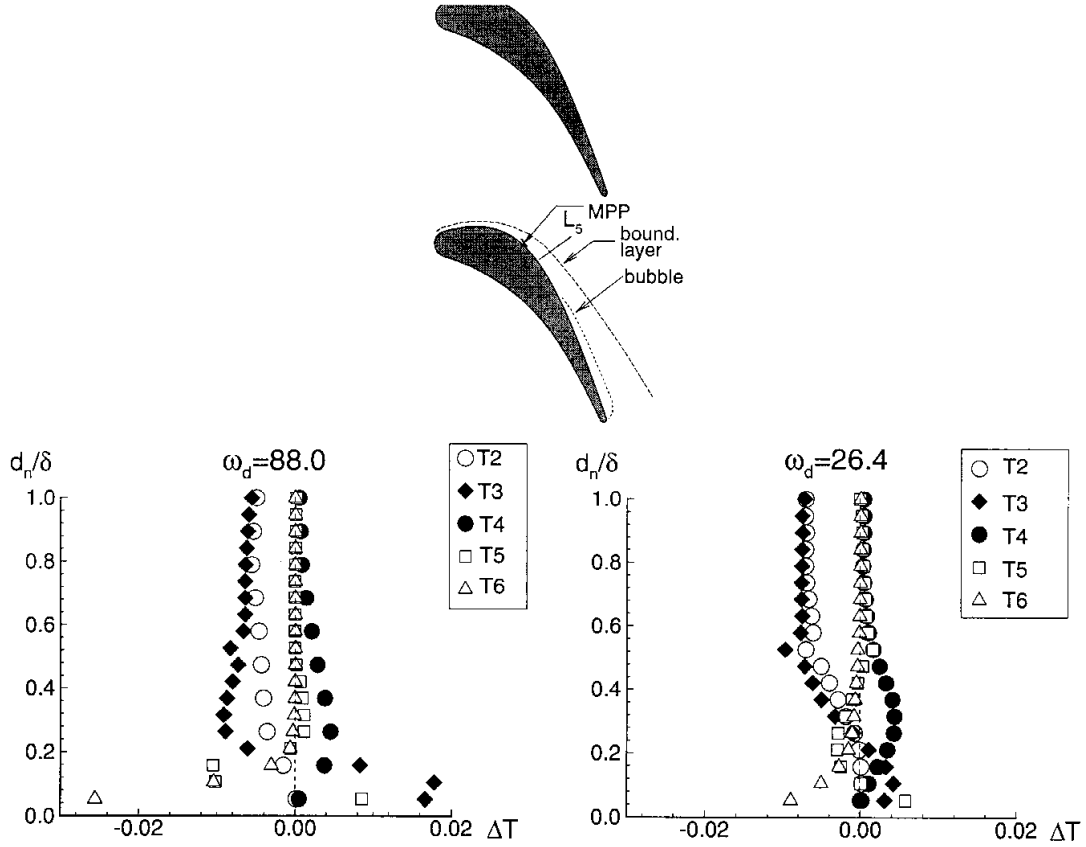

FIGURE 29c. Changes in the FKE terms, measured across the boundary layer perpendicular station L5. Supercritical perturbed flow at Re=1000, ε=0.02, with ω_d=88.0 and ω_d=26.4.

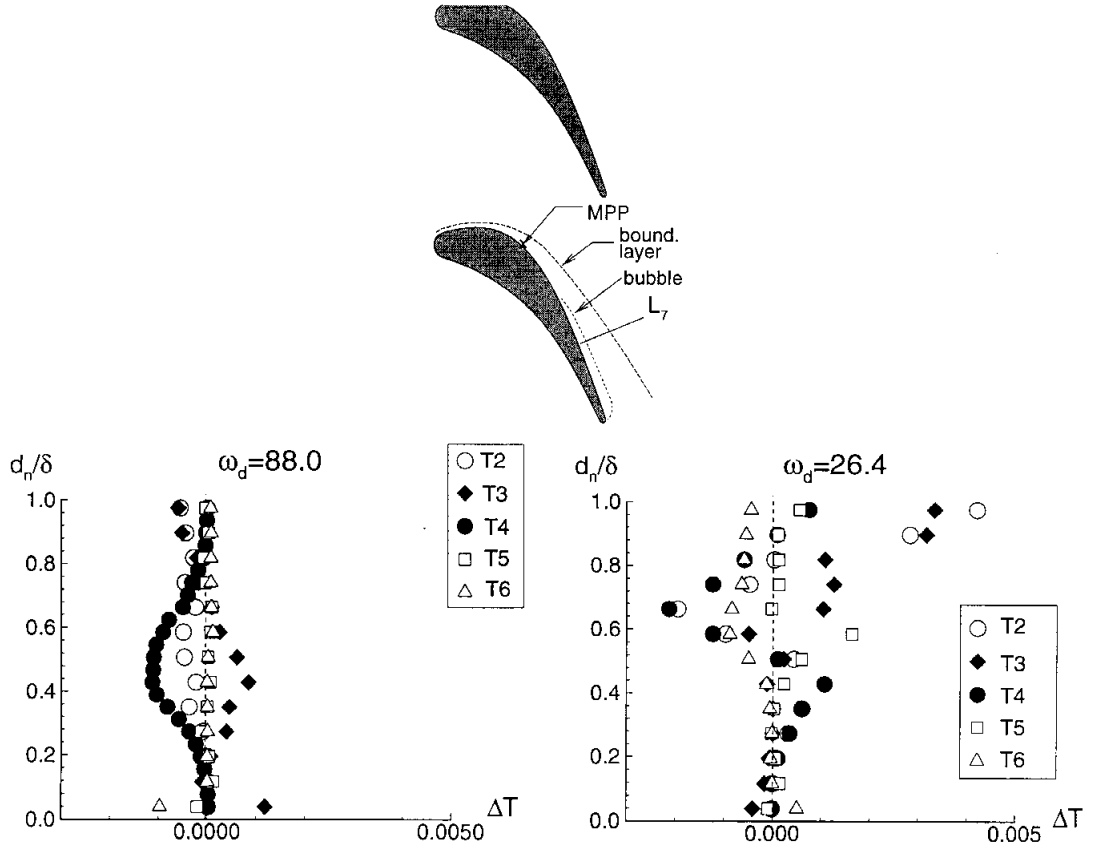

FIGURE 29d. Changes in the FKE terms, measured across the boundary layer perpendicular station L7. Supercritical perturbed flow at Re=1000, ε=0.02, with ω_d=88.0 and ω_d=26.4.

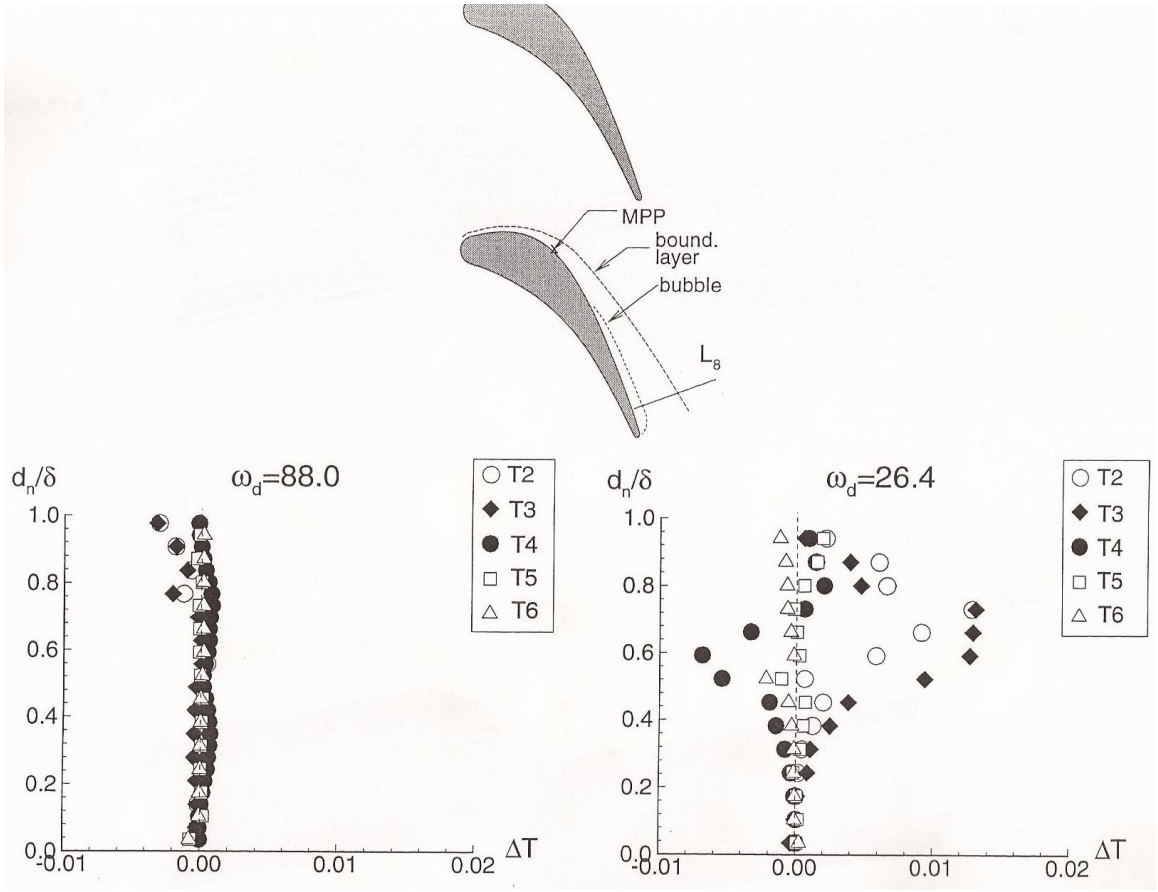

FIGURE 29e. Changes in the FKE terms, measured across the boundary layer perpendicular station L8. Supercritical perturbed flow at Re=1000, ε=0.02, with ω_d=88.0 and ω_d=26.4.

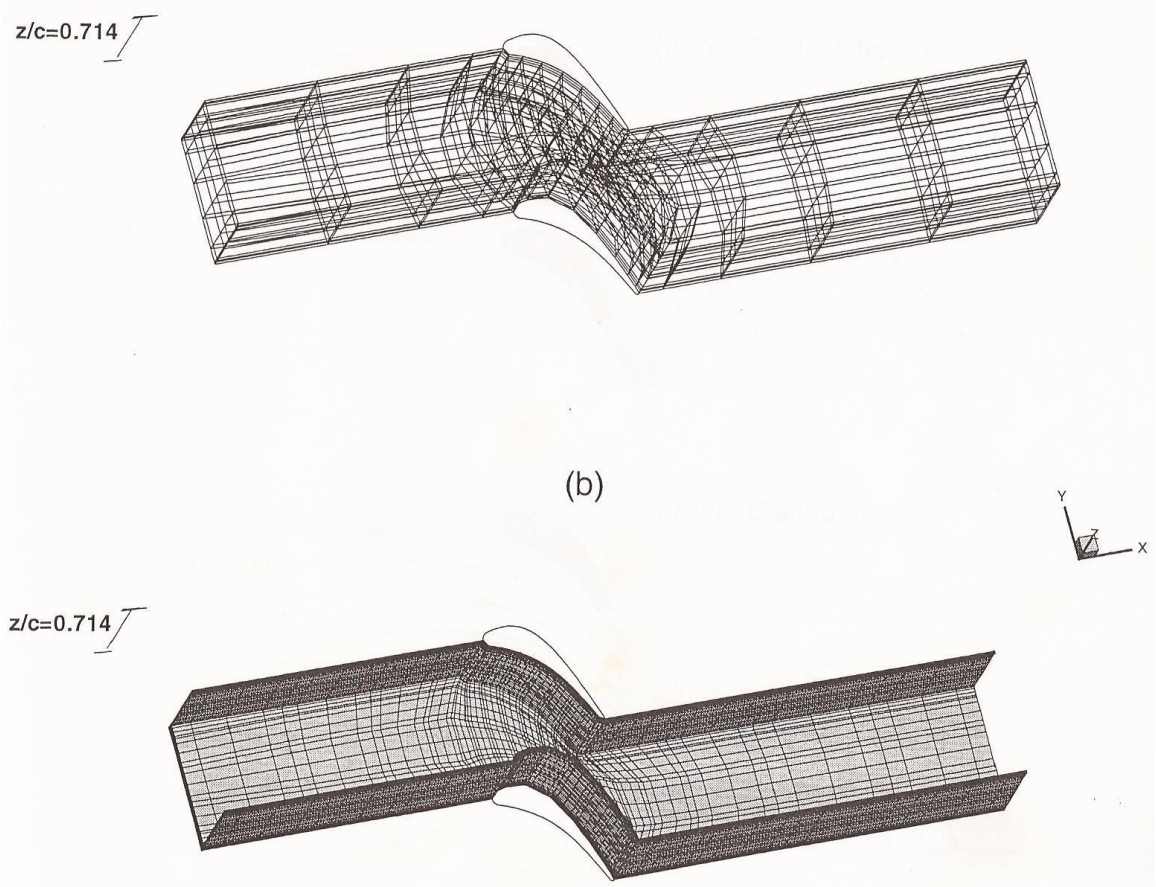

FIGURE 30. Three-dimensional computational domain. 630 macro-elements and 5x5x5 nodes per macro-element.

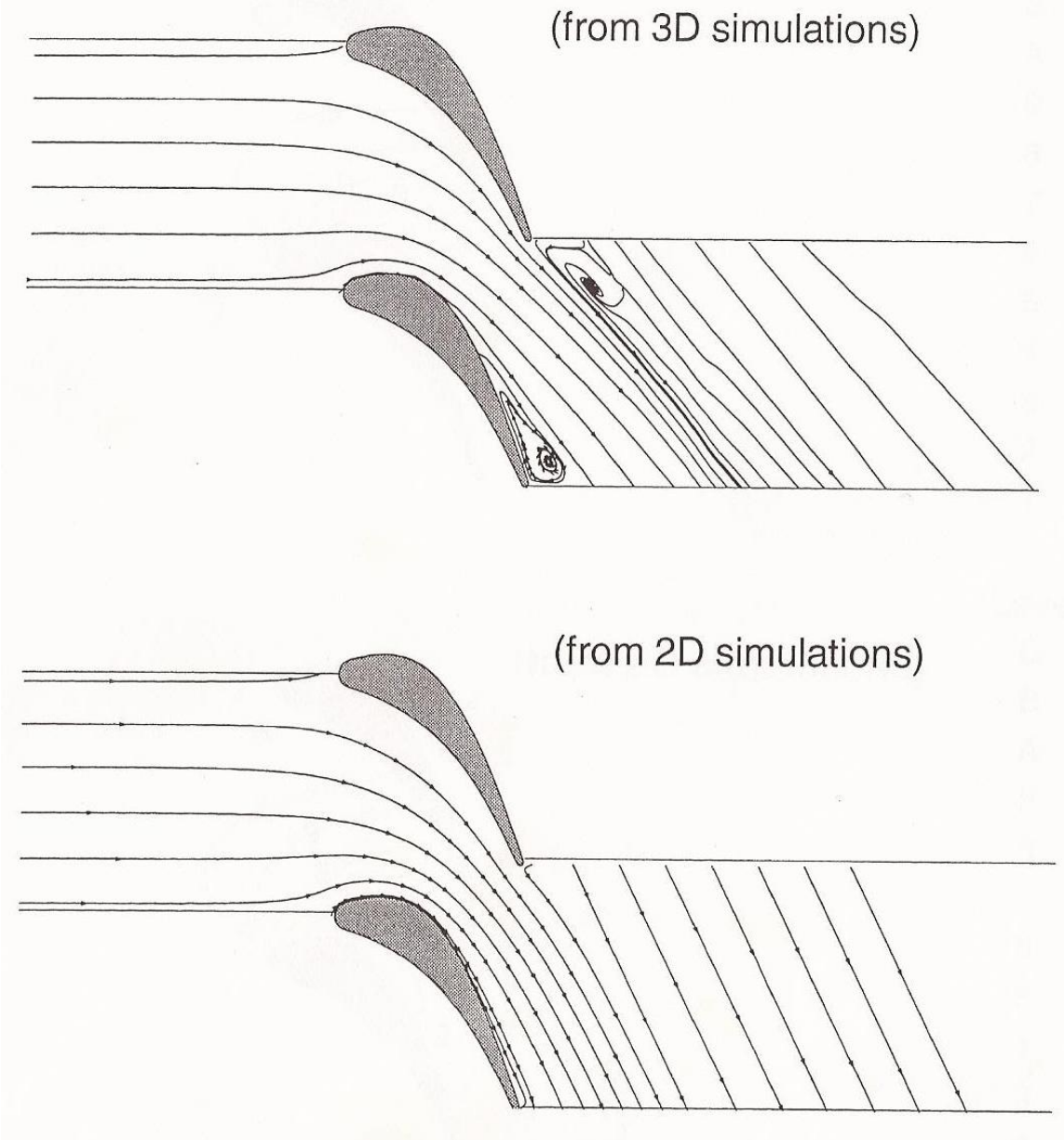

FIGURE 31a. Flow field at midspan section from three-dimensional simulations of the basic flow at Re=400. 630-element mesh with 5x5x5 nodes per element. Streamtraces based on x- and y-velocity components.

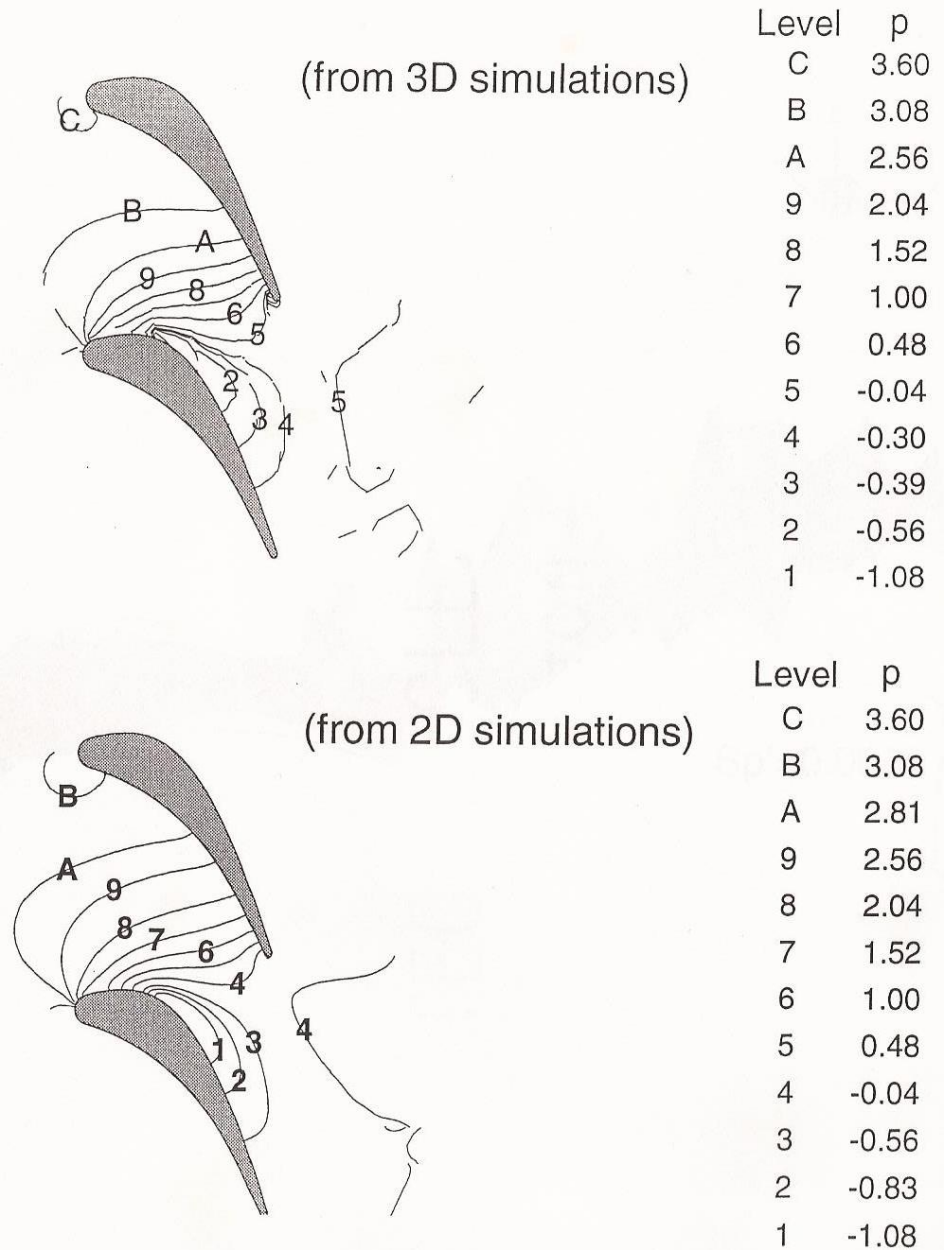

Level	p
C	3.60
B	3.08
A	2.56
9	2.04
8	1.52
7	1.00
6	0.48
5	-0.04
4	-0.30
3	-0.39
2	-0.56
1	-1.08

Level	p
C	3.60
B	3.08
A	2.81
9	2.56
8	2.04
7	1.52
6	1.00
5	0.48
4	-0.04
3	-0.56
2	-0.83
1	-1.08

FIGURE 31b. Flow field at midspan section from three-dimensional simulations of the basic flow at Re=400. 630-element mesh with 5x5x5 nodes per element. Mean pressure field.

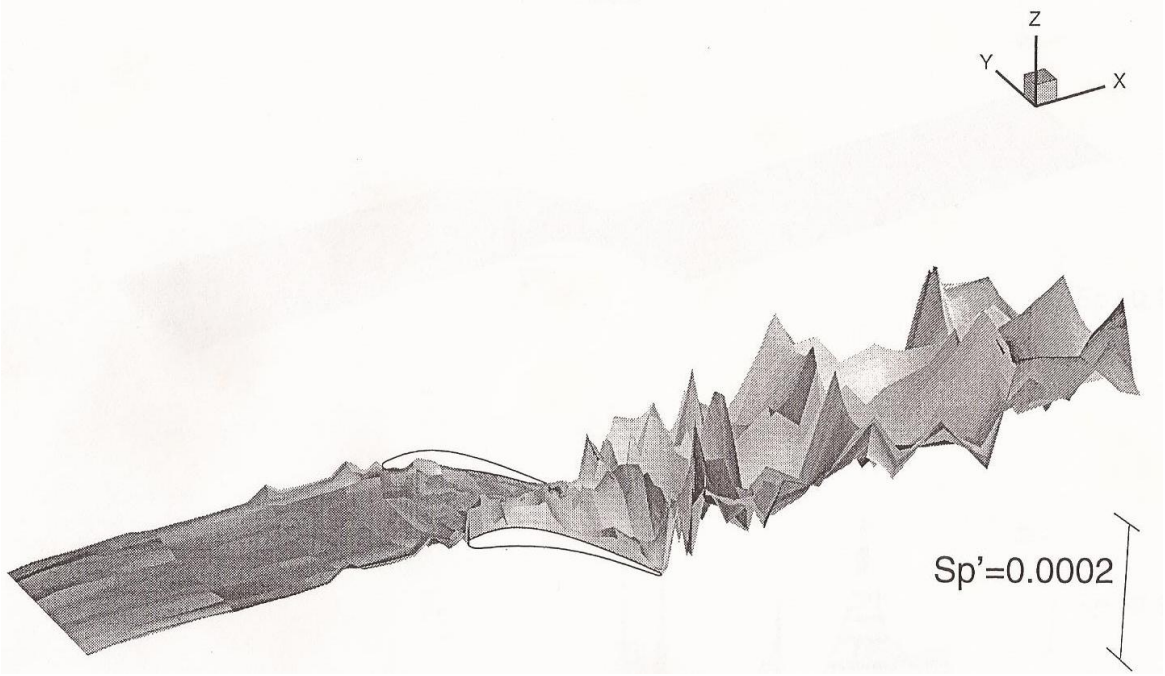

FIGURE 32. Carpet plot of Sp' at midspan section at characteristic time. Three-dimensional simulation of basic flow at Re=400.

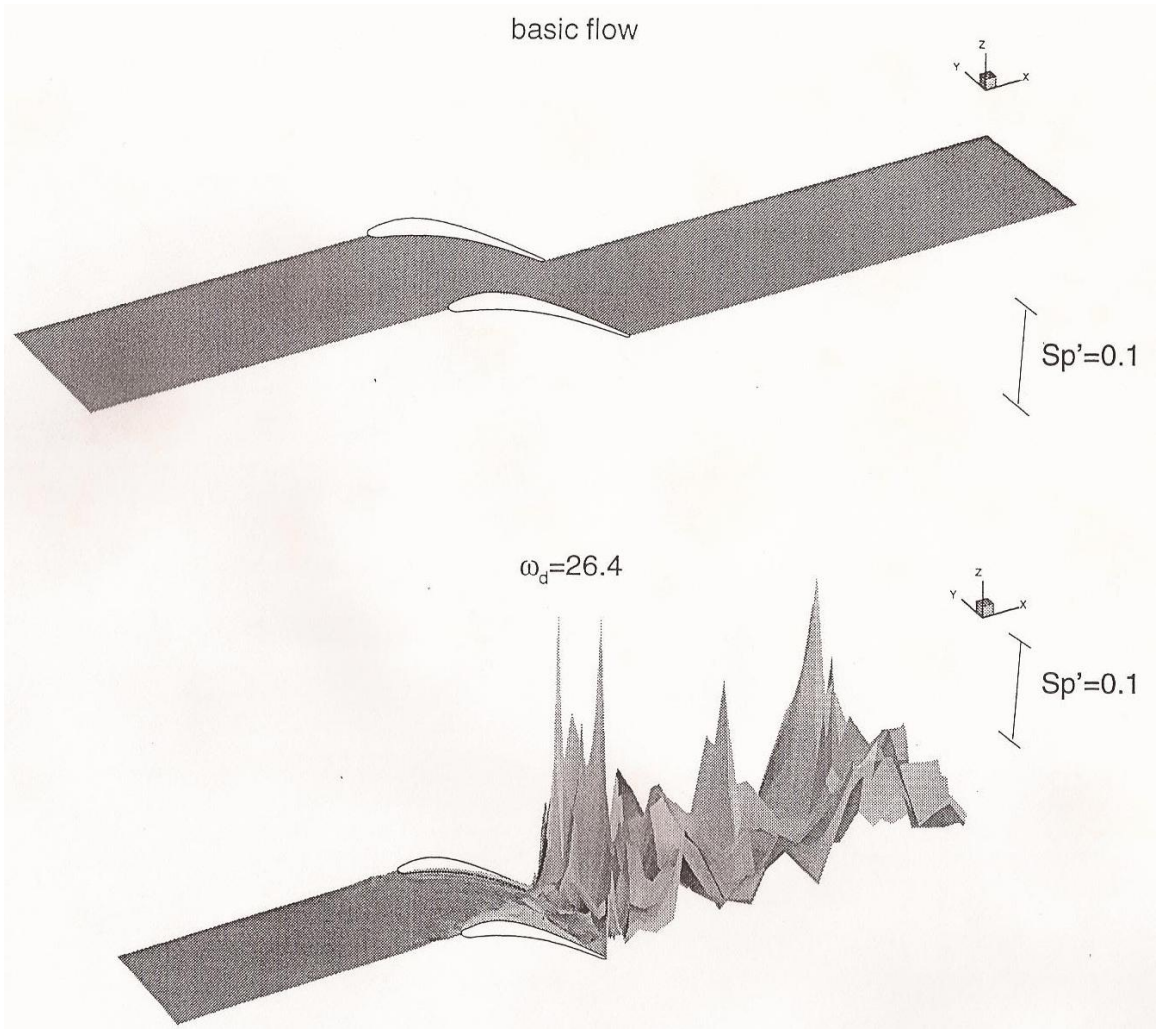

FIGURE 33. Carpet plots of Sp' at midspan section. Three-dimensional simulations at Re=400. Comparison between basic flow at characteristic time and perturbed flow with ε=0.02 and ω_d=26.4 when inlet perturbation vanishes.